The University Of Sheffield.

Nanostructured assemblies of light-harvesting molecules

By:

Charles H. Smith

A thesis submitted in partial fulfilment of the requirements for the degree of Master of Philosophy

The University of Sheffield
Faculty of Science
Department of Chemistry

February 2019

Declaration

This thesis, unless otherwise stated, is the work of the author and has not been submitted whole or in part for any other degree or qualification at this or any other institution.

Acknowledgements

Firstly, thanks must go to Professor Graham J. Leggett for giving me the opportunity to work in his lab and be part of an amazing research group. Over my time here I have had doors opened to opportunities and experiences I otherwise would not have had access to. Your constant support and guidance have proved priceless and enough thanks and appreciation can't be expressed here.

A special thanks to Rob Ducker, who started me off on this project, put his lunch down to talk to me and has been a constant help since. Thank you to other Leggett group members past and present who have provided all manner of assistance: Oscar Siles Brügge, Paul Chapman, Debbie Hammond, Brice Darroch, Max Chambers, Martin Munz, Mar Cardellach, Omed Al-Jaf and Ali Johnson.

Extra thanks must be given to my friends who have made my time in Sheffield so enjoyable, particularly Matt, Jenna and Nick who have put up with living with me, my top YAG pal Catey and all the people I have played sport with and against, particularly Lukey and all the members of SULRFC that is has been my absolute pleasure to coach.

Most importantly, I must acknowledge the support and love given to me by my mum, sister and brother, you've all been a constant presence, the impact of which can't be overstated. I hope I've done you all and the old man proud.

Finally, Rheanna, you poor, poor angel, having to put up with me in these last few months. You deserve some form of medal. You've been my rock and I couldn't have finished this without you.

Table of contents

List of figures

1. Abstract

Our current reliance on fossil fuels is not sustainable in the long term and the need for renewable energy grows ever larger. It is with this in mind that we look towards harnessing the power of sunlight. Whilst devices currently exist that work by capturing solar energy, polymer based photovoltaics have limited efficiency and stability whereas by studying the light-harvesting mechanisms of plants and bacteria, we may be able to design better performing solar cells which have the additional benefit of being made from renewable materials. The photosynthetic apparatus of plants, bacteria and algae is an abundant source of inspiration; a full understanding of these mechanisms may enable the design of more efficient photovoltaic devices. These species have evolved their own specialized methods of harvesting light and rapid energy transfer and these mechanisms and their potential to be exploited and adapted in solar energy capture for human purposes are the focus of this project.

In order to fully explore the photosynthetic process, synthetic systems will need to be designed in order to replicate the light-harvesting environment. Photosynthesis in plants and bacteria utilises light harvesting antenna complexes, whose structure are difficult to manipulate. The goal of this project is to build synthetic structures that incorporate elements of these antenna complexes, e.g. pigment complexes, so that the relationship between structure and function can be explored directly. In the first instance our focus is on membrane components but not on the reconstruction of the membrane. Lithographic techniques will be employed to pattern surfaces incorporating light-harvesting molecules in order to test hypotheses about energy transport within two dimensions. Of particular interest is the relationship between bacterial light harvesting and the spatial organisation of components in antenna complexes.

2. Introduction

2.1. Photosynthesis

The process of photosynthesis begins with the absorption of light energy and its transformation into an electronic excited state followed by a charge separated state and subsequent conversion to a proton gradient across a membrane.[1] Plants and bacteria have evolved in different mechanisms to best maximise their light-harvesting efficiency, yet have retained the same basic components: a reaction centre (*RC*) which is situated at the centre of the unit and antenna complexes which surround it and feed energy into the reaction centre and there will be many of these within each cell. The light harvesting unit of the purple bacteria is simpler compared to its evolutionary competitors in cyanobacteria, algae and plants. Whilst plants and bacteria both use redox process, plants have evolved more complex methods to feed photoexcited electrons directly into cellular processes via splitting water and synthesising sugar.[1] The antenna within bacteria tend to be structurally simpler than plants[2] and therefore provide an easier route to replication and by studying one of the least complex light harvesting units known in nature, that of purple bacteria *Rhodobacter* (*Rba.*) *Sphaeroides*, we give ourselves the best chance of being able to identify the role the quantum coherence plays within light-harvesting and how, if at all, it should be utilised in the manufacture of solar cells.

2.1.1. The photosynthetic unit of purple bacteria

2.1.1.1. The reaction centre

The overall structure of the RC of *Rba. Sphaeroides* consists of a scaffold of three polypeptide chains and ten cofactors.[3] The three polypeptides are labelled as the H-, L- and M- chains and they act to hold the cofactors in the required positions for efficient light-harvesting. The L- and M-polypeptide consist of five alpha helices each that span the

membrane and have particular importance in holding the cofactors in the correct position, whilst the H-polypeptide has a single membrane spanning alpha helix and a domain that caps the cytoplasmic side of the L- and M-polypeptides.[3]

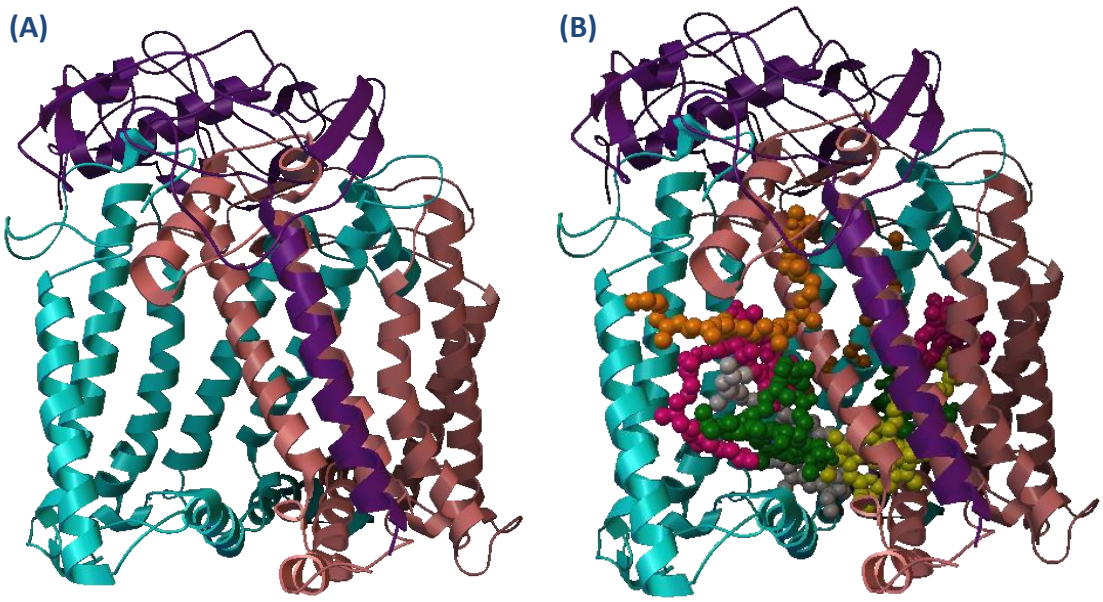

Figure 1. (A) Representation of the three polypeptides that make up the scaffold of the reaction centre of *Rba. Sphaeroides*; H-polypeptide (purple), L-polypeptide (teal) and M-polypeptide (light pink). **(B)** Representation of the ten cofactors held within the three polypeptides. This figure was constructed using PDB file 1PCR[4] and Python Molecule Viewer.[5]

The cofactors consist of four bacteriochlorophyll (*BChl*), two bacteriopheophytin (*BPhe*) which is similar to BChl, but with the magnesium ion removed and replaced with two hydrogen atoms, two ubiquinone-10 molecules, a ferrous non-haem iron atom and a carotenoid. Two of the BChl cofactors form a dimer which is often referred to as the special

pair (*P*) and on either side of these are the remaining two BChl, the two BPhe and the two quinones further out still, as shown in figure 2. One of the ubiquinones is not fixed in place within the core of the reaction centre as its movement is necessary in the facilitation of charge transfer through the membrane. The remaining nine cofactors are held in location by the proteins, with the iron atom also appearing to provide structural support.[3]

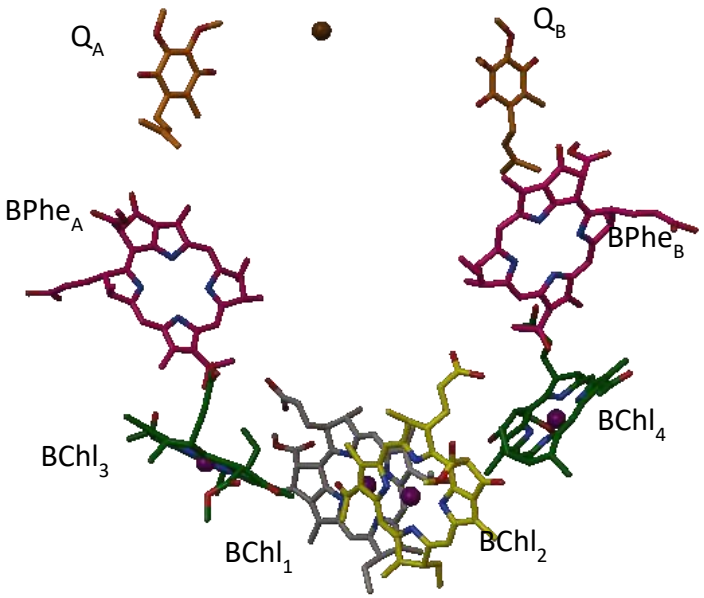

Figure 2. Representation of nine cofactors that make up the photosynthetic unit of *Rba. Sphaeroides*; two BChl which form the special pair dimer (yellow and grey), two accessory BChl (green), two BPhe (bright pink), two ubiquinone-10 (orange) and an iron atom (brown). Hydrocarbon tails have been removed for clarity. This figure was constructed using PDB file 1PCR[4] and Python Molecule Viewer.[5]

Within the RC, light energy is absorbed by the six BChl and BPhe and is funnelled to the two BChl which form a dimer, where the process of charge separation begins in earnest. This then leads to the formation of the first singlet excited state of the BChl special pair which is able to donate an electron to one of the BChls, forming a negatively charged dimer and positively charged BChl state. The electron is subsequently transferred from the BChl to the nearest BPhe followed by transfer to the stationary quinone and this process occurs on the picosecond timescale. On the microsecond timescale the electron is transferred from the stationary quinone to the mobile quinone. Following the reduction of the special pair this process can occur again coupled with proton uptake by the negatively charged quinone so that a quinol molecule is formed which can be transported across the membrane, to a transmembrane protein pump known as cytochrome bc_1 which removes the protons and electrons, thus creating a proton gradient which drives ATP synthase. The cycle is completed by binding of a new quinone and the utilisation of other cytochromes, including cytochrome c_2 which is responsible for the transfer of electrons across the membrane back to the special pair to reduce it from P^+ to P.[6]

2.1.1.2. The antenna complexes

The process that occurs in the reaction centre requires two electronic excitations of the special pair in order to produce the quinol and it is therefore of great importance that the reaction centre is able to operate at a high photoexcitation rate in order to prevent charge recombination and the loss of stored energy.[7] Whilst the four BChl and two BPhe within the reaction centre can absorb light directly and create the first excited state of the special pair, bacteria have developed a series of additional antenna complexes in order to capture light and transfer the energy to the reaction centre. This is necessary as bacteria often dwell in places with very low solar irradiance and so increasing the light-harvesting cross section is vital for photosynthesis to occur; for example a medium sized leaf on a windowsill is hit by 10^{16}

photons per second compared to a single green bacterium found at a depth of eighty metres under water which receives only 300 photons per second, but has developed an incredibly efficient light-harvesting system in order to thrive in these conditions.[7]

Rba. Sphaeroides utilises a light-harvesting structure called light-harvesting complex one (*LH1*) which consists of a ring of thirty two BChls (often noted as B875 because of its main absorption peak at 875 nm and similar notation is used for other bacteriochlorophyll throughout) and sixteen carotenoid molecules, spheroidene, arranged as close as possible around the RC.[8] These molecules are held in a circular structure by thirty two membrane spanning α-helical scaffold proteins of which sixteen are located between the RC and the ring (α- peptides) and the other sixteen are located outside the ring (β- peptides) with the ultimate effect being that a pair of α- and β- peptides hold two BChls and one carotenoid in place.[8] Such is the synergy and close proximity of the reaction centre and the light-harvesting complex one that they are often described as one term RC-LH1.

In order to provide the perfect balance where each reaction centre receives the same amount of light energy as it turns over, *Rba. Sphaeroides* employs further antenna complexes in close proximity which feed energy into LH1 called light-harvesting complex two (*LH2*).[a] Each LH2 consists of a tight ring of eighteen B850 bacteriochlorophyll molecules and nine carotenoids sandwiched between nine α- peptides and nine β- peptides.[1] In addition LH2 also contains another ring of nine BChls, with a major absorption at 800 nm, positioned slightly above and perpendicular to the B850 ring and are more loosely packed.[1] When fully

[a] Throughout, light-harvesting complex two shall be abbreviated to LH2, which should not be confused with the light-harvesting complex two which is found within plants and certain green algae which is abbreviated to LHCII within the literature.

assembled, each chromatophore vesicle contains ten to twenty RC-LH1 complexes and a further fifty to one hundred LH2 units as shown in figure 3.[1]

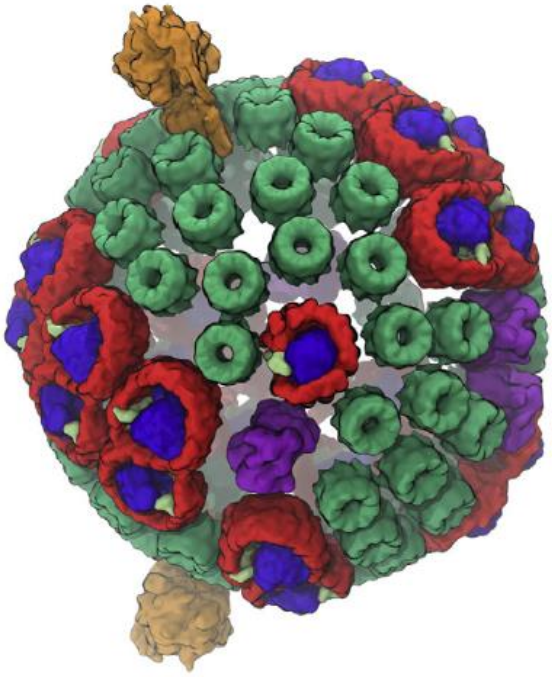

Figure 3. A model of the chromatophore unit of *Rba. Sphaeroides*; RC-LH1 units (blue and red), LH2 units (green), cytochrome bc_1 (purple) and adenosine triphosphate (*ATP*) synthase (orange). Figure adapted from Cartron et al.[9]

2.1.2. The energy transfer process

Fluorescence resonance energy transfer (*RET or FRET*), also known as Förster energy transfer after Theodor Förster who published two papers describing the effect,[10, 11] is a key component in energy transfer between molecules within antennae complexes and also from antennae complexes to the RC.[12] It is this theory which explains the transfer of energy to the B850 ring from the B800 ring within the LH2 complex. Mutants of the LH2 motif which have absorption bands at different wavelengths but no noticeable changes to the arrangement

of the complexes have been used as a means of proving that this energy transfer behaves in the way that Förster theory would predict.[13] The changes in the absorption band result in increased spectral overlap of the two rings within LH2 which in turn leads to an increase in the energy transfer rate and this behaviour is fully expected according to Förster theory.[13] Förster theory predicts that when a light-harvesting molecule is irradiated with light of the correct wavelength an electron is excited from the ground state to the excited state, at which point an exciton is formed and this excited state is transferred between molecules via a hopping mechanism.

Early in the study of light-harvesting antennae complexes it was noted that Förster theory alone can not fully explain how light energy is transferred between molecules.[14, 15] For example it was found that the transfer of energy from the B800 ring to the B850 is faster than that predicted by Förster theory.[14, 15] The hopping mechanism, as described in Förster RET, only holds true when there is weak interpigment coupling and the dominant coupling is between the chromophores and their environment.[2] In systems such as LH2, we know there to be strong interpigment coupling and therefore Förster theory becomes a poor description of energy transfer as it does not take into account the delocalization of excitons across the BChls.[12, 16] This delocalization of the excitonic state is referred to as electronic coherence. Förster theory predicts a temperature dependence of energy transfer from the B800 ring to the B850 ring via vibronic states only, yet experimental evidence suggests that at room temperature the speed of transfer is in fact much faster than predicted. This led to the belief that the electronic coherence within the B850 ring plays a role in providing an alternative pathway.[15]

It has been found that within the reaction centre that the BPhes and the BChls share energy, but with longer than expected lifetimes for the excited states and it is suggested that quantum coherence plays a role.[17, 18] The excited state lifetime predicted using Förster theory

is eclipsed by measurements taken using a two-colour electronic coherence photon echo experiment. The experiment uses a laser pulse at 750 nm to specifically excite the BPhes followed by a second pulse at 800 nm to excite the BChls and finally a third pulse is fired which only generates a photon echo signal if the excited states of both the BChls and BPhes are mixed. The results are shown in figure 4.

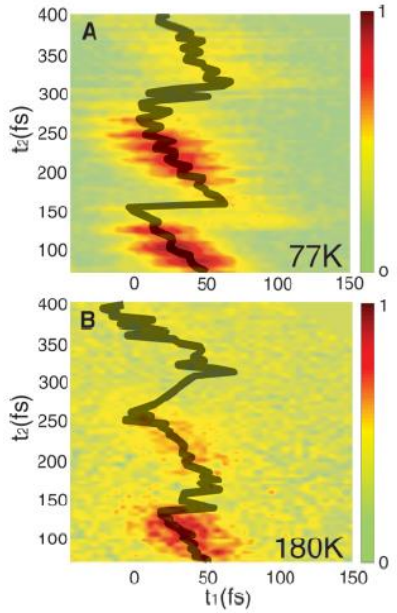

Figure 4. Integrated echo signals from a two-colour electronic coherence photon echo experiment with a *Rba. Sphaeroides* sample, as a function of time delays between laser pulses at **(A)** 77 K and **(B)** 180 K. The data shows that after 75 fs there are few strong signals for the excited state of the BPhe, across the *x*-axis, but that the excited state of the mixed BPhe/BChl system, the *y*-axis, exhibits signals showing a lifetime that gives out strong signals at 275 fs and weaker signals still for longer periods of time. Figure adapted from Lee et al.[17]

The oscillating nature of the coherent state is of interest because it was normally assumed that such coherent oscillations are destroyed very rapidly and that relaxation of the

excited state occurs via their destruction. With lifetimes extending well into the region of 660 fs, these oscillations are suggested to be the result of a quantum coherent superposition of excited states, referred to as quantum beats, a wavelike transfer of energy rather than the hopping mechanism as described by the classical Förster theory.[18]

As previously mentioned, there is a large discrepancy between the predicted timescale of energy transfer from the B800 ring to the B850 ring in LH2 between Förster theory and experimental results.[14, 19] This increase in transfer speed is largely believed to be due to the behaviour of the B850 ring as an acceptor for excitation.[20] The coupling between the B800 BChl pigments is weak, due to their relatively large separation distance, of approximately 22 Å,[21] and as a result they behave as normal donors in relation to Förster theory. On the other hand distance between BChls in the B850 ring is small, at approximately 9 Å,[21] which gives rise to interpigment coupling to a greater extent. This coupling changes the way they act as acceptors in the standard spectral overlap interpretation of energy transfer. If the B850 ring can share energy between BChls via electronic coupling to yield delocalised excitons we should consider that state as intrinsically multichromophoric, meaning that the spectral overlap is an average of the ensemble with a density of states based on electronic coupling factors.[20] The role that disorder within the B850 ring, which can be considered as the interaction with its environment, plays is of importance because it broadens the density of states within the ring and thus increase the spectral overlap and reduce the energy transfer time, yet vibrational motions also cause dephasing of neighbouring pigments.[20]

There is still no clear answer to the question, “what is the role of coherence within light harvesting?” Whilst it is has been known for a long time that electronic coherence exists within certain antennae complexes[22, 23] and is almost certainly involved in the process of light-harvesting and energy transfer, the role of quantum coherence has only recently been investigated thoroughly. This is due to the relatively modern development of two-

dimensional electronic spectroscopy (*2DES*) as a method of preserving and probing coherences.[24–26] It is also known that the environment plays a role in the longevity of excited states but a key question that it is hoped will be addressed is how fundamental this role is, as well as the spatial and distance dependence of the arrangement of the pigments within the light harvesting antennae. The replication of light-harvesting environments on a two-dimensional surface is one of the ways in which these questions can be investigated. Synthetic biomimetic assemblies of components from antenna complexes may enable us to examine phenomenon systematically, e.g. as a function of separation, in a way that is not possible in the naturally occurring proteins.

2.2. Surface Plasmon Resonance

When a material has free surface electrons, those electrons will oscillate. When the frequency of incident electromagnetic radiation matches that of the plasma frequency of the electrons in the material, resonance occurs.[27] Upon changing the angle of the incident beam, keeping the wavelength fixed, or vice versa, a minimum transmission, or reflection if the material is not transparent to the wavelength being used, will be found, at which point the incident will be in resonance with the oscillating electrons.[28] Oscillating electrons will propagate across the surface of the material, most commonly gold, and are known as surface plasmons (*SP*). When they are resonating with an electromagnetic wave, it is known as surface plasmon resonance (*SPR*).[27, 28]

This phenomenon is acutely related the texture and dielectric constant of the material, but also the dielectric properties of the medium surrounding it.[27] Changes to the latter will change the wavelength of the SPR peak, which is the basis of many applications. For example, if a protein binds to the surface, the SPR peak will change. Should the protein subsequently interact with another molecule, an additional change to the SPR peak will occur. This is the premise upon which SPR sensing is based.[29–31] SPR can also be coupled with FRET in order to carry out distance dependence studies of biological molecules. However, the interaction between FRET acceptors and donors is only useable up to 10 nm, but a layer of metal can be placed in contact with the donor and acceptor and couple with both such that when light it absorbed by the donor, the energy is transferred to the acceptor over a distance of up to 120 nm via surface plasmons with high efficiency.[32, 33]

For nanostructures, i.e. smaller than the wavelength of the incident light, localised surface plasmon resonance (*LSPR*) may occur. In this case, the electric field of the electromagnetic wave can be considered constant, leading to electrodynamics governing the

interaction rather than electrostatics.[34] In this situation the plasmons are not said to propagate and are instead limited, or localised, to the nanostructures. The number, intensity and location of these LSPR bands are not only linked to the dielectric properties of the medium[34, 35], but also to the shape and size of the nanostructures.[35–37] To this extent, if the spacing between nanostructures is too small, then the spectra will appear no different to a continuous film.[38] As with propagating resonance, this localised plasmonic behaviour is also subject to changes in the local media and can be used in sensing applications.[28, 31, 39–41] Nanoparticles can be used as so called plasmon rulers, whereby two nanoparticles can undergo plasmon coupling with each other and the resulting plasmon wavelength is known to red-shift as the interparticle distance decreases.[42] This phenomenon can be used such that particles can have biological molecules bound to their surface and the distance dependence of any interactions can be monitored by the shift in the coupled plasmon wavelength or alternatively, an interaction that will lead to a distance change can be monitored against time by measuring the change in peak position.[43]

In addition, it has been discovered that when certain light harvesting particles are attached to gold nanoparticles which exhibit a LSPR, an unusual change occurs. Rather than the plasmon peak shifting slightly as a result of a difference in the local refractive index, the shape of the absorption curve changes entirely. This suggests that a different phenomenon is occurring regarding the transfer of energy between the light harvesting molecules and the nanostructure, and the link between size of the nanoparticle and the density of the light harvesting structures can be investigated. In order to investigate this fully, systems in which full control of the surface and its chemistry need to be employed and methods of creating such systems are explored below.

2.3. Self-assembled monolayers

In the early 20th Century, some of the first highly reproducible monolayers were produced using what are today known as Langmuir-Blodgett techniques,[44, 45] which involve the formation of thin films at an air-water interface and their transfer onto a solid surface through the use of 'troughs.' This technique is arduous, however, and limiting in terms of the types of molecules that can be adsorbed to a surface. Further experimentation was carried out into alternative methods for the adsorption of molecules and subsequently the properties of monolayers adsorbed onto metal were first published during the 1940s.[46] The films produced in this manner were hydrophobic and oleophobic in nature i.e. water and oils would not wet the surface, which initially led to a relatively limited scope of study for their use, to applications such as friction reduction.

Over the subsequent thirty or so years of continued experimentation and exploration, these monolayers systems attracted growing interest for modelling and studying surfaces and surface processes. They were used in areas such as replicating biological membranes,[47, 48] photochemical reactions,[49] catalytic behaviour,[50, 51] electrochemistry[52] and electrical conduction.[53] On the back of this work much effort was put into characterising monolayer assemblies, and even more so when there was evidence to suggest that the monolayers could form spontaneously with a high degree of control.[54, 55]

Momentum was gained in the field in the 1980s and continues to this day since work by Allara[56] and Sagiv[57] documented the adsorption of sulfides onto gold and trichlorosilanes onto silicon, both with a varying range of functional groups on the resulting surface allowing a wide range of applications to be explored. It was at this time that the term self-assembled monolayer was coined and become commonplace for describing such systems.

Self-assembly is a technique that has gained popularity due to its use in the fabrication of surfaces with multiple functionalities onto a multitude of substrates. Films formed have recently been shown to be susceptible to micro- and nanopatterning through various lithographic processes and can be subsequently reacted to, to create further stepwise modifications to the surface, examples of which will be detailed further in this chapter. With these features in mind, there is a great scope to create, replicate and study biological interfaces and well as design and fabricate features that can be used in electronics and devices.

2.3.1. Formation of self-assembled monolayers

The basic components of self-assembling molecules are the head, chain and tail of each moiety; each contributing in a different way to the properties of the monolayer. The head group is part of the molecule that reacts with the substrate to create a chemical bond, i.e. chemisorption, the strength of which correlates to the stability of the monolayer. The tail of the molecule is most frequently on the surface of the monolayer and controls the functionality of the layer depending on the nature of its functional group. The tail therefore determines the chemical routes of reaction available as well as physical properties such as hydrophobicity/hydrophilicity. The chain is merely a linker between the head and tail groups, and though the least important part of the molecule it can influence monolayer formation. For example in a solution of competing molecules which have differing chain lengths but otherwise identical head and tail groups, it is the chain length which is shown to determine which molecule dominates the resulting monolayer.[58] The chain can also contribute to steric effects that dictate tilt angle of the monolayer and that prevent the most efficient and compact packing of the molecules on the surface. When an imperfect or ‘patchy’ monolayer is formed, the tail group is liable to collapse and may become buried in the monolayer and thus remove

the desired functionality. The ability to produce and control highly ordered monolayers is therefore highly desirable.

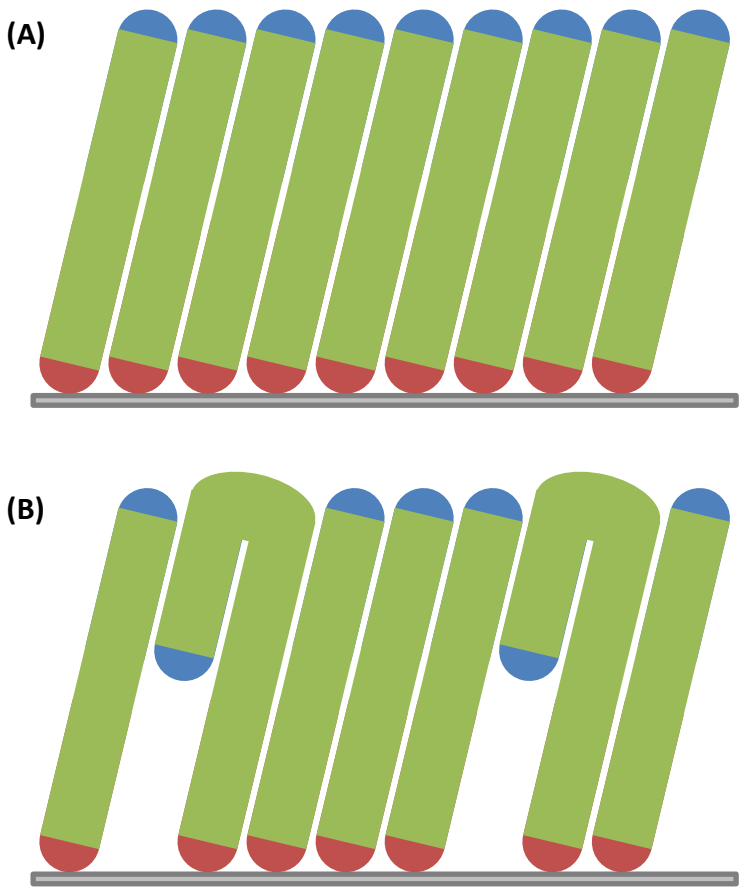

Figure 5. (A) A diagram showing how individual molecules can arrange to form a monolayer. The head group is shown in red, the chain is shown in green, the tail is shown in blue and the substrate is shown in grey. **(B)** An example of an imperfect monolayer, for example caused when a combination of short and long chains are present during adsorption and the tail groups of the longer chains can become buried in the monolayer.

2.3.1.1. Thiolate systems

In contrast to Langmuir-Blodgett films, which are formed by the compression of a molecular film at the air-water interface to drive a liquid-solid transition in two-dimensions, self-assembled monolayers (*SAMs*) form spontaneously following immersion of a surface in a solution and provide greater versatility in terms of the type of monolayer that can be created. One system in particular that received focus was that of disulfides (*RSSR*) and sulfides (*RSR*) adsorbed onto gold films. These were of particular interest because of the previously held belief that gold was inert to chemisorption and that only weak physisorption occurred at its surface; this enables SAMs to be formed on gold surfaces in ambient conditions as any contaminants on the surface are only weakly held there. Sulfides and disulfides are also compatible with many functional groups as they will nearly always bind preferentially to the gold via the sulfur atom over bonding via the functional group.[59] Some of the first work that identified this behaviour and exposed the potential of the system[56] led to further study[58–63] and subsequently the routine use of thiol (*RSH*) monolayer formation on gold as a way of making cheap and easily reproducible functionalised surfaces. The mechanisms behind the chemisorption of disulfide, sulfide and thiol moieties and the subsequent spontaneous arrangement into ordered monolayers are still not known with full certainty, however, the most documented and widely believed are mentioned below.

It has been shown that it is a gold thiolate, an Au-S bond, that links the monolayer to the surface, which has been shown using x-ray photoemission spectroscopy (*XPS*) studies.[64] There is a strong preference for the chemisorption of thiols over disulfides from mixed solution even though the end monolayer is almost chemically identical,[43, 46] yet disulfides will readily adsorb when carried out in ultrahigh vacuum (*UHV*) conditions when thiols will not.[65] Thiols that are chemisorbed from solution proceed to thiolates via the scission of the S-H

bond and early infrared[66] and Raman spectroscopy[67] studies proved that no S-H bonds were present on the surface of the substrate.

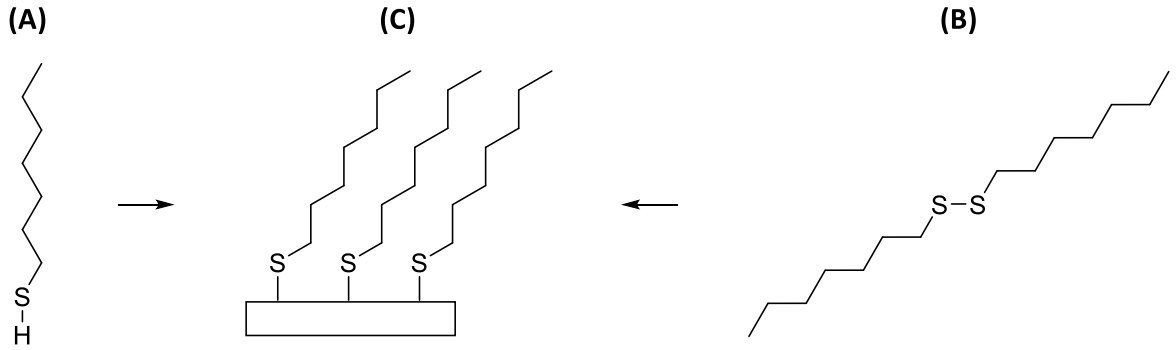

Figure 6. A diagram showing how two precursor molecules, an alkanethiol **(A)** and a disulfide **(B)** when adsorbed from separate solutions will result in the same thiolate type self-assembled monolayer **(C)**.

Whether the scission proceeds after adsorption of the thiol molecule via transfer to the gold surface and subsequent release as H_2 or otherwise is harder to determine. Hydrogen released from thiols has been shown to reduce nitro groups in the monolayer, a situation not observed when the equivalent disulfides are adsorbed, due to their lack of S-H bonds required to produce hyrdogen.[68] On the other hand, for alkanethiols deposited in UHV conditions, only physisorption takes place, which is supported by evidence of an S-H bond remaining for a much greater period of time than if the monolayer was deposited in atmospheric conditions, caused by the absence of an oxidant and a different kinetic regime existing in UHV.[64]

The adsorption of disulfides proceeds via an oxidative addition to the surface, the dissociation of the S-S bond, in both ultrahigh vacuum conditions[65] and from solution.[60] XPS

studies of the sulfur region have shown there to be no S-S peak which proves that intact disulfide molecule are not bound to the surface.[60, 64, 65] The preference for thiol adsorption over disulfides when present in a mixed solution could arise from steric hindrance of the bulkier disulfide and the fact that two adjacent coordination sites must be available.[64, 65]

Though adsorption onto gold is the most widely studied, adsorption onto a variety of metal films can be achieved using a range of disulfide, sulfide and thiol solutions, with concentrations as low as 0.01 to 0.001 molar. Monolayers will spontaneously form from a range of adsorbates with varying alkyl chain lengths and terminal functional groups as well as from a variety of solvents and the differing kinetics and stability of these films are well understood.[59] Monolayer adsorption itself takes only a few minutes to achieve approximately 90% surface coverage[60] and a few hours for full coverage with the resultant chains bound to the surface being close packed, stable and oriented,[59, 69] though the extent of which varies and the surface of the monolayer may exhibit different lattice properties compared to that of the base where the sulfur atoms bind to the gold,[70, 71] which can go some way to explaining the differing structural properties depending on chain length and head group.

Multicomponent monolayers can also be produced by placing the adsorbent in a solution of competing adsorbates.[58, 63] Through changing the length of the chain and the functionality of the terminal end of the thiol, a large range of potential applications are available, for example, the incorporation of a molecule into the monolayer that allows it to function as a sensor.[72–76] Other applications include catalysis[77–79], fabrication of electronic systems[80, 81] and as etch resists.[82]

As touched upon, other metals can be used as the foundation of a thiolate monolayer, though thiols on gold remain the standard for reasons summarised in a review piece from the Whitesides group.[69] The review states five main reasons for gold's continued use which are

summarised as follows. Firstly, gold is easy to obtain as a thin film and a colloid. It can easily be prepared as thin films by physical vapor deposition, sputtering, or electrodeposition. Secondly, gold can be patterned by a combination of lithographic tools and chemical etchants with ease. Thirdly, gold is a relatively inert metal that does not oxidize at temperatures below its melting point or react with atmospheric O_2. In fact, the almost exclusively high affinity for binding between thiols and gold is such that they can displace unwanted materials from the surface, not undergo any side reactions and can be handled in atmospheric conditions rather than under ultra-high vacuum. Fourth, thin films of gold are commonly used for several existing applications, including surface plasmon resonance spectroscopy, quartz crystal microbalances and ellipsometry. Fifth, the adherence and functionality of cells on gold surfaces are not compromised by toxicity of the substrate, a phenomenon that is witness when silver is used.[83] In addition, cell studies of SAMs formed from thiols on gold can be carried out over a period of days to weeks without a decline in performance.

2.3.1.2. Silane systems

At the start of the 1980s a different type of self-assembled monolayer was being explored. The system in question is that of highly ordered and well packed silane monolayers.[54, 57, 84] Figure 7 shows the form that silane monolayers take when chemisorbed to a surface. In contrast to SAMs of alkylthiolates on gold, which exhibit high degrees of order, films of silanes are more disordered and heterogeneous. The recorded O-Si-O distance is smaller than the van der Waal diameters of the adjacent tail group carbons, thus not leaving enough space for the alkyl chains to stand upright and form a well ordered monolayer.[85] It is believed that of the three bonds that silicon can make, the three X groups in figure 7A, only one or two are formed, either to another silane or to the surface and the remainder are left as –OHs which can hydrogen bond to the substrate or another silane resulting in a monolayer that is in a state

of equilibrium, such that O-Si bonds are constantly breaking and reforming in order to maintain the best coverage across the surface.[86]

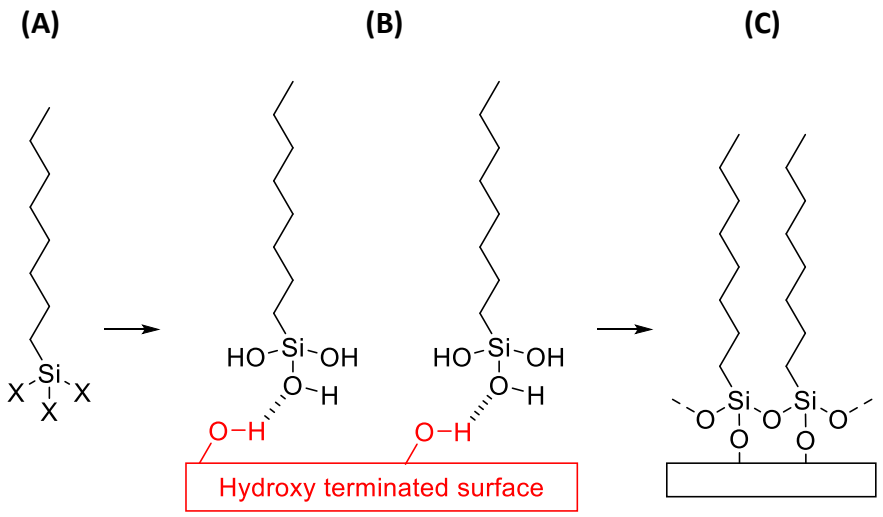

Figure 7. A diagram showing the process that occurs when a silane bonds to a surface and forms a monolayer. **(A)** Show the general formula of a silane, R-Si-$(X)_3$ where X is usually a chlorine, ethoxy or methoxy group and R can be one of many functional groups. A hydrolysis reaction will convert the silane into the form shown in **(B)** after which it will be able to hydrogen bond to a hydroxyl surface and intermolecularly. **(C)** shows the result of the condensation reaction that yields the final silane monolayer that has covalently bound to the surface and undergone planar polymerisation.

The concentration of water in solution has been shown to very important in the attachment of silanes to the surface. Figure 7 shows that water is required for the hydrolysis reaction in order to create the active species, yet if there is too much water present then there will be a greater number of silanes hydrolysed than there are hydroxyl sites on the surface

leading to potential polymerisation in solution and globular deposits on the surface that could lead to defects if they incorporated. If no water is present then the silanes may react with hydroxyl groups at the surface, but the remaining X groups can not be converted and so a patchy monolayer will be formed.[87] Whilst the two systems discussed here share these three key features notable difference is that where thiols are usually adsorbed onto a metal film, silane monolayers tend to be formed on silicon or its oxide.[88]

2.3.2. Characterisation of self-assembled monolayers

2.3.2.1. Contact angle analysis

Using a goniometer to measure a contact angle of a surface is a quick way of collecting a qualitative assessment of a monolayer almost immediately after it has been formed. The wettability of a surface is not overly affected by the type or roughness of the surface it is adsorbed onto, being nearly wholly dependent on the monolayer,[59] which makes the technique so useful for characterisation. Two liquids are commonly used in the production of contact angles, and provide different analysis; water provides information about the polarity of the surface and hexadecane provides information about the polarizability of the surface.[59]

For example, for methyl terminated alkanethiol monolayers with a carbon chain length of eight or greater, the contact angle of water remains relatively constant at 111-114°, but below these chain lengths the contact angle drops away rapidly.[59] For carboxylic acid terminated thiol monolayers though, no such chain length dependence is observed and the surface is wetted, with contact angles in the region below 10°.[59] It stands therefore, that contact angle study measurements can be used to prove the production of a patterned monolayer, for example the photooxidation of methyl tail groups to carboxylic acids. A study of contact angles against time of exposure for example would show the contact angle of the surface decreasing, towards only a few degrees, as the exposure time increases towards full

oxidation. Taking advancing and receding contact angles of multicomponent systems can also be used to determine whether separate domains have been formed.[63]

Many functional groups have had their contact angle documented, accounting for differing chain lengths, the solvent it was deposited from and the substrate it was adsorbed onto. The contact angle can vary based on the tilt of the monolayer from the surface, in order to achieve the densest packing, and this is partly based on the grain size the metal film, for example the tilt angle for gold is approximately 30°,[66] yet the smaller grain size of silver results in tilt angle of approximately 13°.[89] This change in tilt angle between different substrates means that identical monolayers on differing metals will have a different contact angle. Using these previously determined measurements, contact angle studies can be a very quick and useful way of establishing whether a desired monolayer or pattern has been formed.

2.3.2.2. X-ray photoelectron spectroscopy

XPS is a quantitative technique that is widely used in the abstraction of information regarding the chemical composition of a material. The sample is placed in a vacuum and is irradiated with photons of energies in the region corresponding to x-rays. This energy is transferred to core level electrons that, if they have enough energy, are emitted from the surface. These electrons are analysed as a function of their kinetic energies. These are related to the binding energies of the orbitals from which they are ejcted:[90]

$$KE = h\nu - E_B - \Phi$$

where KE is the kinetic energy of the emitted electron, hν is the energy of the exciting radiation, E_B is the binding energy and Φ is the work function of the surface. Because hν and Φ are dependent on the sampling machine and known, the equation can be simplified to a direct link between the kinetic energy of the emitted electron, which is measured, and the

chemical state of the electrons source, the quantitative information we are looking for. This relationship is dependent on the emission process being elastic.[91]

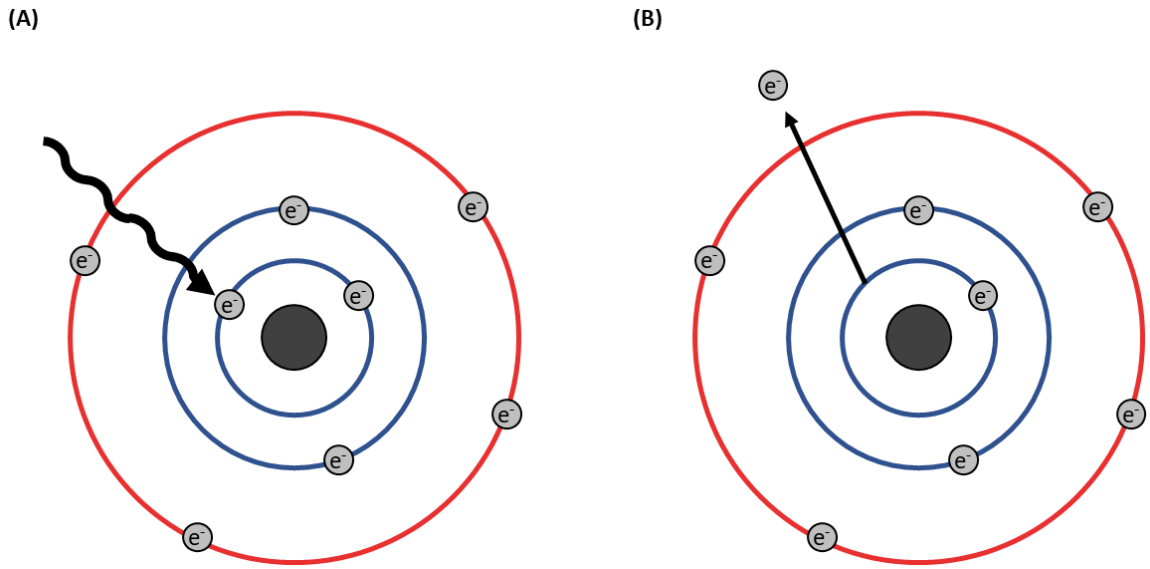

Figure 8. A schematic of the XPS emission process for an oxygen 1s electron. **(A)** An X-ray (black wavy line) irradiates an oxygen atom and the X-ray photon transfers energy to a core electron. **(B)** The electron has energy enough to be emitted into the vacuum chamber to be collected and analysed.

XPS is a powerful technique for analysing surfaces because only electrons from within the 2-3 nm of material can escape from the surface, due to the rate at which the electrons are lost through scattering. Electrons formed at greater depths than 10 nm are inelastically scattered before they can escape.[92] Therefore, despite the irradiated photons having enough energy to travel far through the material, it is exclusively the surface that is

characterised. This depth resolution is machine dependent and can be altered by changing the energy of the incoming photons and the take-off angle amongst other things.[93]

Regardless of the intensity of the illumination, no emission of electrons will take place unless the frequency of the X-ray is greater than or equal to the threshold level for each element. Once that threshold has been met, the number of photoelectrons emitted is proportional to the intensity of the illumination and any excess energy from using X-rays with a frequency higher than necessary, is emitted with the electron as extra kinetic energy.[90] The binding energy is, to a first approximation, the ionisation potential, however, its magnitude is influenced by the bonding environment of the element of interest. The electron's binding energy correlates to its distance from the nucleus and the charge of the nucleus itself. Each element specific peak in turn can be shifted a small amount by changes to the local chemical environment, for example, a difference in oxidation state, molecular environment or lattice site.[91] These shifts are usually only detected in high resolution scans.

XPS must be carried out in UHV conditions so that emitted electrons can be collected with minimal chance of having collided with gas molecules, which would reduce the signal, and so that the surface can remain free from contamination during the experiment. The X-ray source is often magnesium or aluminium and is made to emit fluorescent X-rays after a high energy electron beam has impacted upon it, and it is these X-rays that are directed towards the sample, though often indirectly through a thin piece of foil and a monochromator in order to prevent weaker X-rays from hitting the surface creating satellite peaks and to block high energy electrons and heat from hitting and altering the surface.[90] XPS systems also need to contain an analyser and detector, the job of which is to measure the energy distribution of the electrons emitted.[94] Also required is a collection lens which brings the kinetic energy of the photoelectron down to a constant in line with the range of the energy analyser, the pass

energy, which allows the resolution of the spectra to be controlled. High resolution spectra are usually collected at pass energies of 5-25 eV and wider survey scans at 100-200 eV.[90]

2.3.2.3. Secondary ion mass spectrometry

Secondary ion mass spectrometry (*SIMS*) is a technique used to acquire the mass spectra of surfaces. The process involves the sample, usually a solid surface, being bombarded with primary particles which cause the emission of secondary particles. These particles are then detected and analysed to yield a mass spectrum. In imaging mode, mass spectral data are mapped across the sample surface.

SIMS is different to conventional mass spectrometry as the ionisation source doesn't ionise the sample directly, but rather a primary particle which in turn ionises molecules at the surface of the sample. The technique can be generalised into two categories; 'static' SIMS and 'dynamic' SIMS. Static SIMS is so named due the low flux density of the primary beam resulting in only 1% of the surface being bombarded by a primary ion, making a second impact in the same place statistically highly unlikely.[95] Early primary sources used for static SIMS used an electron bombardment source. The brightness of such sources are only moderate and as such can produce spot diameters of <5 μm.[96]

This has since been largely replaced by using field ionisation sources due to their greater brightness; the brightness of a liquid metal ion gun (*LMIG*) can be up to nine orders of magnitudes greater than those generated by an electron ionisation source.[97] An LMIG source consists of a tip (<10 μm), often tungsten, covered in a film of liquid metal, often gallium, indium or bismuth, which is placed in the region of a high extraction field and primary ions are then stripped from the resulting Taylor cone, either in the liquid or vapour phase, and accelerated towards the surface of the sample.[96] The brightness of such sources has routinely led to spatial resolutions (see later) of 150 nm and as low as 20 nm.[98]

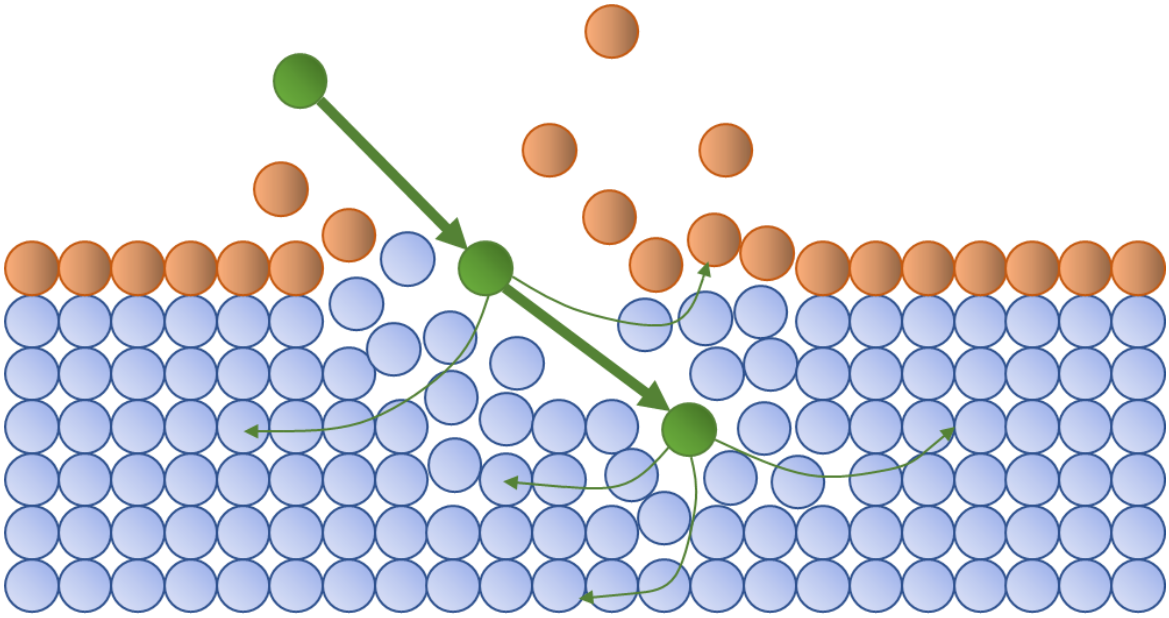

Figure 9. A diagram showing the collision cascade that occurs when a primary ion (dark green) is fired at the surface of a material (orange). The primary ion can travel further into the bulk of the material (light blue) up to a depth of about 10 nm (shown by the dark green arrows). As the primary ion collides with atoms of the target material, energy is transferred (light green arrows) and some of these collisions make their way back to the surface of the material where can be emitted as secondary ions to be collected and analysed.

Should the flux density be high, areas of the surface may be hit by a primary particle more than once and if so, the fragment generated by the second particle will be from below the original surface and therefore not provide true characterisation of the surface. The result is a mass spectrum of a changing surface and hence the term used to describe this phenomenon as 'dynamic' SIMS. This was the first type of SIMS analysis to be carried out and it was not until almost two decades later that Benninghoven's group developed the

technique of static SIMS by reducing the primary ion flux density.[99] Since its discovery in the 1950's this approach has been honed for use in depth profiling and surface ionisation sources are used.

As the high energy primary particle hits the surface it deposits its kinetic energy deep in the sample, causing a cascade of collisions. As the collision cascade spreads out through the sample, the energy density is reduced. Eventually some of the energy returns to the surface where it causes atoms and molecules to be ejected. A small fraction of the sputtered particles are ionised. Emission occurs when the particle's kinetic energy is greater than the binding energy to the substrate. This emission is up to a maximum depth of approximately 30 atomic layers; 95% of all secondary particles originate from the topmost two layers of the sample.[98] SIMS has a significant advantage over electron impact mass spectrometry in that negative ion fragments can be detected using SIMS. The negative spectra do not contain hydrocarbon ions and thus can provide a different kind of information.[98]

The majority of secondary particles are neutral but it is the ionised secondary particles which go on to form the mass spectrum; however, the fraction of desorbed ions is only 10^{-1} to 10^{-6}.[100] A key process in the optimisation of SIMS as a technique comes from improving the number of secondary ions that are both emitted and detected. Traditionally only one m/z channel could be detected at a time, meaning all ions not of that channel are not detected. One solution to this is to use a time of flight SIMS (*ToF-SIMS*) setup, which can detect all ions that are generated within the detection range of the instrument

simultaneously. The formation of the secondary ion itself is still not a fully understood phenomenon and many different explanations were put forward in the early days of SIMS[101, 102] and even in recent years questions and uncertainty are still being raised against popular models of ionization.[103, 104]

Polyatomic primary ions such as Bi_3^+, Au_3^+ and C_{60}^+ produce increased yields of molecular fragments due to the fact they have a smaller sputtering depth and therefore more energy is present at the surface which leads to sputtering of larger fragments and more sputtering overall. When C_{60}^+ is used the yield of secondary ions was as close to 10% and favoured high mass ions. This high yield is a combination of the fact that there is more energy at the surface due to shallow depth penetration of the primary ion and that there is minimal cross sectional damage at the surface which means that higher doses than normal can be used and still maintain the static limit.[105]

In attempts to cause sputtering of larger still fragments, massive cluster primary ions were designed. Such a cluster which can produce ions with masses in excess of 80,000 Da is the Au_{400}^+ ion. When compared to monoatomic gold and small gold clusters ($Au_{3/5/9}^+$) the massive cluster caused greater secondary ion yield, enhanced signal-to-noise ratio, reduced fragmentation and less damage to the surface.[106]

SIMS can be used to form chemical images of materials. A spectrum is recorded at every pixel, allowing the retrospective analysis of the sample by mapping the distribution of specific ions.[100] This technique has been referred to as scanning SIMS and microprobe SIMS as well as SIMS imaging.

The key factor in the quality of the image is the lateral resolution or spatial resolution; the closest distance at which two objects may be distinguished as separate entities; this is commonly referred to as the size of the pixel. The pixel size is highly dependent on the spot size of the primary ionization beam, which in turn is dependent on the type of ion source and the focussing optics.[95] As mentioned above the brightness of LMIG sources is very high and so the resolution of these sources is routinely the smallest available, even more so when a polyatomic LMIG source is used. The limiting factor in most cases is not the size of the spot

but the intensity of the signal for each pixel. If the pixel becomes too small that very few ions are able to be generated within it then the intensity will be too low throughout the sample to derive any contrast within the image to tell one pixel from the next.[95] It is for this reason that attempts to increase the yield of secondary ions per primary ion impact are sought.

In the same way that dynamic conditions can allow for depth profiling, scanning SIMS can be utilised to provide a three-dimensional image of the solid being analysed. The surface is scanned and an image is acquired as described above, however unlike standard imaging, dynamic conditions are employed to erode away some of the solid after which another image is captured and the corrode-image cycle is repeated to a desired depth. The captured images are then arranged as slices on top of each other to provide a three-dimensional image of the solid. The technique does rely on the assumption that erosion is uniform across the sample otherwise distortion will appear in the final three-dimensional image.[107]

2.3.2.4. Atomic Force Microscopy

Atomic force microscopy (*AFM*) is technique that uses a force sensing tip to interact with a surface. A range of interaction forces, including electrostatic and magnetic, can be used to map of the surface in a variety of ways, including its topographical and frictional variances. AFM is a development of scanning tunnelling microscopy (*STM*), a technique in which electron density is mapped across the surface of a material. It was noticed that when the tunnelling current hit a certain threshold, physical interaction between tip and surface occurred. These physical interactions were studied and subsequently AFM was developed,[108] which has proven to be an extremely popular method of microscopy as it is capable of high resolution images and can be carried out on both insulating and conducting samples in both air and liquid.[109]

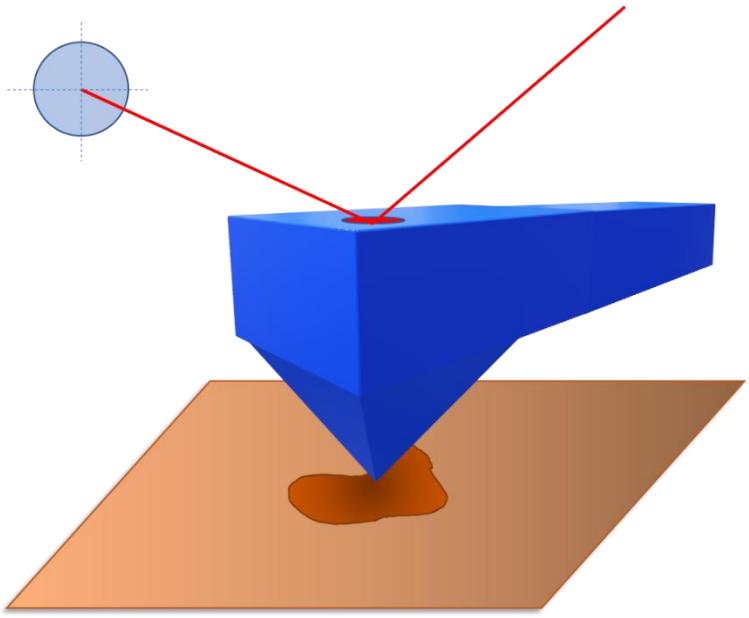

Figure 10. A diagram of the process in which a tip on the end of a cantilever is brought into contact with a surface. The cantilever's position is tracked relative to the interaction forces between the surface and tip and any deviation from normal is relayed through the AFM to produce an image of the surface. (Tip and probe not to scale)

The force acting on the tip can be measured in a variety of ways. Commonly, the tip is attached to a cantilever which acts as a Hookean spring:

$$F = -kx$$

where F is equal to the force, k is the spring constant and x is the deflection. The deflection of the cantilever is measured by observing a change in the deflection of a laser beam reflected off the back of the cantilever, a schematic of which is shown in figure 10.

The calibration process for this is a simple one in which the spring constant for the cantilever is such that any cantilever deflection can be assumed to move the piezo sensor the

same distance. The known distance can be related back to change in the photodetector's received signal to produce quantifiable date.[109]

The nature of AFM is force based and as such the natural first quantitative application is a force-distance measurement. In this process, the tip is positioned above the surface and then lowered towards the sample. Once in contact it is pressed further into the material and then retracted until the tip is no longer touching the surface. This allows the deflection of the cantilever perpendicular to the surface plane to be measured. This process illustrated in figure 11. The tip can be functionalised in a variety of ways, enabling the interaction forces between specific functional groups to be measured.[109]

The Lennard-Jones potential describes the interaction between atoms. At distances greater than their equilibrium separation, attractive forces dominate, while at distances less than the equilibrium separation, the dominant forces are repulsive in nature. The attractive energy varies with $1/r^6$ where r is the atomic separation. For a macroscopic object such as an AFM probe, the interation energy must be integrated across the tip surface, leading to an expression in which the interaction energy is proportional to $1/D$ where D is the separation. Two widely used contact mechanics models have been developed to describe tip-sample mechanical contacts. Short range, strong adhesive interactions and longer range, weak interaction are encompassed within the Johnson-Kendall-Roberts (*JKR*) model and the Deraguin-Muller-Toporov (*DMT*) model respectively.[109] The study and modelling of interactions between the tip and the surface are of vital importance and as such the field of contact mechanics exists to explore this area and further reading is abundant.[110–112]

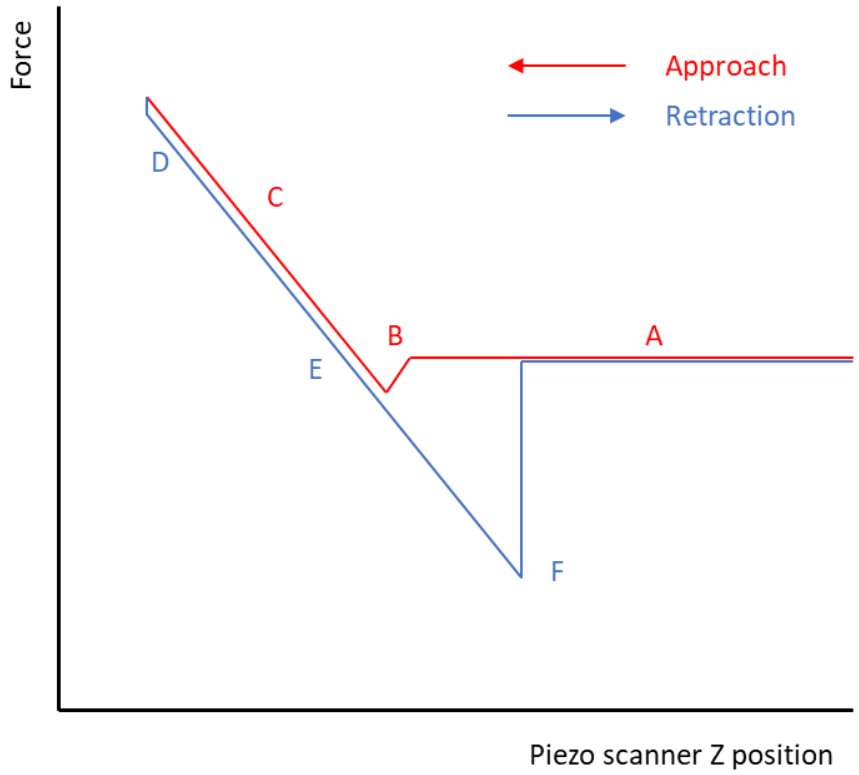

Figure 11. A schematic of a force curve. **(A)** The cantilever starts above and approaches the surface. **(B)** At a certain point an attractive force will cause the tip will 'snap' into contact and be touching the surface. **(C)** The piezo scanner will continue to push the tip into the sample generating repulsive forces. **(D)** The tip will start retracting. **(E)** If the tip adheres to the sample then the tip will not come out of contact at the same Z position as it did in the approach phase. As the tip is retracted further, but continues to adhere, it will cause the cantilever to bend and pull on the surface, producing an attractive force. **(F)** At a specific point a large enough force, called the pull-off force, is present to cause the tip to 'snap' out of contact. This difference between the out of contact force and the pull-off force is the force of adhesion, F_{adh}.

In addition to force-distance measurements, a variety of other modes exist which generate an image of the surface being investigated. In contact mode, the tip of the probe is brought into mechanical contact with the surface, and remains in contact in order to track the surface. The resolution is limited by the dimensions of the tip and the mechanical properties of the tip-sample contact. If a surface feature is smaller than the area of contact between the tip and the sample, it will not be resolved; therefore, in general, the sharper the tip the better. However, as the tip radius decreases, the contact area decreases and, for a fixed load, the pressure increases, causing an increased risk of damage to the surface and deformation of the tip.[109]

A feedback mechanism is required to control the motion of the tip relative to the surface. Precise control of the tip-sample distance is achieved using a piezoelectric crystal. Depending on the system being used that could be by moving either the stage the sample is mounted upon or the crystal itself. The z axis can be controlled in such a way that the cantilever can be held at a constant height, and any deflections caused by a rough surface are represented by a deflection of the cantilever. The cantilever can also be held at constant force, where the distance between the surface and the tip is maintained and adjustments to the cantilever's height are made in order to preserve the set force between the tip and sample.[109]

When the tip is in constant mechanical contact with the surface, it is liable to damage it. An alternative mode of operation was thus developed in which the tip oscillates at a high frequency close to the surface, striking it intermittently, up to once per oscillation cycle. This approach has become known as tapping mode and is useful for providing topographical information on the surface of softer materials such as polymers and cells. Tapping mode is not inherently a non-destructive technique, for if the amplitude of oscillation during tapping is significantly less than the amplitude of free oscillation then more energy will be dissipated

to the surface, potentially causing damage. However, the resolution is often increased for soft materials when compared to contact mode images.[109]

Tapping mode not only provides topographical images, but also phase images. When the tip is brought into contact with the sample, energy will be dissipated, but if the collision is near to elastic then the amount of energy dissipated will be small and there will be a small lag between the driving oscillation and the cantilever response. If the collision results in a large dissipation of energy, then there will be a large lag in the response of the cantilever to the driving oscillation. Thus by measuring changes in the phase lag it is possible to create an image of variations in the mechanical properties of the sample surface.[109]

A further mode of operation is frictional force microscopy (*FFM*), also known as lateral force microscopy (*LFM*). This is a type of measurement made in contact mode. The deflection of the cantilever is measured parallel to the plane of the surface, rather than perpendicular to it. Most modern instruments are capable of acquiring both components simultaneously. Topographical features may cause variations in the lateral deflection of the cantilever, in addition to those caused by variations in surface friction. However, in contrast to friction forces, which always act in opposition to the motion of the probe, these topographical contributions to the lateral deflections are independent of the direction of motion of the probe. To determine the true frictional component, the trace must be subtracted from the retrace and the resulting image will be free from topographical contributions to the lateral force, displaying only the surface friction.[113] Qualitative data can be obtained when a polar tip, for example a standard silicon nitride probe, is dragged across a sample which consists of both polar and non-polar regions, for example an alternating pattern of methyl- and carboxylic acid terminated regions. As the tip moves across the methyl terminated region there is limited attraction, so the frictional force is low. When the tip is moved across the highly polar carboxylic acid terminated region, there is are strong interactive forces resulting

in the tip dragging along the area in question resulting in a large dissipation of energy and a high frictional force.[109]

2.4. Patterning of self-assembled monolayers

There has been a great deal of interest in the use of patterned SAMs in a variety of applications. For example it has been found that long chain thiols, such as hexadecane thiol, act as suitable resists for some common gold etching solutions.[114] Alternatively, selective removal of thiols, e.g. by photo oxidation, allows for their replacement in a spatially selective fashion, allowing for modification of surface.[115] Similarly, spatially localised modification of silane films is also possible.

The techniques described below are a selection of ways in which monolayers can be produced such that selective etching or the formation of patterned multi-component thiol and/or silane monolayers can be manufactured.

2.4.1. Microcontact printing

Microcontact printing is procedurally very simple and utilises a stamp, usually made from polydimethylsiloxane (*PDMS*), that has been 'inked' in a layer of thiol,[116] silane[117] or protein[118] to transfer a molecular pattern to a surface. The stamp is brought into contact with the surface causing material transfer. PDMS is used because it is durable, so that multiple reuse is possible, and elastomeric, so that it easily conforms to the surface of the substrate it is being pressed against.[119] After pattern formation, the surface can then be exposed to an etching solution that will remove gold that is not protected by a thiol monolayer to create microstructures.[120] An alternative to etching is to instead deposit a material which selectively binds to the exposed metal, for example a protein resistant thiol,[121] or one which binds with the entire surface, but not strongly with the printed thiol and can thus be washed off, for example titanium oxide.[122]

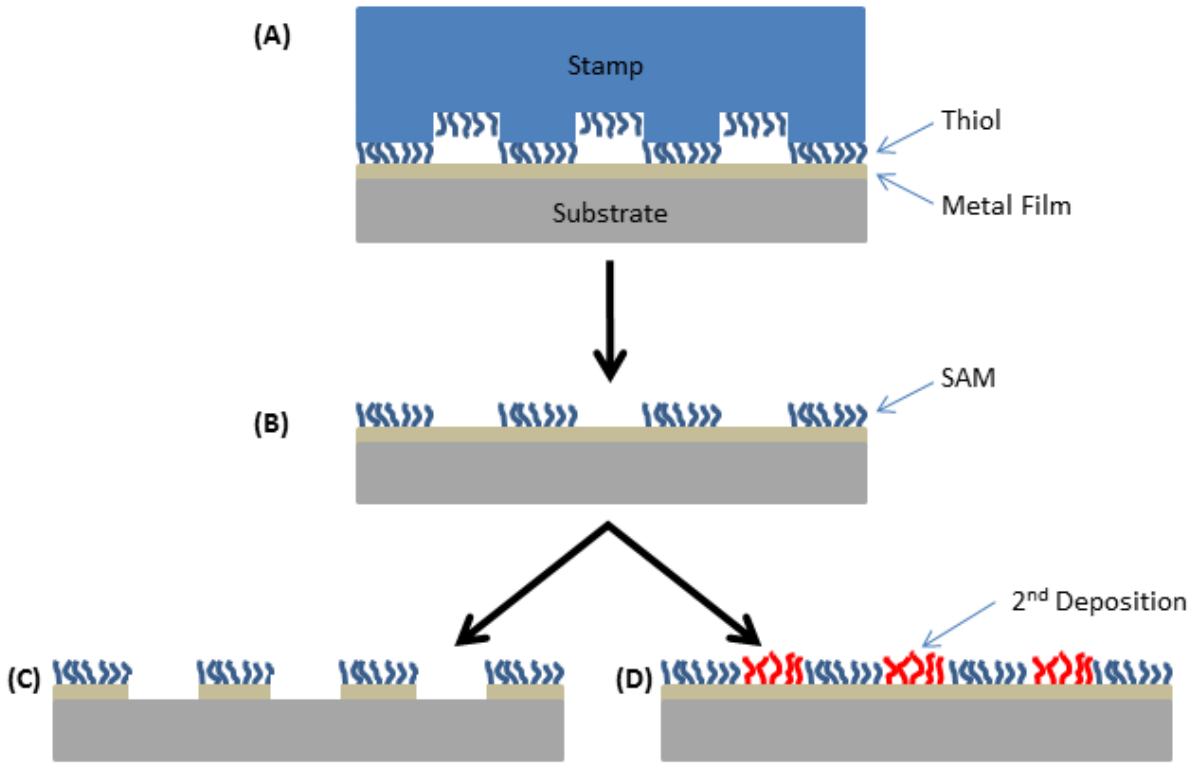

Figure 12. Diagram showing the stages of microcontact printing. **(A)** A stamp is "inked" with a thiol which is then placed against the metal film layer on the substrate. **(B)** The stamp is removed, and the "ink" is deposited on the metal to form areas of SAMs. The patterned surface can then be **(C)** etched with an appropriate etching solution to remove the exposed, unprotected metal surface or **(D)** a second material may be deposited in the gaps between the existing thiol regions.

Advantages of microcontact printing include: the mould can be cast from different master casts allowing for a number of complex patterns to be created, it is based on self-assembly which leads to fewer surface defects, it is relatively inexpensive and simple and can

be used by a range of scientists from different disciplines. Non-planar substrates can be patterned and there is no diffraction limit as experienced by light based techniques and resolutions of sub-micrometre can be routinely obtained.[119, 123] However, there are disadvantages associated with microcontact printing, for example deformation of the stamp will occur over time, defects are higher than in photolithography,[119] it has a limited range of reagents that can be applied to the substrate[124] and PDMS is a known surface contaminant.

2.4.2. Dip pen nanolithography

When an atomic force microscope tip is brought into contact with a surface, a capillary forms between the tip and the surface depending on relative humidity and surface wetting properties.[125] By coating the AFM tip with molecules that chemisorb to the surface and tuning the conditions so that capillary flow occurs from the tip to the surface, patterns of these molecules can be written in manner similar to the deposition of ink onto a paper from a dip pen nib, hence the name dip pen nanolithography (*DPN*).[126] The first molecules that were used as the ink were alkanethiols[126, 127] with line widths of 15 nm being achieved on atomically flat gold substrates. Since then, multiple different types of molecules have been used as the ink including; trichlorosilanes,[128] conducting polymers,[129] oligonucleotides[130] and metal ions.[131–134]

DPN has no need for resists or stamps and can therefore produce patterns in a user designed shape and unlike some other fabrication techniques that rely on the removal or changing of an existing monolayer, DPN directly attaches the desired feature to the surface. DPN can also deposit a series of compounds in sequence exactly where required,[127, 135] however successful DPN is dependent on an ultra flat surface.

2.4.3. Photolithography

Irradiation by light can lead to a chemical change in the monolayer, such as the breaking of a photocleavable bond[136] or the weakening of the bond between the monolayer and the substrate.[137] In this latter situation, the SAM is said to act as a positive-tone resist. This can enable the formation of a pattern, for example, in the case of monolayers of alkylthiolates adsorbed on gold, exposure to ultraviolet *(UV)* light causes photooxidation of the Au-S bond. The weakened bond can be displaced when the substrate is exposed to a solution of a contrasting thiol. This can be exploited by using a photomask to protect parts of the original thiol SAM, irradiating with light and then replacing the molecules in the photoexposed region.[138, 139]

Examples where bonds are cleaved upon irradiation with light are often based around the incorporation of a photolabile group to the surface of the monolayer bound directly to a functional group that can couple easily with other molecules, which could themselves incorporate a photolabile group and thus lead to multiple additions to the original monolayer[140] and an example of such a process is shown in figure 13.

The photolabile group can also be used to perform additional functions, such as act as a protein resist where upon exposure to light of the right wavelength, the photoexposed region is now no longer protein resistant and a pattern is created of protein adsorbed regions and the original monolayer.[141] Additionally arylthiolates can be used as the original SAM and act as a negative-tone resist, meaning that they become bound more strongly, because upon irradiation by light crosslinking between the aromatic groups occurs creating connections between molecules in the monolayer.[142]

Photolithography has many advantages including that the resolution is determined by the size of the beam and is not related to the molecules which make up the SAM or the ink in

the case of microcontact printing.[69] A feature of photolithography is that the dose can be easily controlled by the user by simply changing the time and intensity of exposure, which is not something that can be done as easily, if at all, in contact processes.[123] Disadvantages however include the fact that initial set up costs are high,[69] the technique is not one that is simple to use by all scientific disciplines[143] and that traditional techniques are restricted to a resolution which obeys the Rayleigh limit of $\lambda/2$, where λ is the wavelength of the incident light.[144]

New methods of using light to pattern surfaces have been developed that can achieve resolutions greater than that of the Rayleigh limit and examples include scanning near-field photolithography, interference lithography (*IL*) and extreme ultraviolet (*EUV*) photolithography. The need for such improvements is because the majority of components used in semi-conductor fabrication are produced using photolithography and, in accordance with Moore's law,[145] the demand is for these components to become smaller and smaller still.

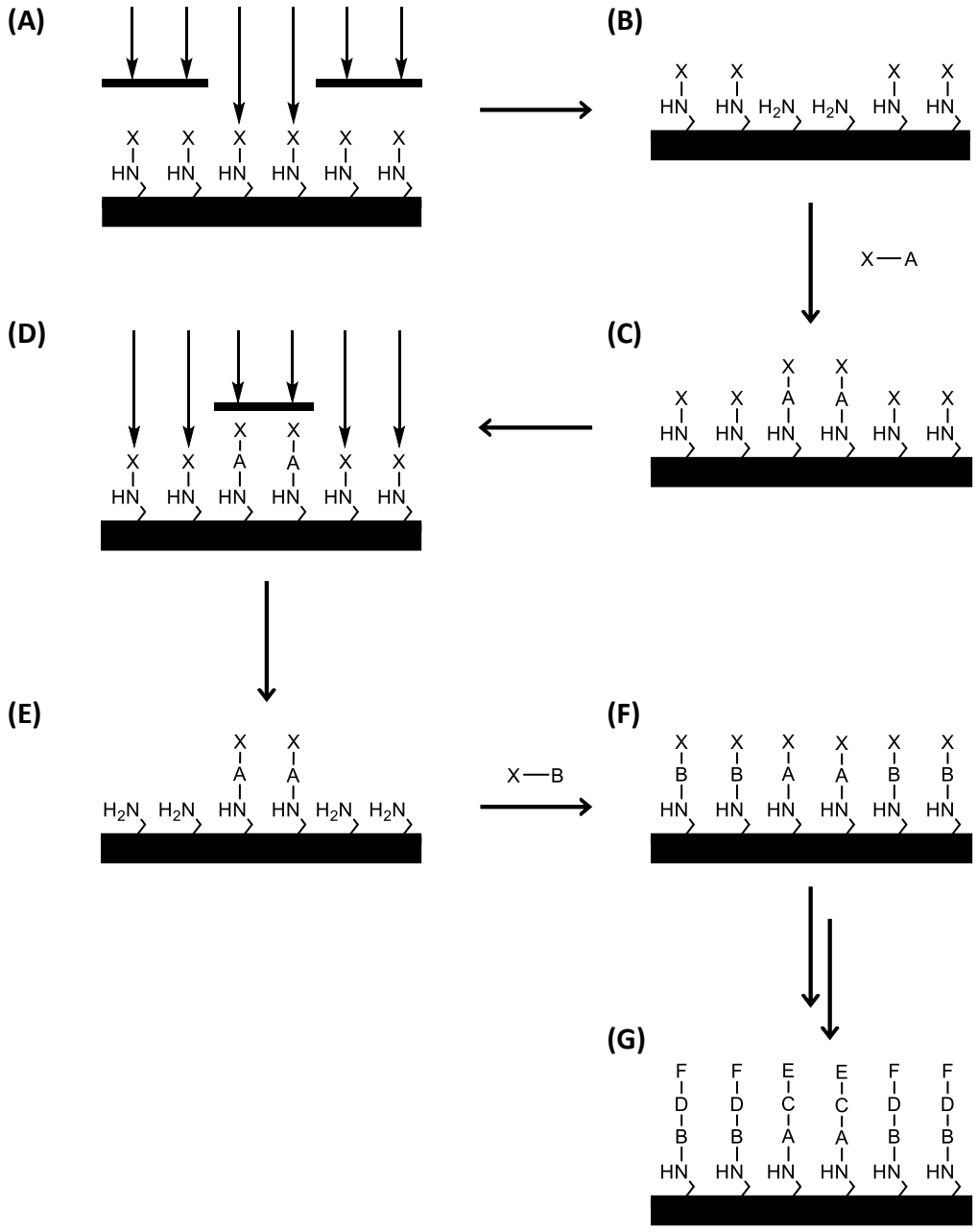

Figure 13. A diagram showing how a sequence of photo cleaving and binding can lead to a patterned monolayer. **(A)** Light, with the required energy, is shone at the surface, through a mask, facilitating the cleavage of the bond to the photolabile group, shown as X, in the photoexposed areas which results in **(B)**, the reactive functional group becoming part of the surface. A different molecule with a photocleavable group, shown as X-A, can be exposed to the surface, the product of which, **(C)**, is now a patterned monolayer. **(D)** In addition, the

original mask can be moved so that the previously unexposed areas will be exposed to the light, causing the removal of the photocleavable group. This resulting surface, **(E)**, can then be exposed to yet another molecule with a photolabile group, shown as X-B, producing a more complex patterned surface **(F)**. This process of removing the photolabile groups and extending the monolayer can be repeated many times resulting in the formation of thicker and potentially very intricate monolayers **(G)**.

2.4.3.1. Scanning near-field photolithography

Propagating electromagnetic radiation is subject to diffraction. When light passes through a subwavelength aperture, an Airy disc pattern is the result, imposing a limit on the resolution of:

$$\frac{0.61 \cdot \lambda}{NA}$$

where λ is the wavelength of the light and NA is the numerical aperture. However, in addition to the propagating wave, an evanescent, non-propagating field is formed, a near-field, which is not subject to diffraction, leading to technique with a theoretically unlimited resolution.[144] In a scanning near-field optical microscope (*SNOM*) the near-field is used to form an image of a sample.[146] In this setup an optical probe is attached to a tuning fork with and adjacent detector to collect light reflecting off the surface. The tuning fork is kept close to the surface using a piezoelectric, in order to ensure that light from the probe interacts with the surface in the near-field region.

This technique can be taken and directly applied to photolithography, though the first reports claimed resolutions of 60 nm, larger than that of the aperture in the optical fibre.[147]

Whilst near-field microscopy has problems associated with it that have deterred scientists from using it as a visualisation technique, such problems do not transfer to the technique when it is used for lithography and features of a size of 20 nm can be produced consistently[148] and at best 9 nm structures have been produced.[149] These feature sizes bring scanning near-field photolithography onto the same length scale as electron beam lithography. A disadvantage of scanning near-field photolithography is that it cannot produce features over larger areas in the way that microcontact printing can, as most setups allow only one feature to be produced at any one time, often at a slow speed.[144] However, it is possible to combine multiple probes to work in parallel in order to generate a larger scale pattern.[150]

2.4.3.2. Extreme ultraviolet photolithography

As has been previously mentioned the limit of resolution of a conventional optical technique can be approximated to $\lambda/2$; therefore in order to further decrease the possible feature size, it is necessary to reduce the wavelength of the incident light. Currently there is interest in the use of extreme UV lithography as a means to achieve better resolution than is feasible using current industry standard excimer lasers, $\lambda = 193$ nm.

Whereas conventional photolithography used light with wavelength in the visible region and then moved towards the deep ultraviolet region, $\lambda = 248 - 193$ nm, EUV photolithography uses light with a wavelength between 5 and 50 nm, most commonly 13.5 nm.[151] This can theoretically lead to production of features with a half-pitch of only 10 nm. However, the advent of immersion techniques when using 193 nm photolithography enabled conventional methods to achieve nodes of 45 nm in size. Initially this was a set back for work on EUV.[152] However, interest has renewed because of the importance of the 32 nm and smaller nodes.

Although theoretically EUV lithography can produce very small feature sizes, there are a number of major problems that have slowed its translation into manufacturing. In order to access these low nanometre wavelengths efficiently there is a challenge in developing a source with high conversion efficiency. Conversion efficiency is how efficiently the energy from a laser pulse, which is fired at a droplet, usually of tin, to generate plasmas that radiate EUV photons that are then directed onto the sample. This technique is known as laser produced plasma, though discharge produced plasma has also been considered as a possible source for the generation of EUV.[151] In addition to a high conversion efficiency, the source must also be high enough in power and yet not damage the collector optics, especially for high volume manufacturing.[151, 153] There is also work going into generating even lower wavelengths through generating plasmas from different elements such as terbium and gadolinium, though optimisation is not yet complete.[154]

Changes need also to be made to the type of resist used, because traditional resists are not practical for EUV photolithography. This is because as feature size decreases the resist layer is more prone to collapse as the ratio of width : height decreases for the individual areas of resist. This critical ratio can be predicted using knowledge of mechanical properties of the resist and the size of the feature.[155] There is also a sharp increase in the incident energy that must be absorbed by the resist as the move from 193 nm to 13.5 nm light is made, often resulting in incoming photons not being selectively absorbed by the appropriate part of the molecule, but by the entirety of the molecule, which is especially problematic when chemically amplified resists are used.[156] It has also been found that as feature size is reduced, the line edge roughness, the amount of deviation from a straight line along the edge of a feature, becomes proportionally larger than the line edge roughness of features created using 193 nm immersion lithography.[157] This is currently the largest problem in terms of obtaining the best possible resolution using EUV.

2.4.3.3. Interference lithography

Rather than using very expensive mask sets or EUV sources, sub-50 nm patterns can be created using interference patterns caused by coherent laser beams. The pitch of the pattern is based upon the wavelength of the light, the refractive index of the resist and the angle between the interfering beams, shown in figure 14B.[158] The substrates, resists and development processes used in traditional photolithography all are still usable in conjunction with interference lithography *(IL)*, except that there is no need for a photomask.[158]

Interference lithography is performed using an interferometer, which may utilise two or more beams, generated using multiple lasers or by using a beam splitter. An alternative approach is to use a Lloyd's mirror interferometer, shown in figure 14A, which generates the interference pattern by reflecting part of the original beam off a mirror onto the sample.

Multiple exposure schemes enable the fabrication of complex patterns. If the resist is exposed to one dose of the interfering laser beams, then a line structure will be produced.[159] The line width and period are determined by the angle as shown in figure 14B. However, a double exposure process can be conducted by rotating the sample between exposures to facilitate the fabrication of nanostructures of varying shapes and sizes.[38, 160]

An important advantage of IL is that it facilitates the fabrication of patterns on the square centimetre scale in a single exposure, which is particularly useful, for example, when producing arrays of biofunctional sensors.[161]

(A)

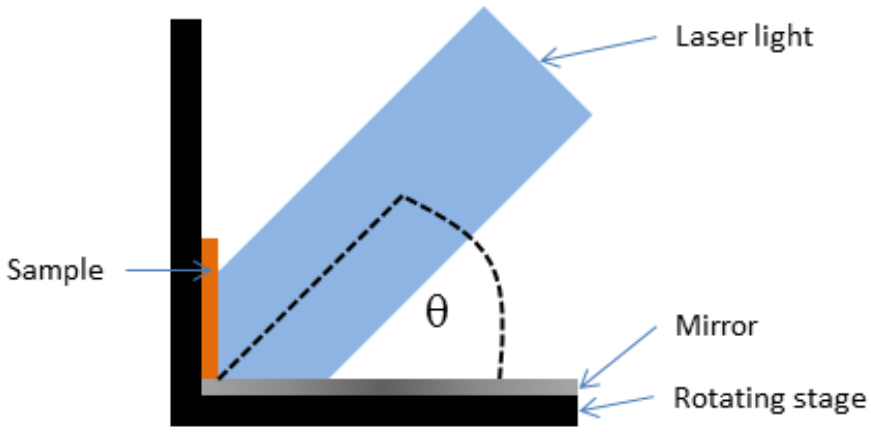

(B)

$$d = \frac{\lambda}{2n \times sin\theta}$$

Figure 14. (A) An illustration of a typical Lloyd's mirror set up, where a laser is shone at the sample and at the same time a mirror, which reflects onto the sample. Light reflected off the mirror interferes with light coming directly from the laser to create the interference pattern. The stage can rotate at the joint in order to change the angle at which the two beams come together. **(B)** The equation which determines the size of the period of the pattern, *d*, based upon the wavelength of the incoming light, λ, the refractive index of the resist material, *n*, and the angle at which the two coherent laser beams interfere, θ.

2.4.4. Electron beam lithography

Development of electron beam lithography (*EBL*) began in the late 1960s[162] and became more widespread once poly-(methylmethacrylate) had been discovered as an electron resist

that showed a large number of traits desired in a photoresist to be used for high resolution patterning.[163] EBL systems are very similar in design to scanning electron microscopes, in fact, EBL devices can be bought from modified scanning electron microscopes, though their performance is not good as machines designed specifically for lithographic purposes.[164] EBL devices are made up of a chamber, an electron gun, and a column. The electron optical components are housed with the column, and are needed to create the electron beam, to accelerate and focus it and to deflect it in order for the pattern to be written.[164] EBL differs significantly from scanning electron microscopy in that the electrons can be accelerated to a significantly higher voltage in the former.[164] The electron beam is then scanned across the substrate in order to create the desired pattern.

The much smaller wavelengths of electrons mean that in principle electron beam lithography is subject to a smaller resolution limit than photolithography. The effective resolution limit of EBL is not defined by the diffraction limit but by the 'spread' of excitation in the plane of the modified material that expands beyond the electron beam spot. When EBL is used to directly write on the surface and is followed by an etching process, can produce features of 10 nm[165] and even smaller.[166] However, despite this high resolution capability, the electron beam can only pattern one pixel at a time, which results in a very slow throughput which is not practical for the production of semiconductor components on mass.[167]

An issue that has needed to be addressed when using EBL is that of the proximity effect. Due to the high energy nature of the electrons, some of them may penetrate through the resist and into the substrate. Subsequently, the electrons may be scattered back towards the resist, but in an area that was not meant to be exposed, therefore causing potential unwanted patterning. More significantly, these electrons may also result in high energy secondary electrons that can travel up to 100s of nanometres away from the original area,

causing a large amount of unwanted resist exposure.[168] There are numerous models detailing corrections that take the proximity effect but there is debate about the relative merits and accuracies of such models.[169–171] Even taking the proximity effect into account, EBL is still the most widely used fabrication method used for creating high resolution features.

2.5. Conclusion

With the size of features continuing to decrease due to fabrication techniques being created and improved on a frequent basis, the possibilities available for the manufacture and testing of light harvesting behaviour are numerous. Self-assembled monolayers can be used to attach light harvesting molecules to a surface and incorporate photocleavable groups within the systems. Photolithography can be used to vary the densities of light harvesting molecules over such surfaces and their spectroscopic behaviour subsequently monitored. Additionally IL can be used to create metal nanostructures with fixed sizes and shapes and light harvesting molecules can be attached to these nanostructures to see how their behaviour is affected by confinement to a certain space.

Therefore through use of the techniques listed above, the understanding of how light harvesting molecules can obtain, retain and move energy so efficiently can be explored. Eventually, great control can be exerted over the manufacture of sub-100 nm light harvesting systems which, ultimately, is what we should be striving to obtain, because the light harvesting vesicle of *Rba. Sphaeroides* as shown in figure 3 has only a 60 nm diameter and a near unity conversion of light to usable energy.

It is the aim of this project to explore the production of nano-structures of light harvesting molecules, using top-down and bottom-up fabrication methodology including commonly used techniques, but also some that are not widely used, if at all, and identifying their potential for creating smaller feature sizes than the above techniques. Experimental conditions and variables of these new techniques shall be explored such that any desired feature size can be produced. This range of feature sizes will then be applied to protein resistant monolayers, modifying them in such a way that light harvesting proteins and other molecules can be adsorbed and confined within a certain spatial configuration; the effect this

confinement has on the light harvesting properties of these molecules can then be investigated.

3. Tip induced electro-oxidative lithography of silane monolayers

3.1. Introduction

AFM probes have been used to successfully oxidise silicon and other semi-conductor surfaces by applying a potential difference across the tip and the surface and bringing the tip into contact with the surface, creating well defined patterns on the nanoscale.[172–176] Similarly, application of bias induced surface patterning techniques have been shown to promote the oxidation of methyl tail groups of certain silane monolayers to carboxylic acid groups.[177] It should follow on that the technique of applying a bias between an AFM tip and a highly ordered silane monolayer will therefore lead to the formation of nanostructures within a monolayer.

The oxidation process is facilitated by oxidising species (either OH^- or O^-) found in the water film that lies atop the surface of the monolayer and also the water meniscus that forms between the tip and surface. This meniscus also provides a bridge for electrical field required to induce oxidation and controlling the width of the meniscus grants effective control of the width of the features produced.[175] The role of these oxidising species and oxidising process can not be described as a purely electrochemical as no current flow has been detected during the reaction.[173] By varying a range of possible parameters such as the voltage, relative humidity and tip velocity the linewidths of the nanopatterns produced can be expected to vary and therefore optimised to produce features as small as possible.

Experiments would be carried out to with the aim of oxidising methyl terminated silanes such as octadecyltrimethoxy silane (*ODTMS*) and octadecyltrichloro silane (*ODTS*), as oxidation of methyl tail groups have been shown before[177, 178] and the monolayers are easy to make and tests to prove experimental success are simple and quick. Once tip induced

electro-oxidation of methyl terminated silanes had been established, work would be advanced onto other systems such as poly(ethylene glycol) (*PEG*) terminated silanes.

The protein resistance of ethylene glycol groups is well established,[179] and incorporating the functional group into a monolayer through use of a silane is a viable route to manufacturing a protein resistant pattern on the nanoscale.[141] PEG and oligo(ethylene glycol) (*OEG*) can be easily attached to a surface via a silane self-assembled monolayer and oxidised to lose their protein resistance.[180, 181] The aim of this chapter is to use tip induced electro-oxidation to facilitate constructive nanolithography to create nanoscale patterns of light harvesting proteins a few units wide that can be imaged at a high resolution.

3.2. Experimental

Silicon wafers were cut to size and cleaned and placed in individual sample vials and submerged in a solution of soap and deionised water and sonicated for ten minutes, the slides were subsequently rinsed with acetone and then rinsed again three times with deionised water. Piranha cleaning solution was then used and the slides were rinsed seven times with deionised water. These slides were subjected to further cleaning by using the Radio Corporation of America standard clean one (*RCA I*) method and rinsed in deionised water seven times before being placed in an oven set to 120 °C to dry.

The sample vials were taken out of the oven, sealed with a suba seal and flushed with nitrogen. Dry toluene was then added to the vial and ODTS monolayers were created by adding 0.3 mL of octadecyltrichlorosilane to create an approximate 1 % volume : volume solution of silane to solvent. The slides were left in solution for times of between 60-120 minutes, after which they were washed and annealed. Contact angle measurements were taken to test the quality of the monolayer.

OEG monolayers were created by taking sample vials out of the oven, sealing with a suba seal and flushing with nitrogen. Dry toluene was then added to the vial and 0.3 mL of 2-[methoxy (polyethyleneoxy) propyl]-trichlorosilane added to create an approximate 1 % volume : volume solution of silane to solvent. The slides were left in solution for times of between 20-30 minutes, after which they were washed and annealed. Contact angle measurements were taken to test the quality of the monolayer.

The silane films were then placed on the AFM and a potential difference was placed across the tip and sample where the equipment was set-up so that either the sample or the tip could be negative. To oxidise the sample a variety of variables are changed to produce thinner/thicker or more solid/broken features, including tip velocity, the force of the tip onto

the sample, the voltage and the relative humidity. The types of tips used were either tapping mode or contact mode and the electrochemical oxidation process was carried in the contact regime. The tips were either metal coated or bare silicon. Following patterning, samples were rinsed with ethanol and dried with nitrogen gas.

Refunctionalised ODTS bilayers were created by placing patterned ODTS functionalised silicon slides in a piranha and RCA 1 cleaned sample vial which is then flushed with nitrogen. Dry toluene was then added to the vial and 0.3 mL of octadecyltrichlorosilane added to create an approximate 1 % volume : volume solution of silane to solvent. The slides were left in solution for times of between 60-120 minutes, after which they were washed and annealed.

Refunctionalised OEG bilayers were created by placing the patterned OEG functionalised silicon slides in a piranha and RCA 1 cleaned sample vial which is then flushed with nitrogen. Dry toluene was then added to the vial and 0.3 mL of 2-[methoxy (polyethyleneoxy) propyl]-trichlorosilane added to create an approximate 1 % volume : volume solution of silane to solvent. The slides were left in solution for times of between 20-30 minutes, after which they were washed and annealed.

3.3. Results and discussion

3.3.1. Surface characterisation of ODTS films

ODTS monolayers on silicon were formed and characterised using contact angle measurements and XPS. The contact angles were found to be 112 ± 3° and are in a similar range as those in the literature[57, 182] and show a high degree of hydrophobicity which is expected for a highly ordered methyl terminated surface.

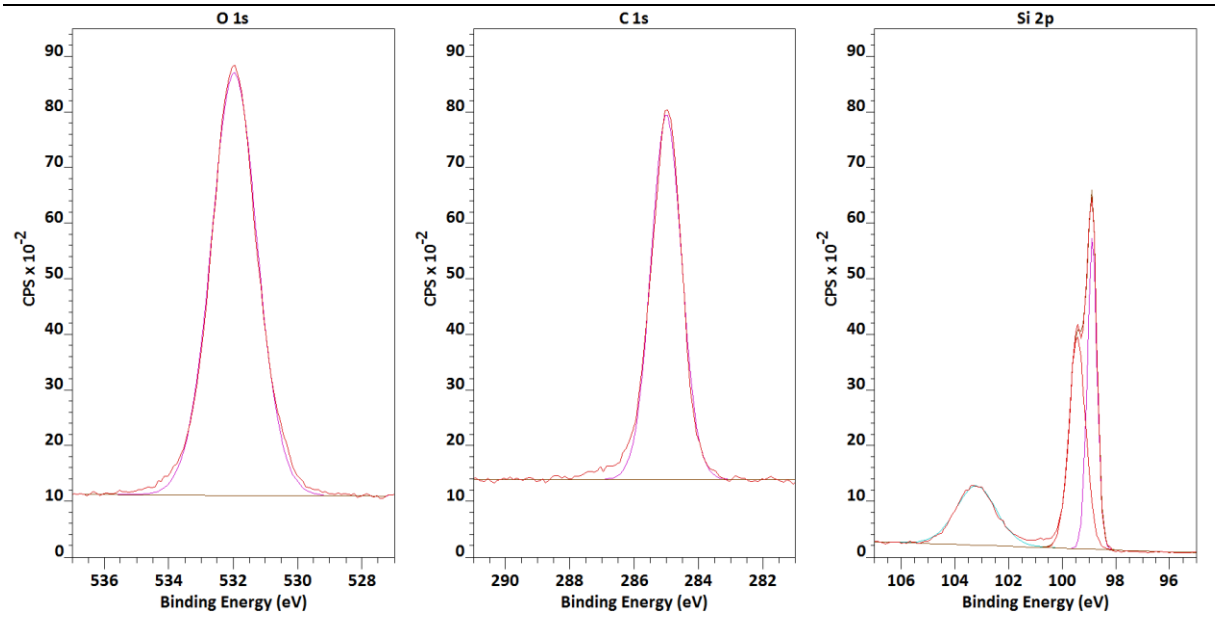

Figure 15. O 1s (left) and C 1s (middle) and Si 2p (right) photoelectron spectra of ODTS monolayers on silicon.

Figure 15 shows the O 1s, C 1s and Si 2p spectra of the ODTS monolayers. The O 1s spectrum displays one peak at 532.0 eV which represents the oxygen in the surface oxide layer of the substrate. In the Si 2p spectrum region a peak is observed at 103.2 eV corresponding to oxidised silicon.[183] The silicon 2p spectrum exhibits a doublet at 98.9 eV and 99.4 eV attributed to the Si $2p_{3/2}$ and $2p_{1/2}$ respectively. There was no evidence of

chlorine in the XPS spectra confirming that hydrolysis of unreacted Si-Cl bonds has occurred during the formation of the monolayer. The C 1s spectrum exhibits a single peak at 285.0 eV which corresponds to the CH_2 / CH_3 units of the alkyl chain.

3.3.2. Nanopatterning of ODTS films

3.3.2.1. Effect of voltage

Nanopatterning was carried out by tip induced electro-oxidation, in which a potential difference is applied across an AFM tip and an ODTS monolayer. A series of patterns at a range of speeds were drawn and for each, the voltage was varied from -1 V being applied to the tip, decreasing by integers to -10 V. The linewidth of the resulting features would be expected to increase as more negative voltages are applied to the tip, for if the potential difference is greater, the ability to carry out and electro-oxidation reaction is increased also. It is also predicted that there will be a critical voltage, below which no change in the surface will be detected.

Figure 16 shows AFM images of an ODTS monolayer on silicon when voltages of -1 V through to -10 V are applied to a tip travelling at a velocity of 0.45 µm s^{-1}. At all speeds, when lower voltages are applied, there is no evidence obtained from AFM imaging that any tip induced electro-oxidation has taken place, whereas for higher voltages there are signs that oxidation has taken place. When imaging the methyl terminated sample post electro-oxidation, in both tapping mode and contact mode, there were visible changes in phase and force images respectively where the tip had been traced across the sample. This suggests that the methyl groups had been oxidised, as a change from a methyl group to an alcohol or aldehyde would result in a significant change in how the surface interacts with the AFM tip. The modified surface contains an increased degree of disorder due to oxidation during the

lithographic step, with the result that more energy is dissipated as the probe slides across the surface giving rise to a change in phase and friction forces.

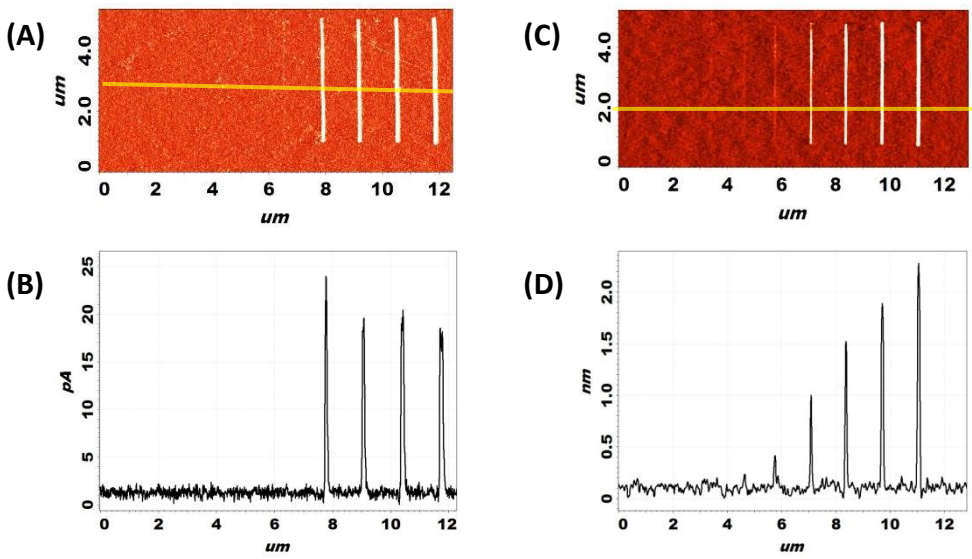

Figure 16. (A) A lateral force AFM image in the forward direction taken in contact mode showing the area where tip induced electro-oxidation has been carried out. The potential difference across the tip for each line increases in integers from left to right from -1 V to -10 V. Only the lines where the voltage was -7 V, -8 V, -9V and -10 V are clearly visible. **(B)** A cross section taken from the yellow line in figure 16A. **(C)** A topography AFM image taken in tapping mode showing the same area as figure 16A. **(D)** A cross section taken from the yellow line in figure 16C.

It can be seen that although there is a clear change in the lateral force in the areas where the voltage was applied to the tip and surface, there is also a corresponding height change as shown by the topographical image in figure 16C and D. This change in height increases as the potential difference increases and can be seen in figure 17. Theoretically,

such a height change should not be seen as a simple transformation of the tail group as that would lead to a minimal difference in the length of the silane, therefore it is possible that in addition to the surface of the monolayer, the silicon oxide substrate below is being induced to grow. This would lead to changes in topography and make the area of the monolayer above it appear higher.

Voltage on tip / V	Height / nm	Full Width at Half Maximum / nm	Lateral Force Intensity / pA
-7	1.04	50	18.85
-8	1.69	75	21.25
-9	1.98	93	21.60
-10	2.35	90	19.95

Figure 17. A table showing the heights, full widths at half maximum (*FWHM*) of the lines and lateral force intensities of the lines shown in figure 16. All values are calculated as an average of 10 points taken on each line. Height and FWHM values were calculated from tapping mode images and lateral force intensity is an absolute value calculated from contact mode.

Figure 17 shows that as the voltage is increased for a constant tip velocity the width of the feature increases. This suggests that in order to create the smallest possible features, there is an optimal value for the potential difference such that oxidation of the surface can take place but not to such an extent that line broadening occurs. A long term goal is to establish this ideal voltage by optimising tip velocity, set point and voltage.

Figure 18 shows a plot of feature width against the potential difference for a series of lines written for a range of constant voltages, where the AFM scanner speed was varied from between 0.15 µm s^{-1} and 4.00 µm s^{-1}. The results show the relationship between feature FWHM and probe voltage for each of the chosen speeds. For each speed it can be seen that the feature width decreases with increasing potential difference, agreeing with the data in figure 17.

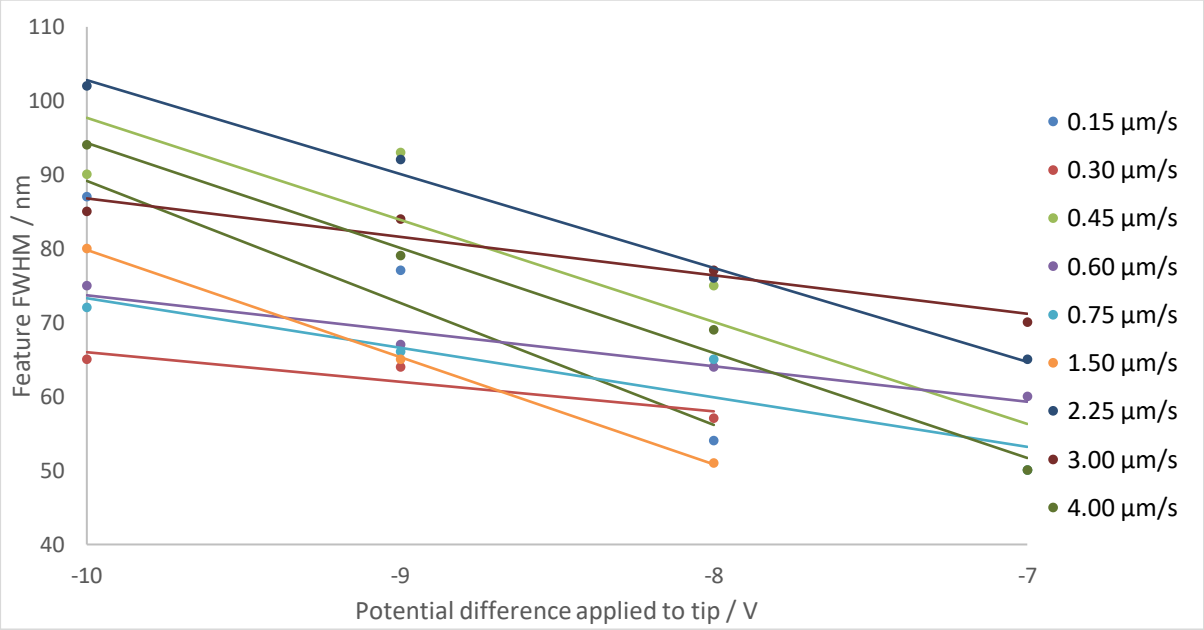

Figure 18. A graph showing how ODTS monolayer feature FWHMs vary with voltage, carried out over a range of speeds. The values for FWHMs are an average of the FWHM of ten points on each line.

3.3.2.2. Effect of tip velocity

A series of lines were written where for a given scanner speed, the voltage was varied. Figure 19 shows the feature width as a function of tip velocity and there does not appear to be a correlation.

It would be expected that as the speed of the scanner is increased, the tip will be in contact with each point on the line for less time and therefore there will be less time for oxidation to take place and shorter, narrower features should result. As scanner speed increases, it is also possible that the water meniscus between the tip and the surface can not establish and so the medium for the electro-oxidation to occur is removed, preventing a nanopattern from being drawn. However, such a trend is not observed implying that the tip velocity does not have as strong effect on the feature width as voltage.

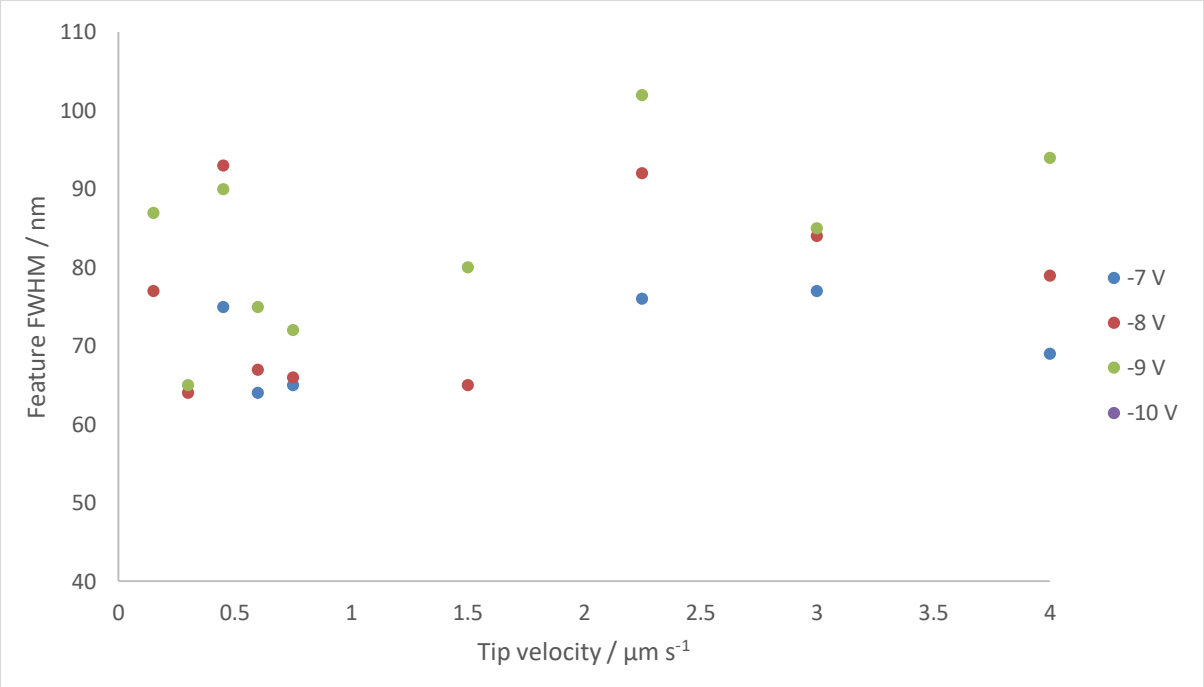

Figure 19. A graph showing feature FWHM in relation to the tip velocity across an ODTS monolayer.

3.3.2.3. Refunctionalisation of patterned ODTS regions

By immersing the sample in a silane solution after the writing process, the extent of oxidation could be tested, for if methyl groups have been oxidised to contain oxygen in some form, then a silane should grow on these areas, which would lead to a significant change in the topography of the surface, and if the original silane was used, any previous change in force and phase would be effectively negated. Figure 20 shows images taken after the sample that has been exposed to tip induced electro-oxidation, is then placed in a solution of ODTS.

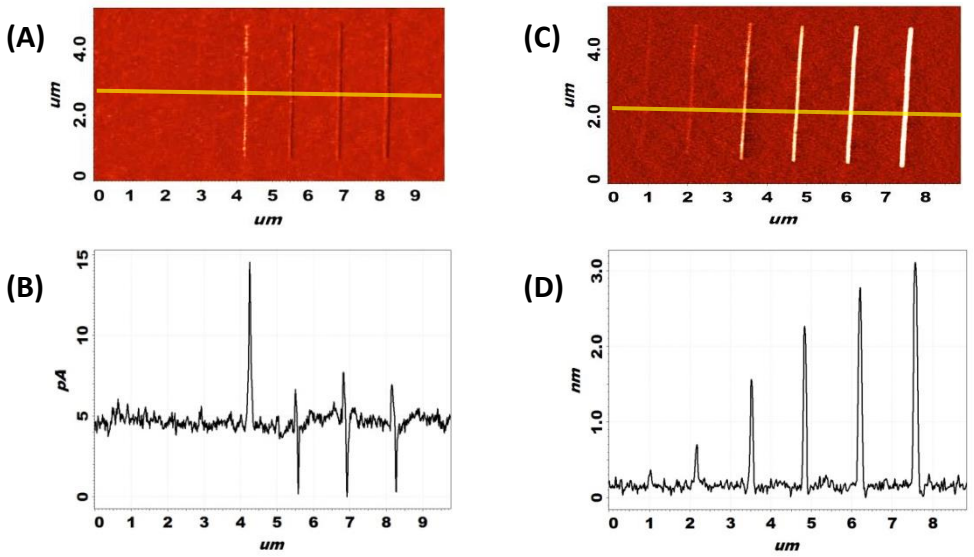

(E)

Voltage on tip / V	Height / nm	Lateral Force Intensity / pA
-7	1.91	8.35
-8	2.27	3.95
-9	2.60	4.25
-10	3.18	4.45

Figure 20. (A) A lateral force AFM image in the forward direction taken in contact mode showing part of the area where tip induced electro-oxidation has been carried out in figure 16 and the placed in a solution of ODTS. Only the lines where the voltage was -7 V, -8 V, -9V

and -10 V are clearly visible. **(B)** A cross section taken from the yellow line in figure 20A. **(C)** A topography AFM image taken in tapping mode showing the same area as figure 20A. From left to right the lines visible are -5 V, -6 V, -7V, -8V -9 V and -10V. **(D)** A cross section taken from the yellow line in figure 20C. **(E)** A table showing the heights and lateral force intensities of the lines in figure 20A-D. All values are calculated as an average of 10 points taken on each line. Height and FWHM values were calculated from tapping mode images and lateral force intensity is an absolute value calculated from contact mode.

If the data in figure 17 and figure 20 is compared it can be seen that after the sample has been submerged in ODTS for a second time an increase in height and a reduction in the absolute lateral force intensities can be observed. The values for the lateral force have dropped, implying that any oxygen containing groups that were on the surface post-oxidation have successfully reacted with a silane molecule to create a bilayer. Figure 20 shows the change in lateral force is towards zero, suggesting that the oxidised areas have changed to something with a similar nature to that of the rest of the surface, implying the successful creation of a bilayer.

Figure 20 shows that the oxidised areas undergo a height change and whilst this is to be expected if the oxidation of the ODTS was successful, the magnitude of the changes was not. The literature values for the length of ODTS is between 2.26 and 2.90 nm[182, 184, 185] and the changes of height after the second silanisation process range from between 0.58 to 0.87 nm which are significantly less than this value. The changes in height for all speeds are displayed in figure 21 and only the lines drawn at 4.00 μm s^{-1} have a height increase in this range, which is contrary to prediction, as faster tip travel across the surface should hinder tip induced electrochemical oxidation of the monolayer and thus the size of any bilayer grown in

that area. Whilst there is an increase in height in all the areas, there is no discernible trend relating this increase to voltage and tip velocity. This is an area for further investigation as it would appear that the relationship between the independent variables is not as clear cut as it would seem in theory.

	Tip Velocity / µm s^{-1}								
Voltage on Tip / V	**0.15**	**0.30**	**0.45**	**0.60**	**0.75**	**1.50**	**2.25**	**3.00**	**4.00**
-7			+0.87	1+.62	+0.03		+1.32		
-8	+0.76	+0.92	+0.58	+1.01	+0.68	+0.55	+2.70	+0.83	+2.44
-9	+1.16	+0.87	+0.62	+0.90	+0.86	+1.29	+1.78	+1.15	+2.23
-10	+1.12	+0.96	+0.83	+1.11	+0.43	+1.01	+1.20	+1.57	+2.88

Figure 21. Table showing the changes in height in nm of the oxidised areas after a second submersion in ODTS for all speeds carried out.

3.3.3. Surface characterisation of OEG functionalised silane films

The technique of tip induced electrochemical oxidation has been reproduced successfully and then applied to OEG films, in particular 2-[methoxy (polyethyleneoxy) propyl]-trichlorosilane. These OEG films are of particular interest because they are protein resistant, however, upon oxidation they become receptive to the binding of proteins[115] which opens up the potential of creating lines of, for example LH2, that are 100s and possibly 10s of nanometres wide. Films of 2-[methoxy (polyethyleneoxy) propyl]-trichlorosilane were prepared and characterised by contact angle analysis and XPS. The contact angles of the films were 45 ± 3° which are within the range of values for ethylene glycol terminated silanes quoted in the literature.[141]

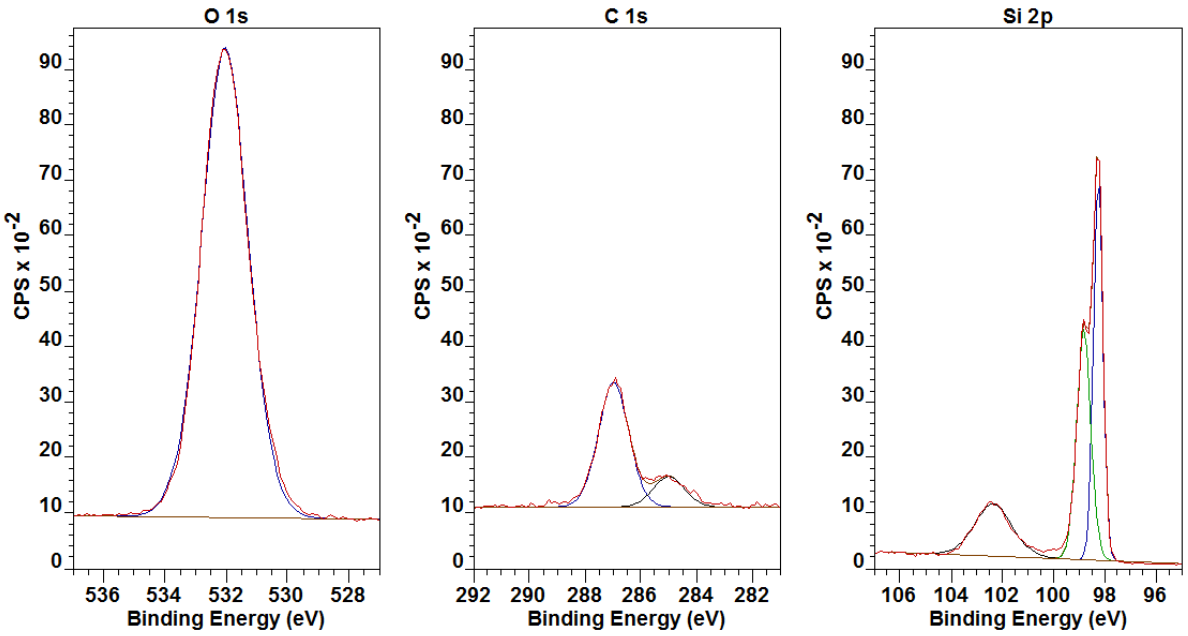

Figure 22. O 1s (left) and C 1s (middle) and Si 2p (right) photoelectron spectra of 2-[methoxy (polyethyleneoxy) propyl]-trichlorosilane monolayers on silicon.

The O 1s and Si 2p XPS spectra in figure 22 are very similar to those in figure 15 as they represent the bulk silicon and oxide layer of the substrate. However the C 1s spectrum is markedly different. Two prominent peaks are observed at 287.0 eV and 285.0 eV, where the former corresponds to the carbon environment adjacent to electron withdrawing carbon with the ethylene glycol group, while the latter corresponds to emission from carbon atoms in the hydrocarbon tether linking the OEG group to the substrate.

3.3.4. Nanopatterning of OEG functionalised silane films

The same controls that were applied when performing tip induced electrochemical oxidation on ODTS were maintained for tip induced electro-oxidation of 2-[methoxy (polyethyleneoxy)

propyl]-trichlorosilane i.e. tip velocity and voltage applied to the tip, in addition to this, experiments were performed where the force applied to the tip was varied.

3.3.4.1. Effect of voltage

For a given speed and force applied to the tip, a range of voltages were applied and the tip moved across a monolayer of 2-[methoxy (polyethyleneoxy) propyl]-trichlorosilane. There were similarities between the ODTS and OEG system when the potential difference across the tip was changed, such as that no evidence of oxidation was present when a voltage of -6 V inclusive and greater (i.e. towards 0 V) was applied and evidence for oxidation was visible for voltages less than or equal to -7V. As for the ODTS system, when the most negative voltages were applied to the tip the features that were produced yielded the widest line width, as shown in figure 23.

The feature width appears to level off between -7 V and -8 V which suggest that the relationship between voltage and feature width is not necessarily linear. Future work is to study more in depth this range of voltages in order to determine the voltages at which feature width starts to significantly increase and also at which voltage evidence of oxidation becomes apparent in order to determine the optimum voltage for producing the narrowest lines.

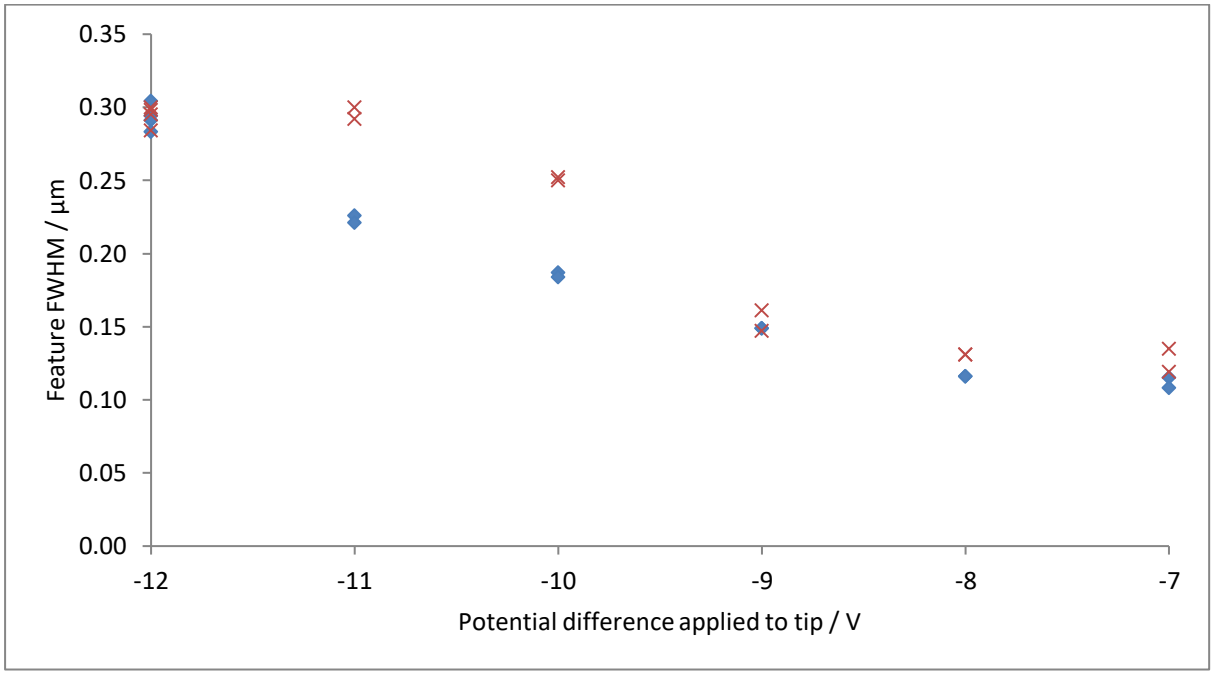

Figure 23. The feature full width at half maximum as determined from topographic AFM data (blue diamonds) and frictional AFM data (red crosses) for varying potential differences for a 2-[methoxy (polyethyleneoxy) propyl]-trichlorosilane monolayer on silicon. Tip velocity was 2.0 µm s^{-1} and the force applied to the tip was 50 nN.

3.3.4.2. Effect of tip velocity

When the velocity of the tip is varied with a constant voltage and force applied, no obvious trend is observed as shown in figure 24. The FWHMs of the oxidised features are between 166 nm and 239 nm and similarly to the ODTS system shown in figure 19, the apparent widths of the features do not decrease as the velocity of the tip increases. Once an "ideal" voltage to apply to the tip has been determined, varying the tip velocity, including those

greater than 11 µm s^{-1}, for this voltage may yield results more in keeping with those expected.

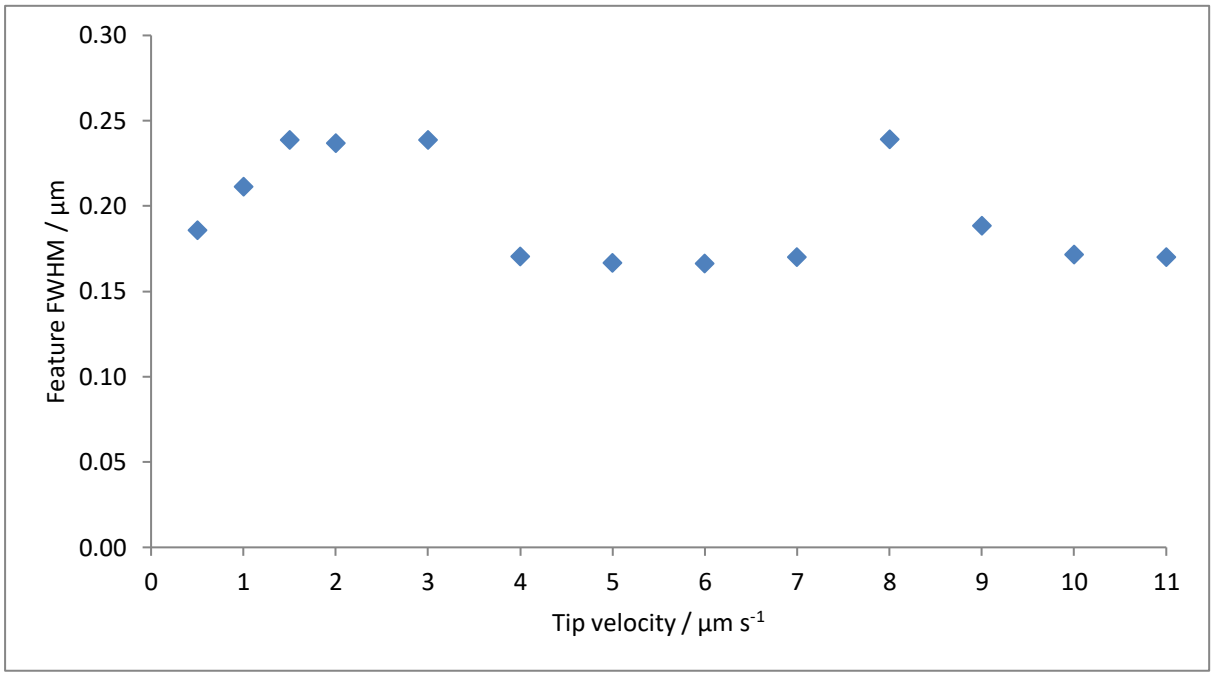

Figure 24. Feature full width at half maximum of oxidised 2-[methoxy (polyethyleneoxy) propyl]-trichlorosilane monolayer on silicon as determined by topographical AFM against varying tip velocities. A voltage of -12 V and a force of 50 nN was applied to the tip.

3.3.4.3. Effect of force

A series of lines were written in which the voltage and tip velocity were constant and the force applied to the tip is varied. Figure 25 shows that for forces between 1 – 100 nN the FWHM does not vary significantly, however from 500 nN and greater the FWHM begins to trail off and narrow. When a greater force is applied to the tip, theoretically this should lead to the capillary of water between the tip and sample becoming wider and thus the lines

created by the oxidative process should become wider. Figure 25 however shows that upon inspection this is not the case.

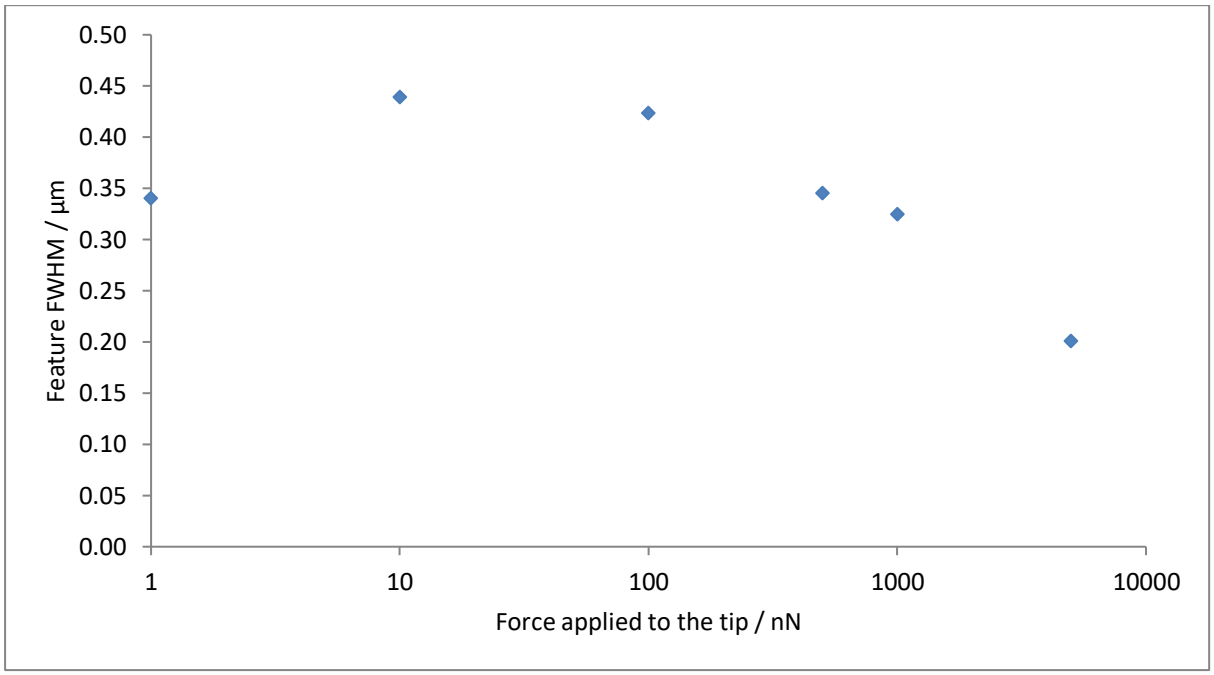

Figure 25. Feature full width at half maximum of oxidised 2-[methoxy (polyethyleneoxy) propyl]-trichlorosilane monolayer on silicon as determined by topographical AFM against varying forces applied to the tip. A voltage of -12 V and a speed of 2 µm s^{-1} was applied to the tip.

At low forces the feature width become wider as the force increases, however beyond approximately 50 nN as the force increases the feature widths decrease. This is possibly a result of a physical deformation of the tip when large loads are applied, though more likely is that at a certain threshold the tip will penetrate the silane monolayer and start slicing through it. This will have the effect of narrowing the meniscus between probe and sample, if not

completely removing it causing oxidation of the molecules in direct contact with the tip and the immediate surrounding area.

3.3.4.4. Effect of deformation of the tip

In addition to the factors mentioned above that can affect the quality and size of any features produced by tip induced electro-oxidative lithography, physical changes to the tip used in the writing process may have an effect on the feature size. An additional experiment was carried out to determine whether the AFM tip used in the writing process undergoes oxidation itself, resulting in silicon oxide growth. In order to test this, a new tip was used to carry out tip induced electro-oxidation of 2-[methoxy (polyethyleneoxy) propyl]-trichlorosilane with a tip velocity of 0.1 μm s^{-1} for an extended time period of approximately 50 minutes. The results are displayed in figure 26.

It can be seen from figure 26 that as time elapses, the FWHM increases. A reason for this is that as a potential difference is applied to the silicon tip, the oxide layer grows and thus the tip diameter will increase, leading to widening feature widths. However, growth of silicon oxide would result in the tip becoming less conductive and therefore would be less able to oxidise the sample. Another possibility is that over long periods of time the tip loses it sharpness and blunts. A future experiment will be to perform the same experiment at a higher voltage. If the line broadening occurs at a slower rate, the effect can be attributed to growth of the oxide layer, if however, broadening occurs at the same rate as the more negative voltage, then the feature widening can be attributed to the tip becoming blunted over time. Regardless of the precise nature of why the lines widen over time, the effect should be carefully considered when optimising parameters, as using an old tip may result in wider lines than a fresh tip, which may be incorrectly attributed to a change in a control variable.

(A)

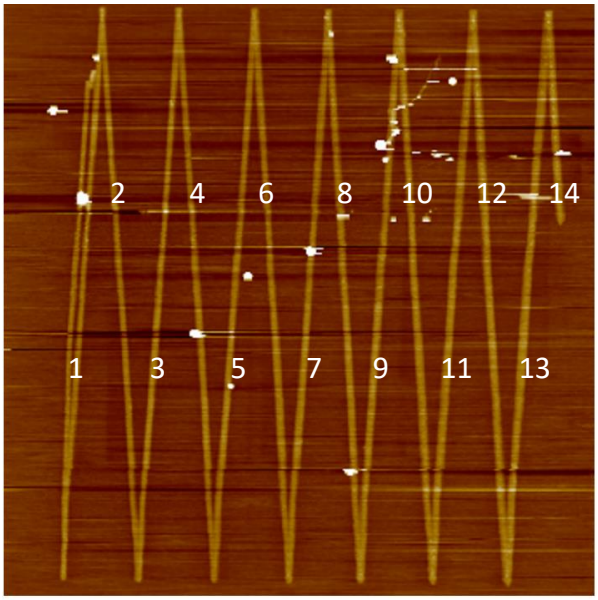

(B)

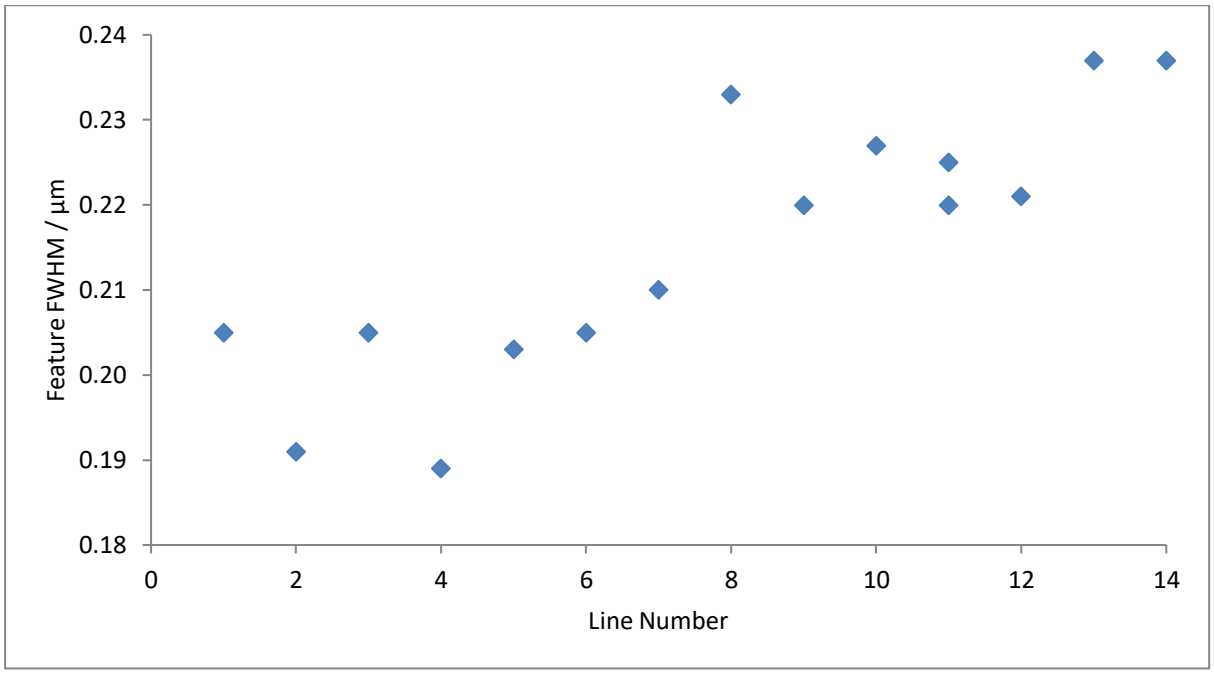

Figure 26. (A) A topographical AFM image of oxidised 2-[methoxy (polyethyleneoxy) propyl]-trichlorosilane. The pattern was written from left to right, where the tip was new for the feature labelled 1. **(B)** The FWHM of the lines corresponding to the labels shown in (A).

The process of degrading 2-[methoxy (polyethyleneoxy) propyl]-trichlorosilane should result in a loss of height, however the topographical image in figure 26 A provides evidence that the silicon oxide layer is thickening during the writing process, as it can be clearly be seen that there is a height increase in the oxidised area.

3.3.4.5. Refunctionalisation of patterned OEG regions

A test was done in order to prove that oxidation of the 2-[methoxy (polyethyleneoxy) propyl]-trichlorosilane had occurred and that the features were not solely of growth of the native oxide of the substrate. The sample shown in figure 26 A was placed in a solution of ODTS and worked up as before. The resulting height difference between the bilayer and monolayer is displayed in figure 27.

A height increase would suggest that the OEG groups had been cleaved from the surface to leave the bare silicon oxide and that ODTS had bound to the substrate. If there is no change in height after being immersed in ODTS solution, then it is probable that the OEG groups had been degraded to aldehydes and thus no sites for ODTS to bind to were available in the monolayer.

The data shows that the greatest height difference was only 0.43 nm and there were some areas where the height appeared to decrease a small amount. Should the OEG groups at the surface of the monolayer have been oxidised then the ODTS will not bind to the resulting aldehyde groups and a bilayer will not be formed. If the silane had been cleaved from the surface, then ODTS will easily bind to the exposed silicon oxide resulting in a height change. If a bilayer was formed then there would have been a height increase corresponding to the length of an ODTS molecule of between 2.26 and 2.90 nm.[182, 184, 185] As there was no height change of this scale, this would suggest that tip induced electro-oxidation resulted in the degradation of the OEG groups and the formation of aldehyde terminated features.

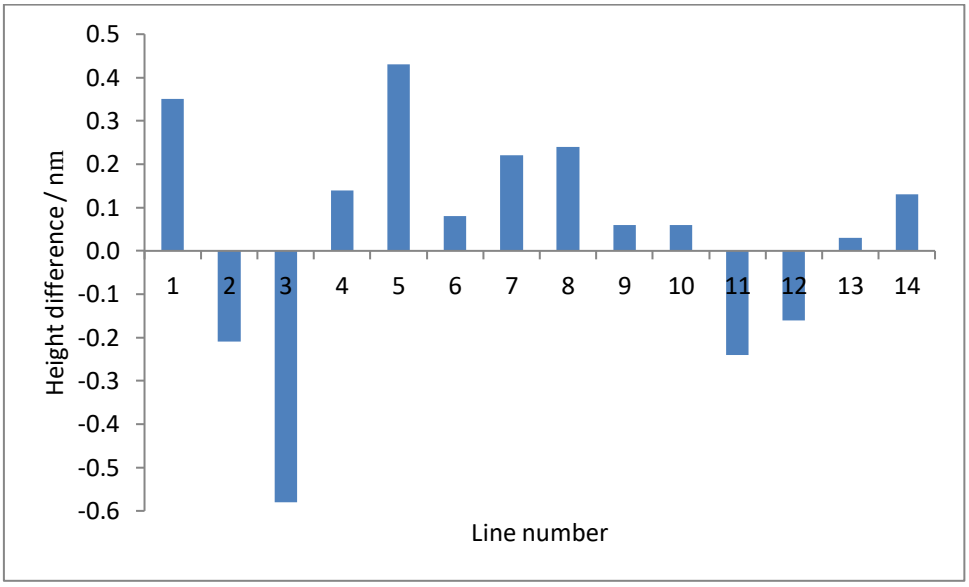

Figure 27. The height difference when the height of the 2-[methoxy (polyethyleneoxy) propyl]-trichlorosilane monolayer is subtracted from the 2-[methoxy (polyethyleneoxy) propyl]-trichlorosilane/ODTS bilayer. The line numbers correspond to the labels on figure 26 A.

It is possible that an ODTS bilayer did not form because the native 2-[methoxy (polyethyleneoxy) propyl]-trichlorosilane had not been oxidised at all and that only growth of the silicon oxide had occurred. Data from figure 26's corresponding friction AFM image suggests that there is a chemical change at the surface in the exposed areas which suggest that this is not the case. An additional experiment can be carried out to prove that a chemical change has occurred on the surface of the monolayer. This would involve exposing a sample that has undergone tip induced electro-oxidation to a protein marker such as green fluorescent protein. The marker would only be able to bind to the areas that had been oxidised and thus lost their protein resistivity and could be easily detected and imaged due to their fluorescent

properties. If no degradation has occurred then a protein marker would be unable to bind to the original monolayer and thus no fluorescence would be detected.

3.4. Conclusions

It can be concluded that varying the voltage has the greatest effect on the line widths as making the voltage more negative by approximately a factor of two results in a widening of features by approximately a factor of three. However, when the load applied to the tip is increased by over three orders of magnitude, the FWHM is reduced by a factor of approximately only two, and the variation of the tip velocity results in a negligible change to the feature size. In order to create the smallest features, optimisation of the parameters should therefore focus on determining the best voltage that should be applied to the tip. The significance of the role that voltage applied to the tip has is further highlighted in the data that was used to produce figure 23. This shows that no oxidation occurs at a voltage of -6 V or above, suggesting the process of oxidising the 2-[methoxy (polyethyleneoxy) propyl]-trichlorosilane is driven by electric field effects and is not a not tribochemical process or force driven as a minimum voltage is required to form the liquid bridge between the tip and the surface.

3.5. Future work

Aldehydes produced after the degradation of OEG groups can then react with an amine containing nitrilotriacetic acids via an imine bond formation, which in turn can react with nickel. This Ni terminated feature is then able to bind to a histidine (*His*) tagged protein creating an alternative route to protein specific adsorption.[181]

The oxidation of OEG groups is a simple degradation process and to further test the potential of this technique for chemical modification, tip induced electro-oxidation on molecules that undergo a site specific chemical reaction should be carried out. One such molecule is [4-(Chloromethyl)phenyl]trichlorosilane (*CMPTS*) which reacts to exposure of UV light to produce a carboxylic acid terminated layer, see figure 28, and such a surface has the potential to bind to biological moieties.[186] If tip induced electro-oxidation of a CMPTS monolayer resulted in a carboxylic acid terminated features then it would be proof that the technique is capable of carrying out specific chemical reactions which opens many routes of creating protein patterns on the nanoscale.

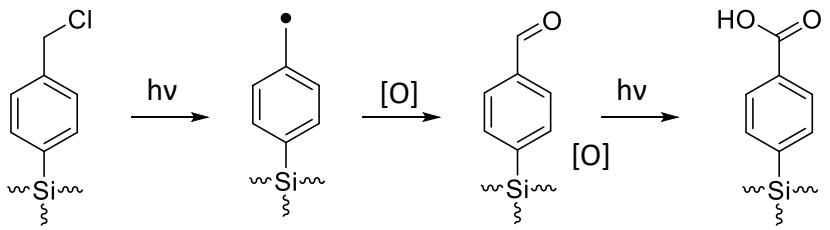

Figure 28. The sequence of steps that results in 4-chloromethylphenylsiloxane SAMs being carboxylic acid terminated.

In addition to oxidising CMPTS, there are many other methods of producing nanopatterns in protein resistant surfaces that utilise ultraviolet light that could be explored such as nitrophenylethyoxycarbonyl-protected aminopropyl- triethoxysilanes. In this case, the nitrophenylethyoxycarbonyl group protects the amine found in the aminosilane, until the molecule is exposed to light of 325 nm wavelength or lower and the protecting group is removed and a free amine is exposed enabling further chemistry to be carried out at these sites.[141] If tip induced electro-oxidation could be used to perform a specific deprotection it opens up yet another route of allowing proteins to bind to a surface they would otherwise be unable to.

The long term goal for this chapter is to be able to produce nanostructures with linewidths as small as 10s of nanometres and selectively attach light harvesting compounds such as LH2 to these nanolines and investigate their behaviour.

4. Tribochemical modification of OEG-NPEOC-APTES

4.1. Introduction

With the desire to expand upon and improve the existing capabilities of nanotechnology comes an increased demand for changes to nanofabrication techniques. Within this chapter both top-down and bottom-up fabrication techniques based around the molecule oligo(ethylene glycol) nitrophenylethoxycarbonyl protected aminopropyltriethoxysilane (*OEG-NPEOC-APTES*) shall be explored as a potential means to create protein patterns of only 10s of nanometres in size.

OEG-NPEOC-APTES can roughly be described as being made up of three components, each of which perform a function that when combined produce a molecule of great interest.

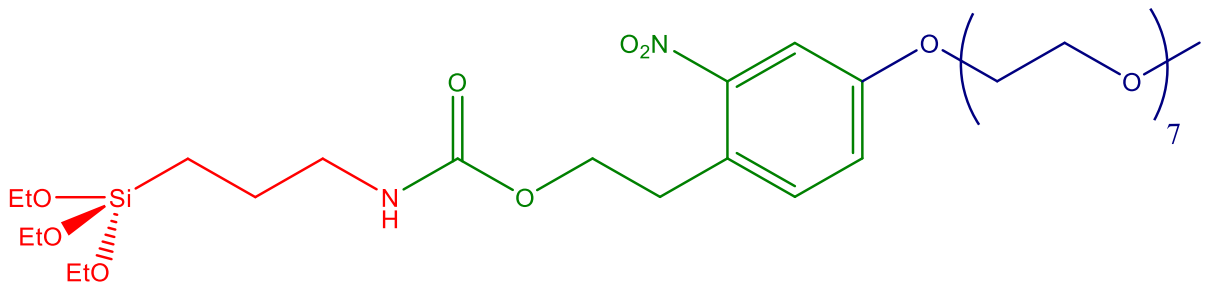

Figure 29. The structure of OEG-NPEOC-APTES. The red part of the structure is the APTES unit. This silane unit allows the OEG-NPEOC-APTES to self-assemble and form a compact monolayer. The green part of the structure corresponds to an NPEOC protecting group, which can be removed to expose the amine of the APTES group for further reaction. The blue part of the structure is a heptaethylene glycol adduct, which primarily adds protein resistivity to the moiety.

Because of its resistivity to biological fouling and its photocleavable protecting group, OEG-NPEOC-APTES has been used as a means of producing nanopatterns of proteins.[141, 187, 188] This is done by irradiating the molecule with UV light in order to remove the protecting group, and simultaneously the ethylene glycol units, thus exposing free amines on the surface. These amines can be further reacted in such a way that a protein pattern is generated by utilising the widely used system of binding nitrilotriacetic acid (*NTA*) to a His-tagged protein.[189, 190] Feature sizes in the region of 100's of nanometres can be produced when a SNOM is used to generate these patterns.[141, 187, 188]

When used for nanopatterning, SNOM as a technique for lithography can be expensive, time consuming and challenging, as it requires specialist probes to be produced to carry a laser light to the surface, which must in turn be coupled with a feedback loop to keep the end of the probe an appropriate distance from the surface. With these probes costing many hundreds of pounds per item, and from previous experience that the probes are liable to be damaged easily despite great care being given in their use, an alternative method for deprotection of OEG-NPEOC-APTES on the nanoscale has been sought.

It shall be explored, whether using an AFM probe to impart mechanical energy into the surface of an OEG-NPEOC-APTES monolayer can replicate the conditions by which a photochemical reaction occurs when a photon is adsorbed by the molecule leading to its deprotection. Mechanochemistry has already been demonstrated on thiols on gold,[191, 192] however the process that occurred in such experiments is believed to be a lateral displacement of the molecule, rather than its complete removal. Further adding to the complexity of the tribochemical lithographic process proposed is that the desired effect is not that of removal of the whole molecule from the substrate, but rather the breaking of a specific bond within the molecule, a schematic for which is shown in figure 30.

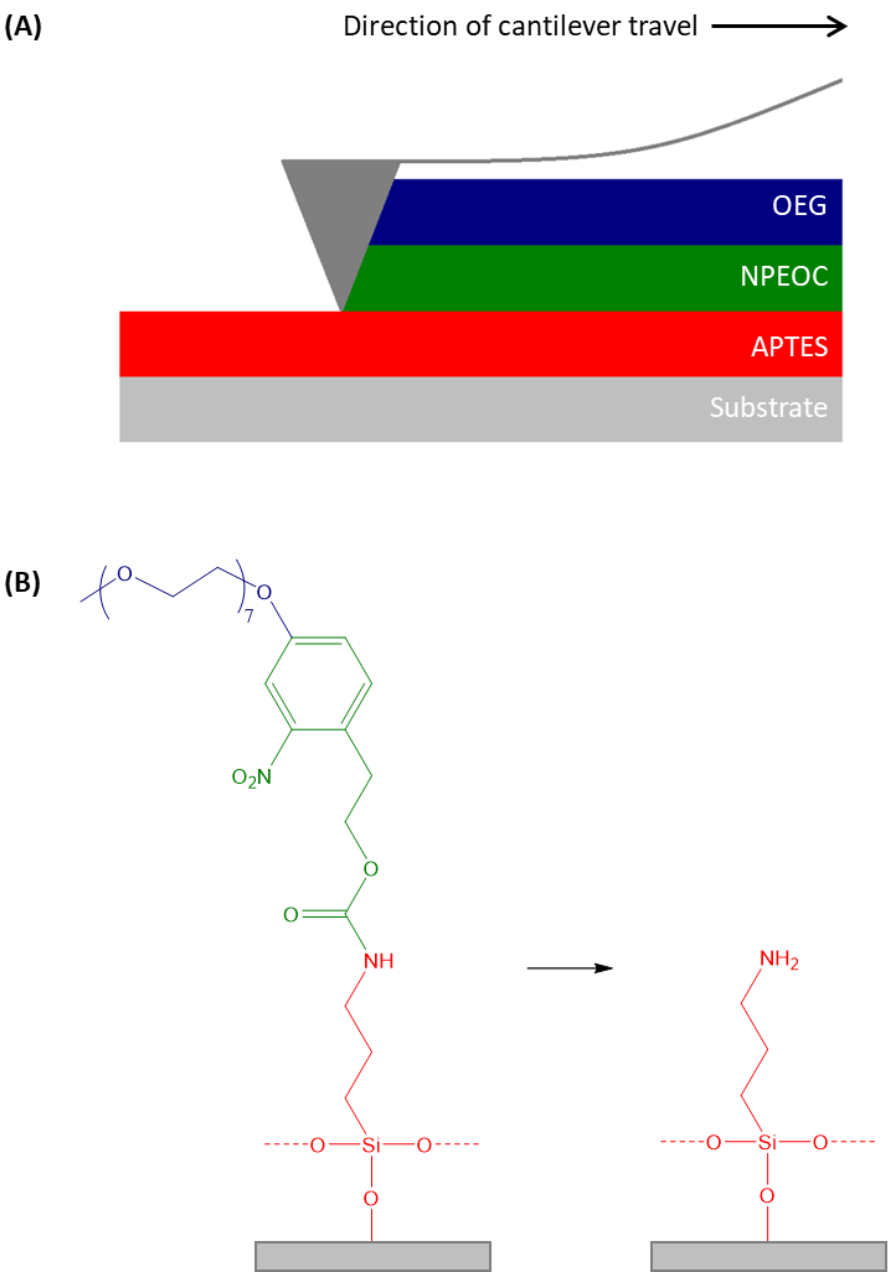

Figure 30. (A) A schematic of the selective deprotection of OEG-NPEOC-APTES through force applied through an AFM tip, leaving the amine from the APTES part of the moiety free on the surface to undergo further reaction. **(B)** The structure of OEG-NPEOC-APTES before and after the removal of the protecting group.

By carrying out nanofabrication in this way, the process becomes much more accessible, as only an AFM and probes are needed. This removes the need to have specialised pieces of equipment in order to carry out the lithography, such as a SNOM or other photolithographic set-up. Instead, a large quantity of variables can be changed by changing the probes used in the lithographic process as they can vary in a range of sharpness, stiffness and functionality.

Polymer brushes are also an area of high interest because they can be designed in such a way that they are also resistant to biological fouling, similar to OEG-NPEOC-APTES.[193, 194] Through careful control and simple photolithographic processes, nano- and microscale patterns of polymer brushes can also be designed in such a way that they can be used to support lipid bilayers such that they can be monitored in situ, a task that is otherwise problematic.[195, 196] Exploration of membrane and lipid behaviour can facilitate exploration of many biological processes, including that of bacterial photosynthesis.[9, 197] Poly(cysteine methacrylate) is of particular interest as it is zwitterionic and based on its pH, can be resistant to fouling or not,[194] and its growth can be controlled readily using atom transfer radical polymerisation (*ATRP*), a technique that has proved widely popular for growing polymers from the surface upwards.[198]

These processes however often require exposure to UV light to pattern an initiator, but if one such step could be replaced with a tribochemical lithography step, then it opens the possibility of having smaller regions of polymer brush or even areas of three or more different polymer brushes. It has been shown that a molecule containing a photoprotecting group that is remarkably similar to the one present in OEG-NPEOC-APTES can be modified by UV light and from the resulting amine, a polymer brush grown.[195] This suggests therefore that it would be possible to replicate these results using OEG-NPEOC-APTES and grow polymer brushes from tribochemically modified surfaces.

4.2. Experimental

Silicon wafers were cut to size and cleaned and placed in individual sample vials and submerged in a solution of soap and deionised water and sonicated for ten minutes, the slides were subsequently rinsed with acetone and then rinsed again three times with deionised water. Piranha cleaning solution was used, and the slides were rinsed seven times with deionised water. These slides were subjected to further cleaning by using the RCA I method and rinsed in deionised water seven times before being placed in an oven set to 120 °C to dry.

OEG-NPEOC-APTES monolayers were created by adding dry toluene to a vial taken from the oven and 0.03 mL of OEG-NPEOC-APTES added to create an approximate 0.1 % volume : volume solution of silane to solvent. The vials were then sealed and nitrogen gas bubbled through for 5 minutes. The slides were then place in dark conditions and left in solution for times of between 24-48 hours, after which they were washed and annealed. Contact angle measurements were taken to test the quality of the monolayer.

The nanomechanical modification of the OEG-NPEOC-APTES surfaces was done by bringing a tapping mode tip into contact with the surface. Tapping mode tips were used as they are stiffer than contact mode tips which was found to provide better results. A desired load was applied to the tip after which scanning started. Following the lithographic process, the samples were washed in phosphate buffered saline solution (*PBS*) which made up according manufacturers specifications by dissolving tablets in water such that a pH 7.4 solution was produced. Samples were then dried with nitrogen gas.

Attachment of proteins to modified OEG-NPEOC-APTES is as follows. The free amines were reacted with a 25% volume : volume glutaraldehyde (*GA*) in water solution for 1 hour at pH 5 in order to derivatise the modified areas with an aldehyde terminated surface. An aqueous solution of 10 mM (S)-N-(5-Amino-1-carboxypentyl)iminodiacetic acid

(*ABNTA*) adjusted to pH 5.1 was made up and the aldehyde functionalised surfaces immersed for approximately 16 hours in order to produce a NTA terminated region. The NTA surfaces were then immersed in an aqueous 500 mM solution of $NiCl_2$ for 2 hours. A His-tagged green fluorescent protein (*GFP*) in PBS solution, pH 7.4, was created and the samples covered in protein solution and then placed in a fridge overnight. Prior to fluorescence microscopy, the samples were rinse with fresh PBS, then a gentle rinse with deionised water before being dried with nitrogen gas.

OEG-NPEOC-APTES selectively bound to finder grid patterns were created as follows. Slides were taken from the oven and placed in the thin film evaporator with finder grids placed between the evaporation source and the slides. Approximately 20 nm of chromium was evaporated through the grids onto the slides, followed by 40 nm of gold. The slides were then placed in a 10 mM solution of dodecanethiol in degassed ethanol for 18 hours. The slides were then washed and placed in clean sample vials from the oven and then immersed in a 0.1 % volume : volume solution of silane to solvent of OEG-NPEOC-APTES in toluene, before being flushed with nitrogen gas for 5 mins. The sample vials were then wrapped in foil and left for 48 hours. The slides were then washed and placed in the vacuum oven.

APTES monolayers were produced as follows. Sample vials were taken out of the oven, sealed with a suba seal and flushed with nitrogen. Dry toluene was then added to the vial and 0.3 mL of (3-aminopropyl)triethoxysilane added to create an approximate 1 % volume : volume solution of silane to solvent. The slides were left in solution for 2 hours, after which they were washed and annealed. Contact angle measurements were taken to test the quality of the monolayer.

The growth of PCysMA from amine terminated surfaces was carried out as follows. Firstly the amines need to be derivatised with the polymerisation initiator molecule. A 0.1 M solution of α-bromoisobutyryl bromide (*BiBB*) in dichloromethane (*DCM*) was made up with 1 : 0.95 : 0.2 molar equivalents of BiBB : triethylamine (*TEA*): water. Alternative initiators in the form of 2-bromoisobutanoic acid N-hydroxysuccinimide ester (*BiBNHS*) and 2-bromoisobutyric anhydride (*BiBAn*) can also be used and in such cases are made up as 0.1 M solutions in DCM with 1 : 0.95 molar equivalents of BiBNHS/BiBAn : TEA. The polymer solution was made as follows. 0.75 g of cysteine methacrylate monomer was ground into a fine powder then dissolved in 4 mL of deionised water. 100 mg of ascorbic acid was dissolved in 10 mL of deionised water, of which 0.18 mL was added to the monomer solution. A further solution consisting of 5 mL of deionised water, 5 mL ethanol, 14.6 mg of copper(II) chloride and 38.8 mg of 2,2'-bipyridyl (*BIPY*) was made, of which 0.35 mL was added to the monomer solution. After 5 mins the monomer solution was ready for use and the samples were immersed for times from 30 seconds – 2 hours.

4.3. Results and discussion

4.3.1. Surface characterisation of OEG-NPEOC-APTES

OEG-NPEOC-APTES films were made and contact angle measurements were carried out. Contact angles were found to be on average 44 ± 3° which was in agreement with literature values.[141] XPS characterisation was also carried out.

Figure 31 shows two regions in the N 1s high resolution spectrum, a peak at 400.09 eV and a peak at 406.18 eV which correspond to the amine group and the nitro group respectively. Though the regions should be equal in size, they are not, this is however consistent throughout every repeat measurement taken.

The C 1s spectrum yields three peaks. The largest peak is the one at 286.7 eV corresponding to the ether carbon atoms in the OEG-functionalized protecting group. A smaller hydrocarbon peak is observed at 285.0 eV, which corresponds to carbon atoms in the aromatic ring and in the propyl linker. The smallest peak at 289.55 eV corresponds to the carbamate carbon, which is double bonded to oxygen and single bonded to both oxygen and nitrogen.

SIMS spectra was also collected figure 32 show the negative ion spectra for the m/z range of 0-800. Present are some of the key ion fragments that can be used to identify OEG-NPEOC-APTES, such as the NO_2^- fragment at 46 m/z from the photoprotecting group, CN^- at 26 m/z which is from the carbamate and C-NO_2 bond. Figure 33 shows the positive ion spectra for the same range was also collected. Present are key peaks such as the carbamate fragment, $COONH^+$ at 59 m/z, the end of the OEG chain, CH_2OCH^+ at 45m/z, as well as regular repeating units for ethylene glycol chain that vary by 16 and 28 m/z, which correspond to O^+ and C_2H_2/CO respectively, within the range of 200-400 m/z.

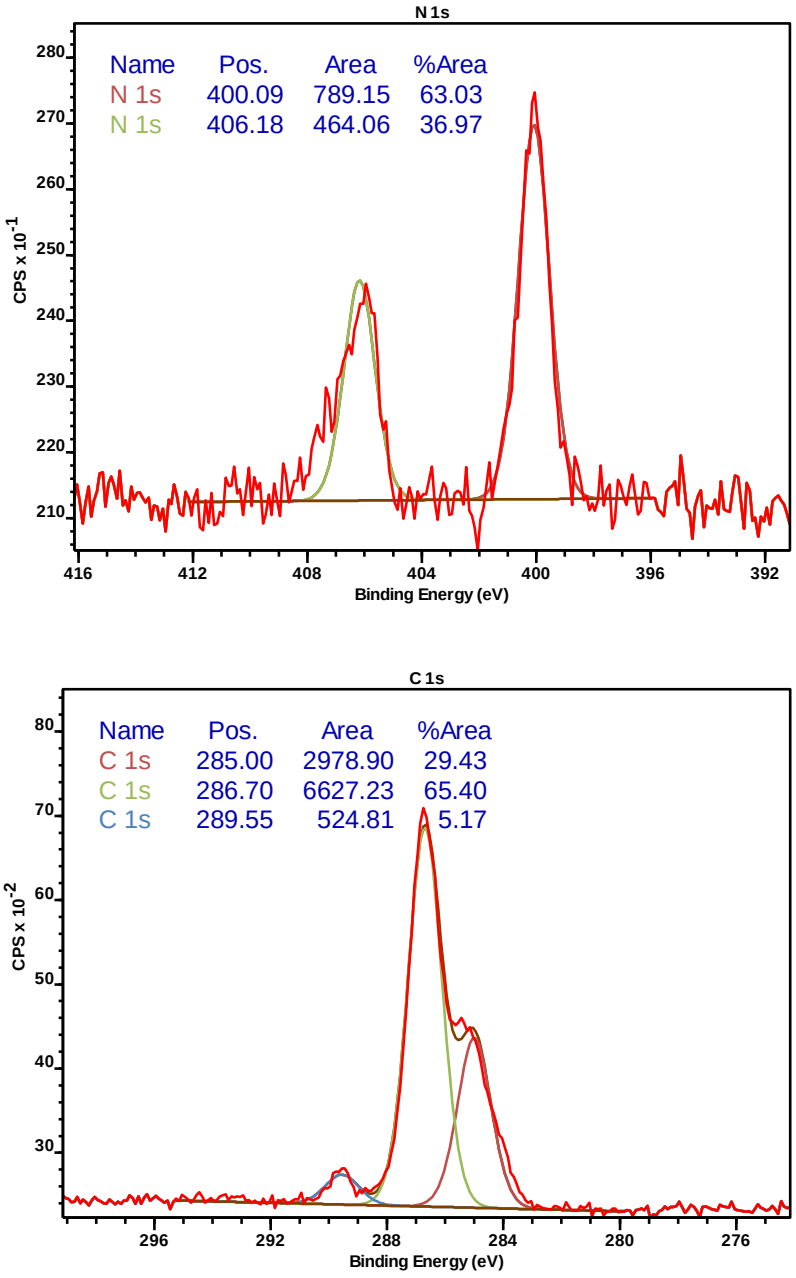

Figure 31. Top, the N 1s photoelectron spectrum and bottom, the C 1s photoelectron spectrum for a native OEG-NPEOC-APTES monolayer on silicon.

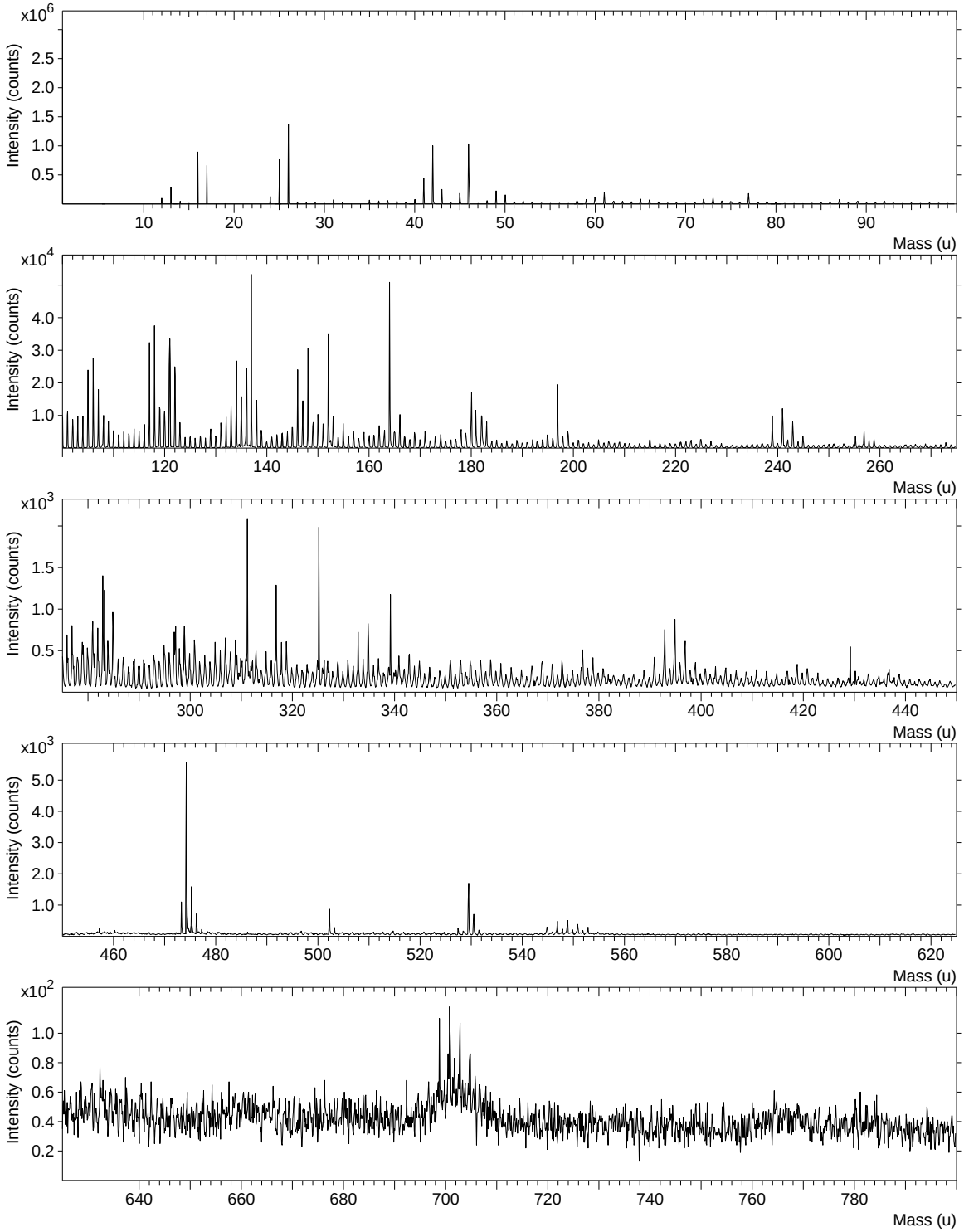

Figure 32. Negative ion SIMS spectra of OEG-NPEOC-APTES on silicon.

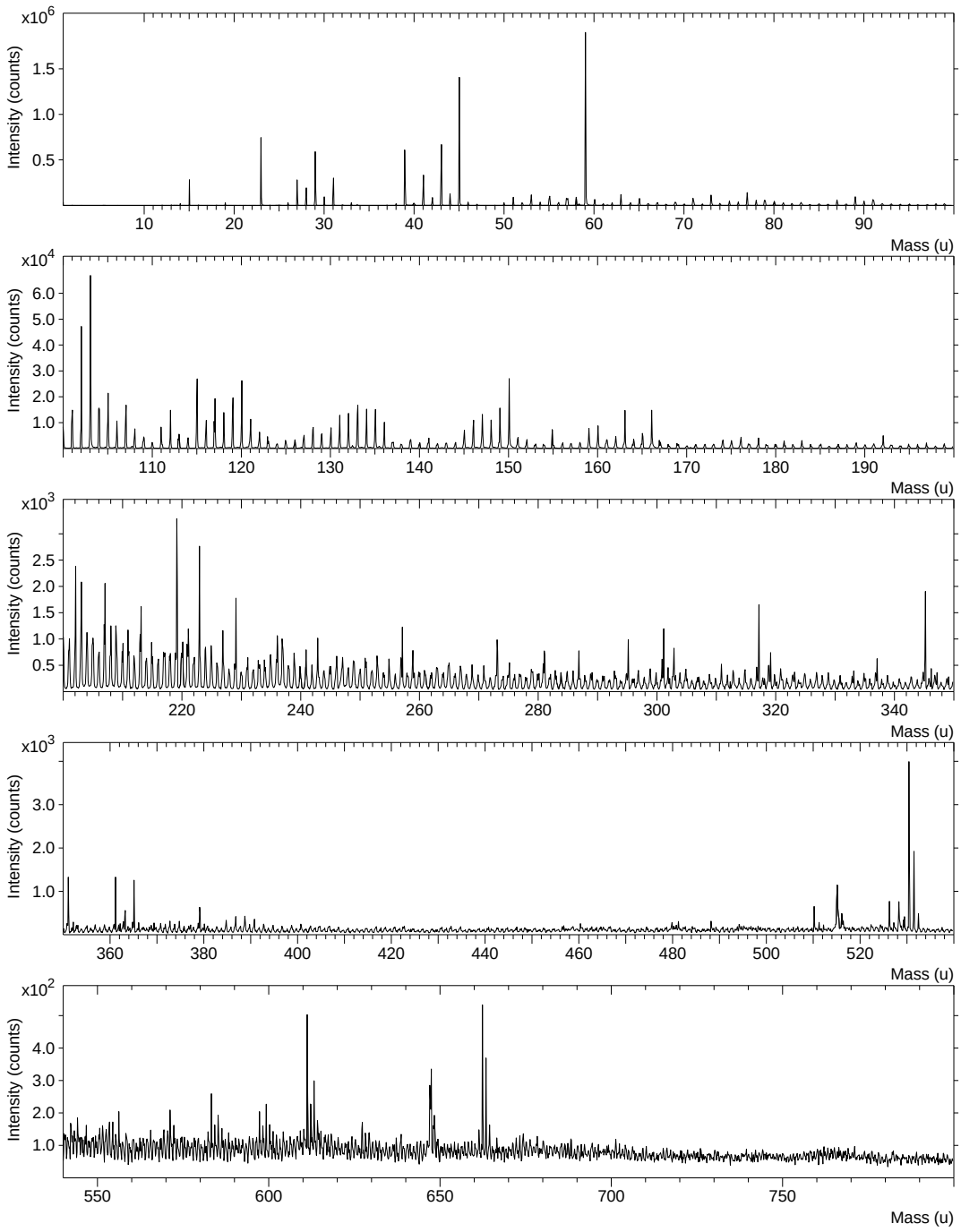

Figure 33. Positive ion SIMS spectra of OEG-NPEOC-APTES on silicon.

4.3.2. Tribochemical modification of OEG-NPEOC-APTES

By applying a load to the surface through an AFM tip and moving the tip across the surface of a film it is possible to modify the surface in such a way that it is visible via the use of AFM imaging. Due to the nature of the modification, a change in topography is visible, as is a change in the frictional force. This is to be expected as a large portion of the molecule is being removed and the chemistry of the functional group at the surface of the molecule between modified and unmodified areas is markedly different enough to show up in FFM.

The image in figure 34 was produced when a load of a 750 nN was applied to the tip and moved across the surface at a constant speed of 10 µm s^{-1}. The line in figure 34 (B) has an average FWHM of 29.17 nm and an average depth of 0.48 nm. Samples needed to be rinsed following tribochemical modification as a phenomenon known as plowing occurs leading to a build-up of debris at the side of the feasture.[199] Figure 35 shows a typical image of sample immediately after modification. The line section in figure 35 (B) is taken from the line in the main image that has the least debris visible and yet a noticeable ploughing effect can be seen. Following a rinse with PBS, any part of the original monolayer that was removed during the lithographic process was subsequently washed away and clean images like those in figure 34 are standard.

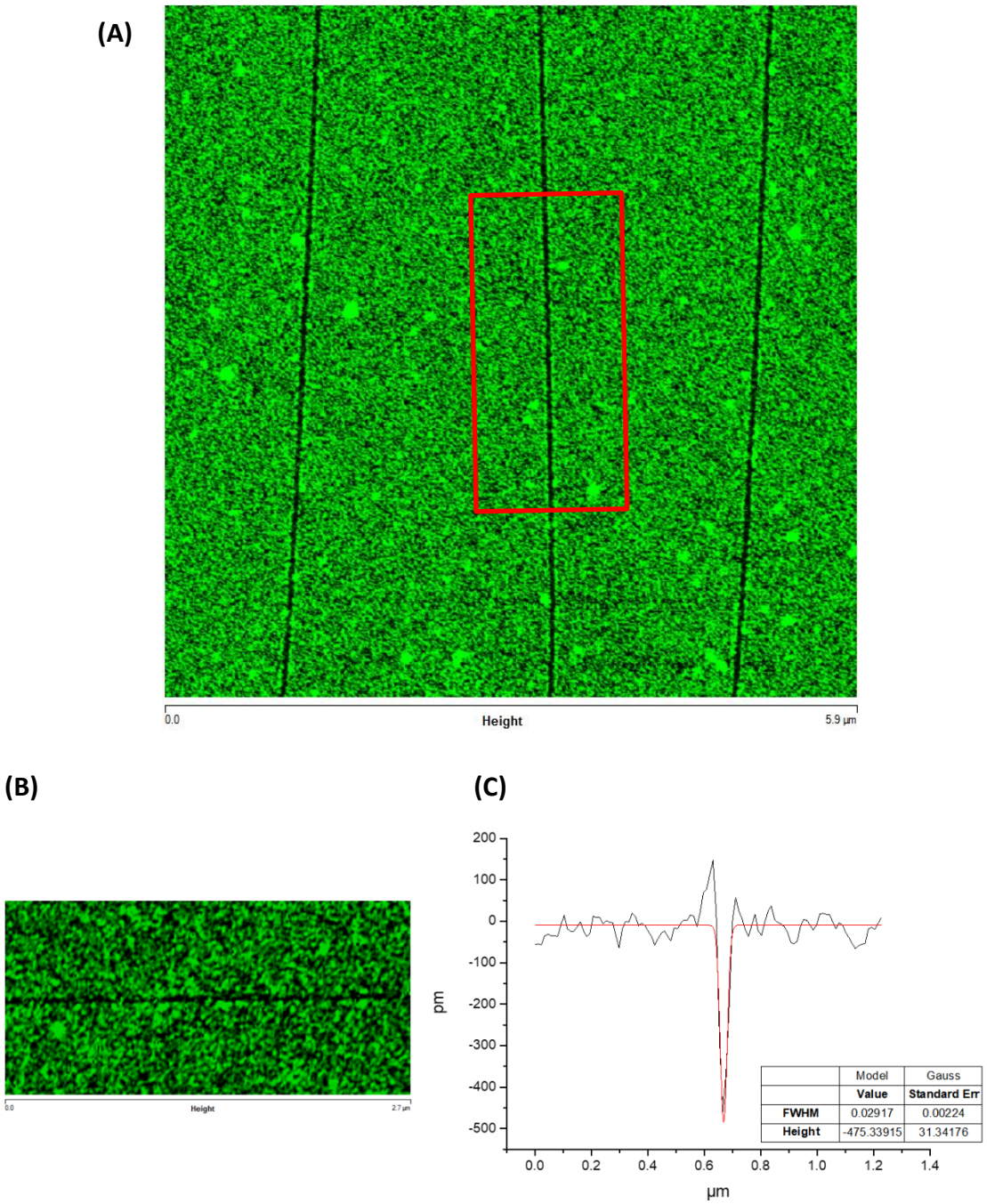

Figure 34. (A) A tapping mode AFM topography image of a tribochemically modified OEG-NPEOC-APTES film. **(B)** A higher magnification image of the section in (A) that is indicated by the red overlay and **(C)** a line profile for the area in (B).

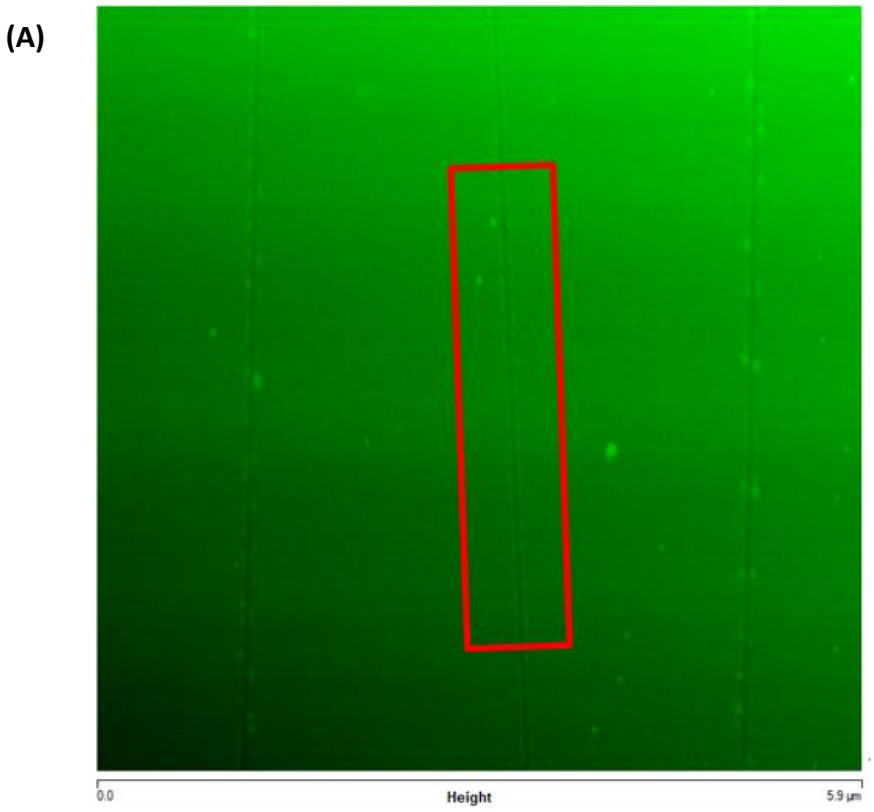

Figure 35. (A) A tapping mode AFM topography image of a tribochemically modified OEG-NPEOC-APTES film showing the build-up of debris following tribochemical modification. **(B)** A line profile for the area in (A) highlighted by the red overlay.

The effect of the load applied to the surface to the feature width and FWHM was investigated. Loads from 300 nN to 10,000 nN were applied. Loads no lower than 300 nN were selected because no detectable modification was observed for such values. In figure 37, data points are not included for lines drawn using loads of 300 and 400 nN, as though they did yield lines of modified OEG-NPEOC-APTES detectable via AFM, there were not enough recorded examples (N>10) to make the results statistically significant. 10,000 nN was chosen as the upper limit as a control was carried out on an APTES film to see what load is required to fully cleave the silane from the substrate. Tests showed that noticeable changes to the APTES surface first occurred when loads of in the region of 10,000 nN was applied. Though loads nearing 15,000-20,000 nN were required to remove the APTES fully, loads of 10,000 nN and lower were used in this study to increase confidence that any changes to the OEG-NPEOC-APTES surface that were seen were due to the protecting group being cleaved, as in figure 30, and not due to molecule being removed from the surface in its entirety.

When larger loads are used, the increase in FWHM is noticeably larger, and though harder to spot without using software to analyse the AFM image, the depth of the feature size increases also. The image in figure 36 was produced when a load of a 5,000 nN was applied to the tip and moved across the surface at a constant speed of 10 µm s^{-1}. The line in figure 36 (B) has an average FWHM of 60.68 nm and an average depth of 0.78 nm. Figure 37 shows the relationship between applied load and feature FWHM and the applied load and feature depth. For these load experiments the AFM tip was brought into contact with the surface and performed 16 scans across a 60 x 60 μm^2 area at a constant speed of 10 µm s^{-1}. Multiple lines from each experiment were analysed and each experiment was repeated a number of times (N>5). It can be seen that an increase in FWHM and depth occurs. This would suggest that there is not an immediate change from an intact molecule to a cleaved molecule, but rather that varying degrees of partial deprotection occur, increasing with load.

This would seem to align with photodeprotection studies that indicate that a threshold dosage of UV light is required for complete deprotection and partial deprotection occurs up to the point where the threshold dosage is met.[188] Rather than this gradual change to FWHM and depth occurring from a point of zero load, a minimum threshold for any deprotection needs to be met. This can be explained by presuming that below a certain pressure, the tip only acts to sit upon the surface and when a high enough load is applied, the tip breaks through the surface.[200]

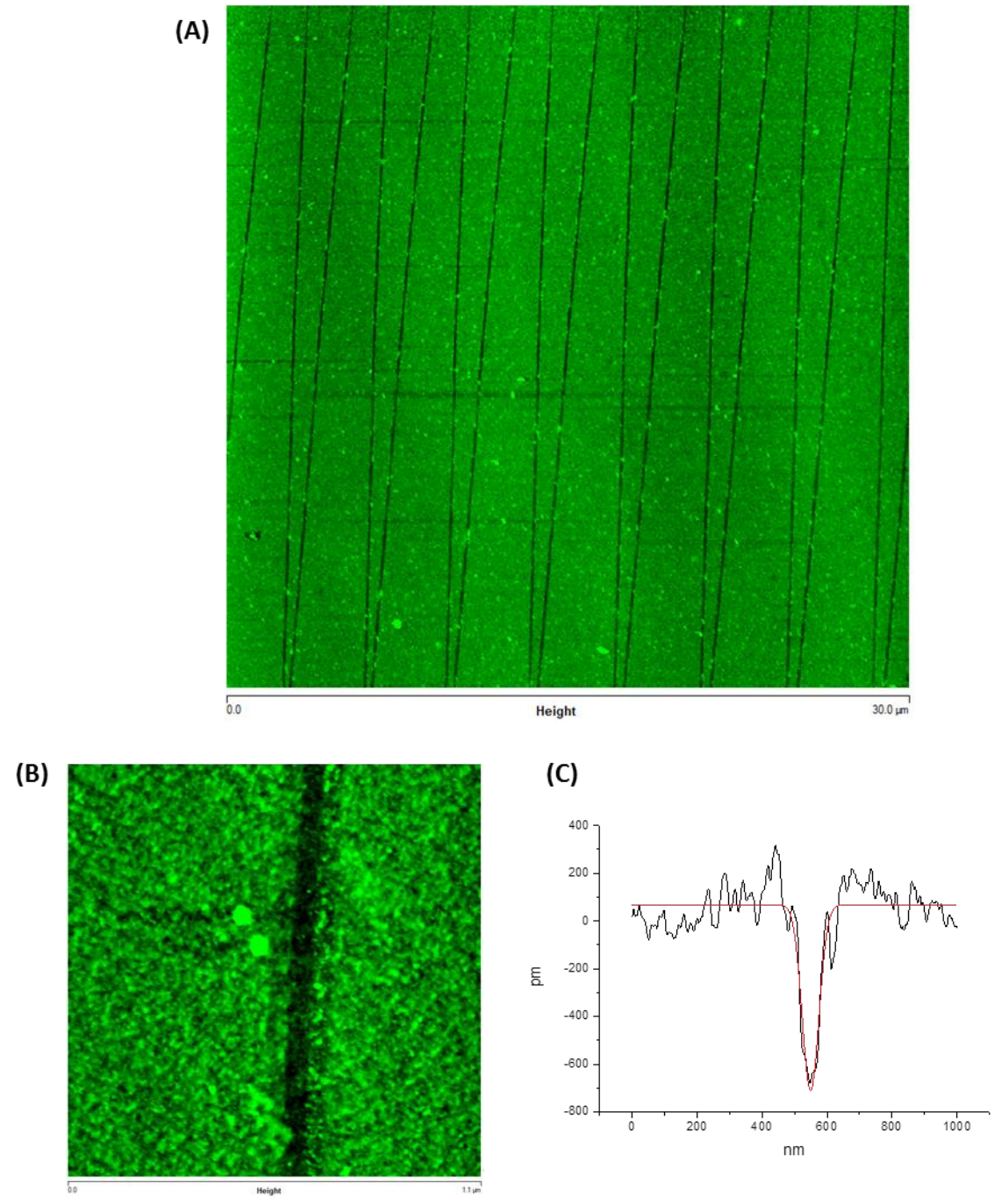

Figure 36. (A) A tapping mode AFM topography image of a tribochemically modified OEG-NPEOC-APTES film. **(B)** A higher magnification image and **(C)** a line profile for the area in (B).

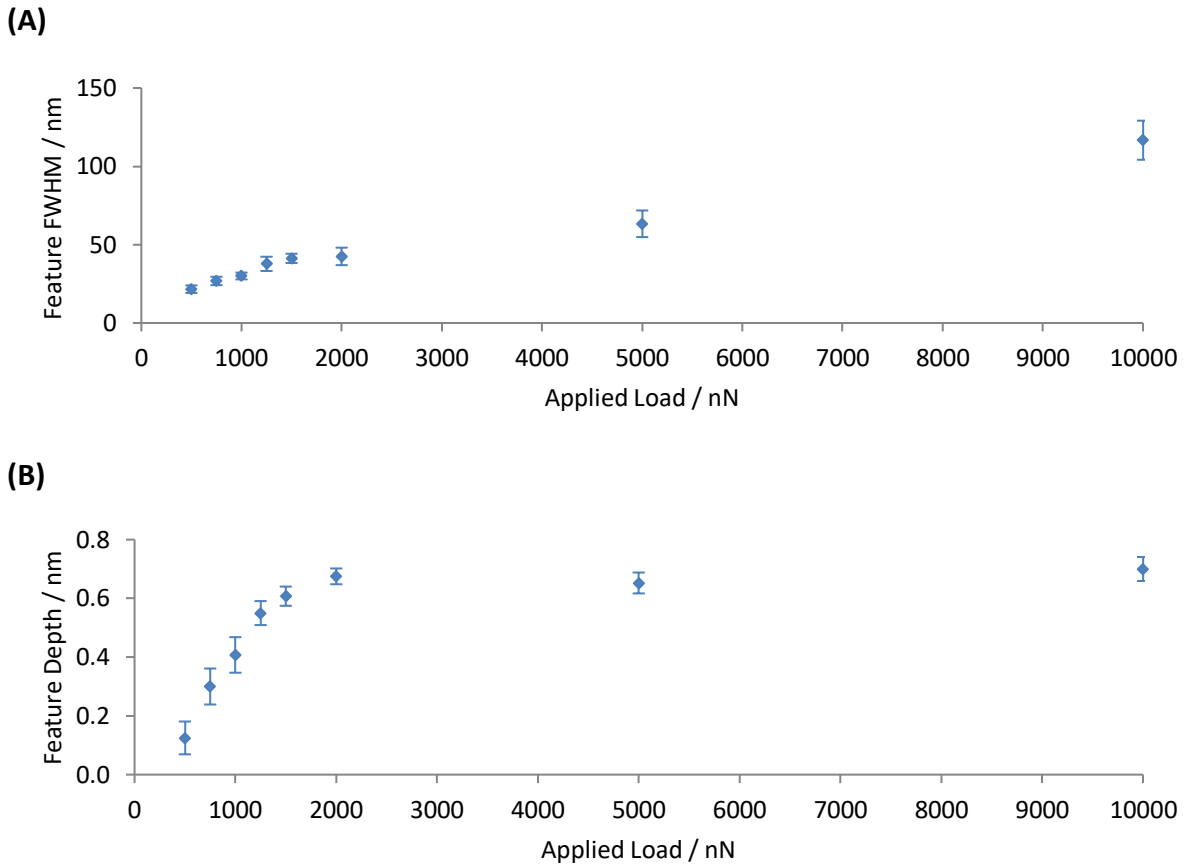

Figure 37. A graph showing the effects of load applied to an AFM tip vs. **(A)** feature FWHM, and **(B)** feature depth, of tribochemically modified OEG-NPEOC-APTES.

As in chapter 3, writing speed was also investigated. For these writing speed experiments, the AFM tip was brought into contact with the surface and performed 16 scans across a 60 x 60 μm^2 area at a constant load of 750 nN. Multiple lines from each experiment were analysed and each experiment was repeated a number of times (N>5). Four writing speeds were chosen such that they covered a number of orders of magnitude but remained within the physical constraints of the AFM. From the graph in figure 38 it is apparent that the effect of writing speed on feature properties is significantly less than that of the effect of the

applied load. The faster writing speeds had more statistical variance, possibly as result of the feedback loop in the AFM not being able to track the surface as accurately. Conversely, slower writing speeds had less statistical variance. However, the slowest writing speeds were impracticably slow and as such are not worth the compromise of slightly smaller feature sizes.

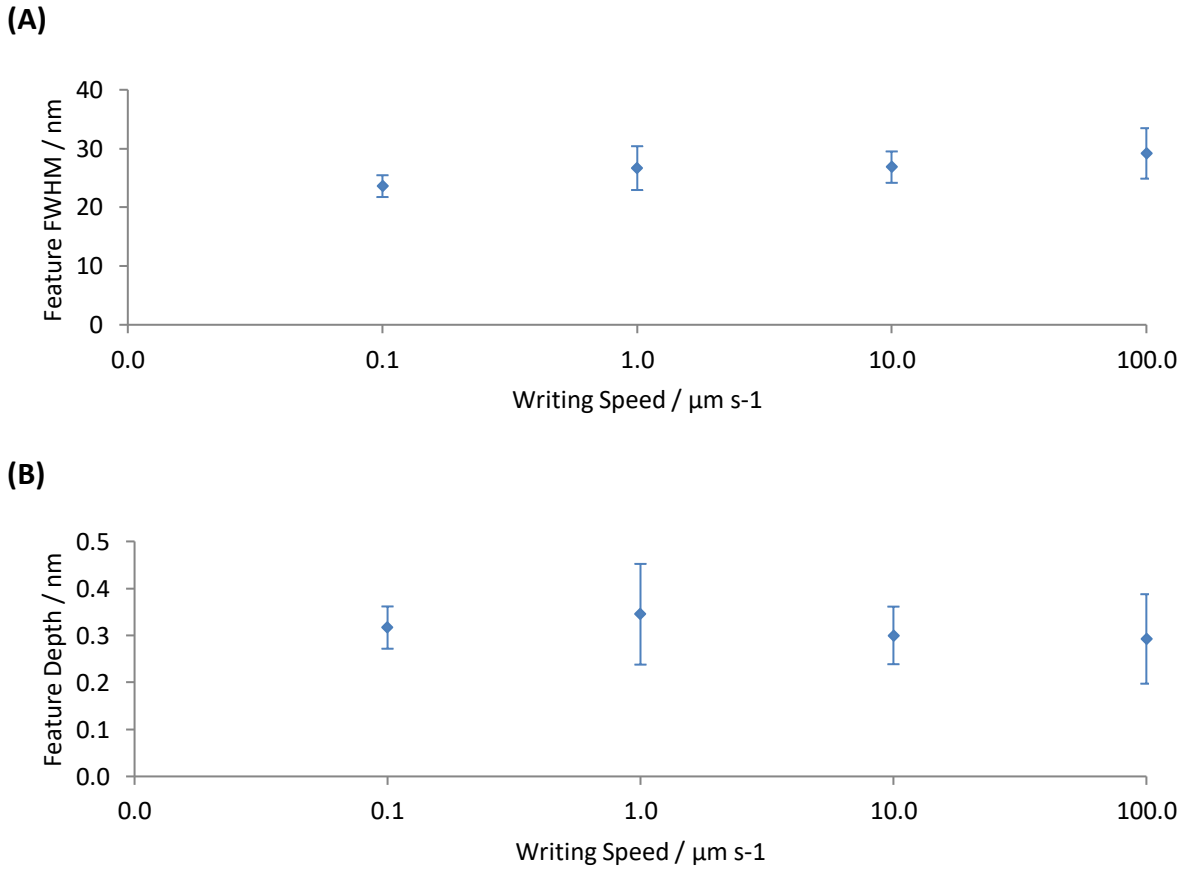

Figure 38. A graph showing the effects of the writing speed of an AFM tip vs. **(A)** feature FWHM, and **(B)** feature depth, of tribochemically modified OEG-NPEOC-APTES.

4.3.3. Attachment of GFP to tribochemically modified OEG-NPEOC-APTES

Proteins can be attached to modified OEG-NPEOC-APTES via a series of steps. These reactions only occur at the modified regions of OEG-NPEOC-APTES as the unmodified monolayer retains its natural antifouling and is relatively inert. One such method first involves generating an aldehyde functionalised surface, which can be done by reacting the free amine with glutaraldehyde. An NTA surface was then generated by reacting ABNTA with the surface. The NTA functional group is a well-known chelating group that can bind strongly to Ni in such a way that a His-tagged protein can then subsequently bind to the Ni.[201] This process provides a complete chemical link from OEG-NPEOC-APTES to GFP and is shown schematically in figure 39.

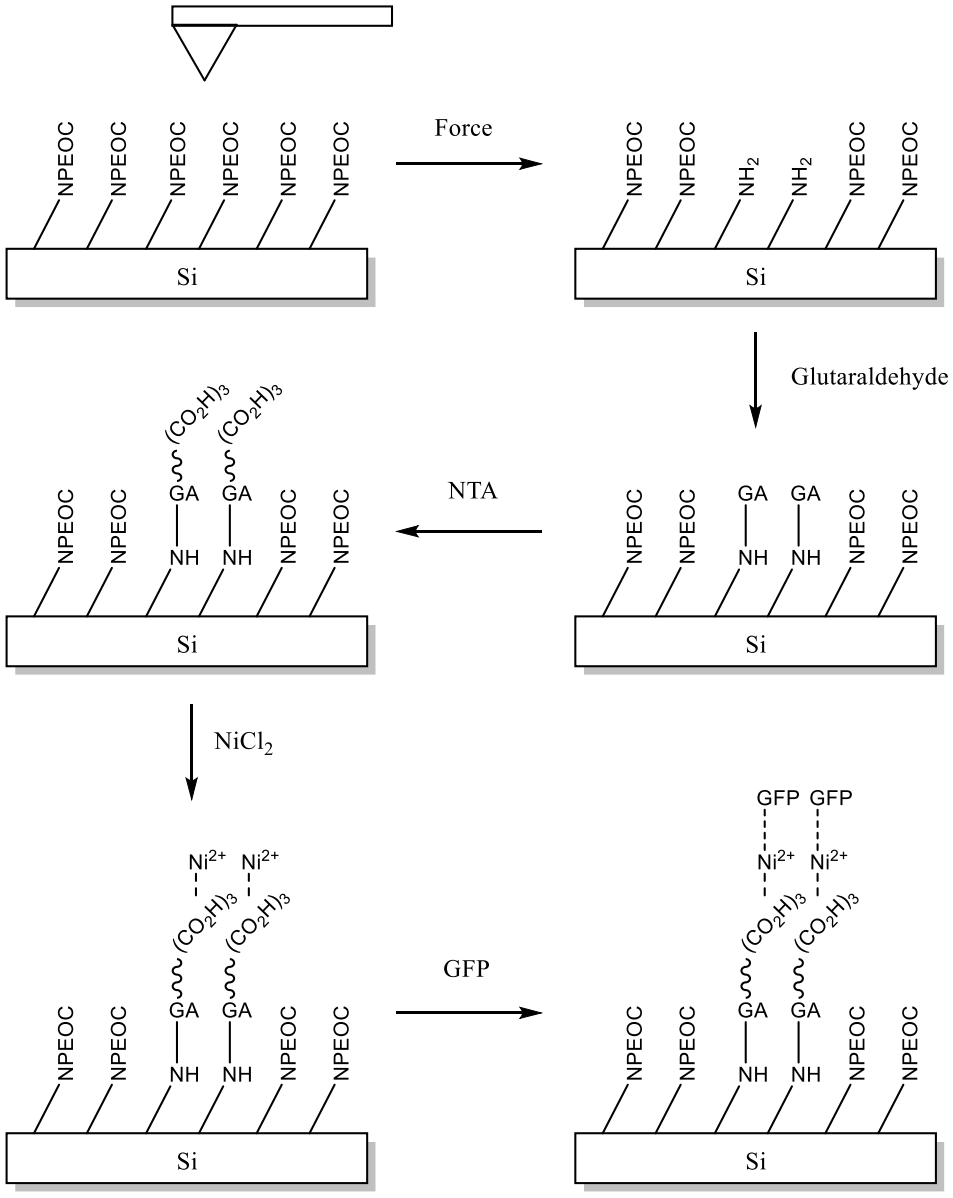

Figure 39. A schematic showing the derivatisation involved in the attachment of GFP to tribochemically modified regions of OEG-NPEOC-APTES.

An extra step must be taken in order to enable any lines drawn in the OEG-NPEOC-APTES monolayer to be visualised using a confocal microscope. Metal was evaporated through a finder grid in order to create easily identifiable structures on the macroscale. The

process works as follows: gold is evaporated through a finder grid which is pressed against the silicon/glass slides resulting in areas of gold and clean glass. Following this stage, a dodecanethiol monolayer is put down. Thiols are known to bind strongly to gold, but will not adsorb onto silicon/glass, resulting in a patterned slide of dodecanethiol and clean glass. This sample is then immersed in OEG-NPEOC-APTES, which will adsorb onto the silicon/glass, but will not displace the thiol layer from the gold. The OEG-NPEOC-APTES areas can then scratched as outline above, a schematic for which is found in figure 41.

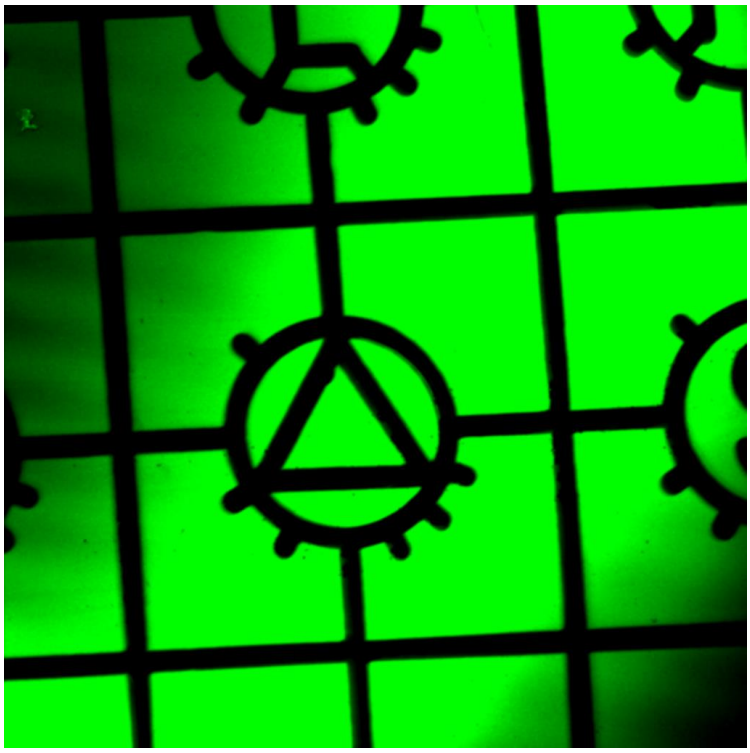

Figure 40. A fluorescence image of a finder grid pattern fabricated using the method in figure 41. The dark areas were covered by the finder grid during the evaporation step and so are protein resistant OEG-NPEOC-APTES whereas the green areas are fluorescing GFP adsorbed onto dodecanethiol which is in turn bound to a gold layer on the substrate.

When the sample is tribochemically modified and subjected to the GFP attachment steps outlined in figure 39 and figure 41, the unmodified OEG-NPEOC-APTES will resist the adsorption of GFP, the modified regions of OEG-NPEOC-APTES will bind to GFP, and the dodecanethiol regions will non-specifically adsorb GFP. An example of such a surface is given in figure 40. There is good contrast between the black and green areas of the image, indicating that the protein resistant properties of OEG-NPEOC-APTES have not been compromised by the additional steps and modifications to the substrate surface.

However, upon inspection of a higher resolution image of the area of interest where scratching was carried out was taken, no evidence of a scratching pattern was visible. A possible reason for this could be that due the presence of large amounts fluorescing molecules on the surface, a signal of a fluorescing line which is only 10s of nanometres wide could be effectively drowned out and not detected, though this is unlikely as fluorescence images have been captured at this scale before. It is also possible that the steps leading up the attachment of GFP had failed. If this were the case, then GFP would still be able to freely adsorb to the dodecanethiol but would not specifically bind to the modified OEG-NPEOC-APTES as desired.

A control experiment was designed such that the GFP attachment steps were carried out on an unmodified APTES surface. APTES was chosen as it is identical to the proposed product of tribochemical modification of OEG-NPEOC-APTES. Fluorescence microscopy showed complete surface coverage of GFP and its subsequent removal using imidazole, a well-known competitive inhibitor of His-tagged proteins.[202] This suggests that the attachment process was not the problem, though not ruling it out entirely as the reaction with native APTES was occurring on the macro scale without any spatial or steric confinement issues.

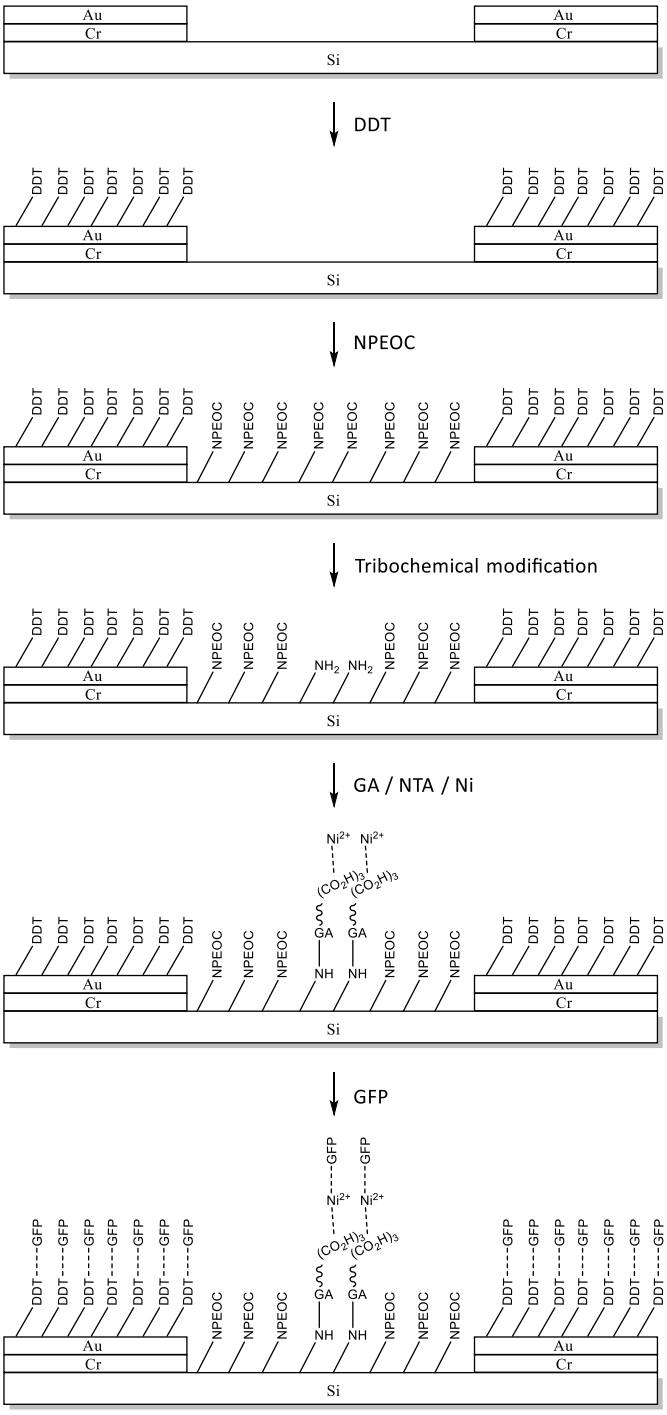

Figure 41. A schematic showing a dodecanethiol protecting layer in order to create areas of fluorescent contrast to identify regions of interest under a confocal microscope.

4.3.4. Growth of PCysMA from tribochemically modified OEG-NPEOC-APTES

Growing polymer brushes from tribochemically modified OEG-NPEOC-APTES surfaces was investigated. A control was designed to grow PCysMA from APTES monolayers on silicon, as APTES is significantly cheaper than OEG-NPEOC-APTES and as for the attachment of GFP control experiment above, APTES is the expected product of the modification process and therefore is a comparable starting point for the polymerisation process. Growth of PCysMA through ARGET-ATRP is a fast process with polymer growth being apparent after only 30 seconds immersion time, however, the degree of polymerisation is not controlled when compared to other polymerisation techniques leading to discrepancies between repeat measurements and large statistical variances in the growth profile displayed in figure 42. It is apparent from the growth profile that the rate polymerisation appears to tail off after 40 mins and from observation, the polymerisation solution for the conditions we used was no longer active after 2 hours.

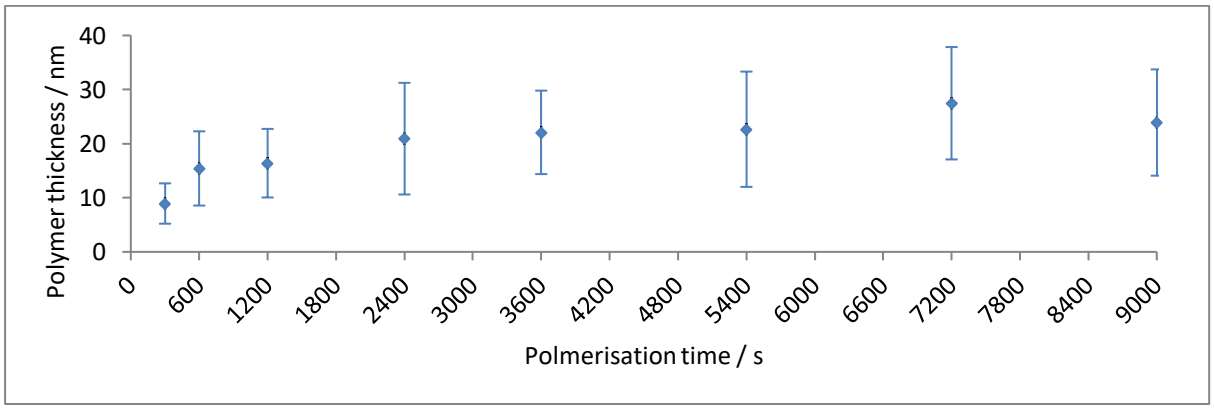

Figure 42. A growth profile for PCysMA on silicon. Thicknesses were measured using an ellipsometer.

When PCysMA was grown from tribochemically modified OEG-NPEOC-APTES the polymer was not contained to the modified regions, but instead was apparent all over the surface. This is shown in figure 43, which is the same sample as figure 34 after it has been reacted with an initiator and then immersed in PCysMA solution. The well defined lines that were generated after the lithography stages are no longer visible and instead the surface appears to be much rougher, suggesting complete coverage of polymer rather than polymer growth in the desired areas only. Possible reasons for this are adsorption of polymer to native the native OEG-NPEOC-APTES film or initiator binding to unmodified regions.

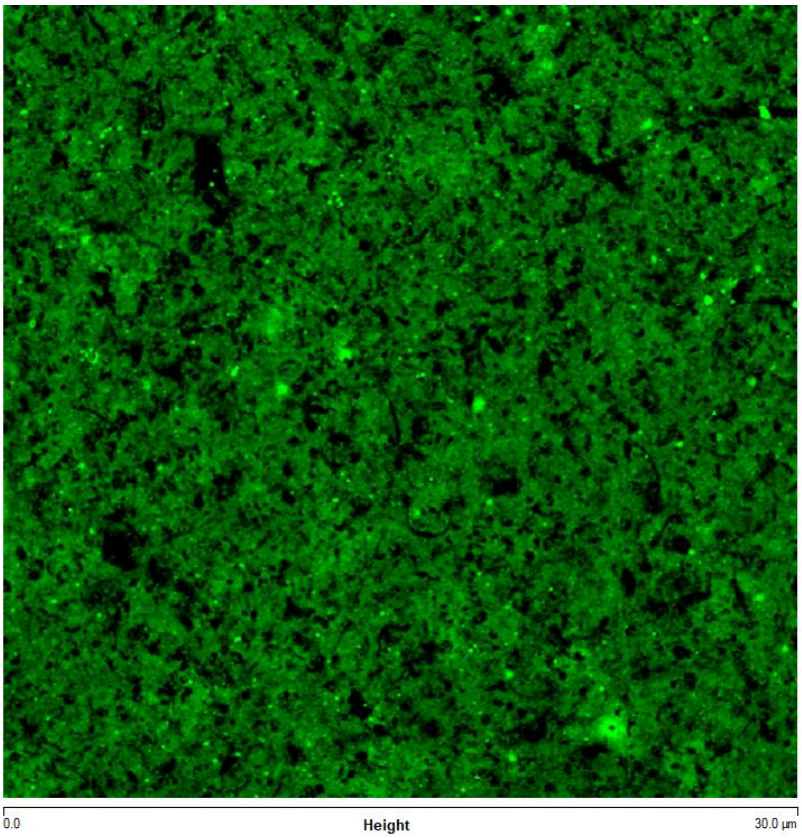

Figure 43. An AFM tapping mode topography image of a tribochemically modified OEG-NPEOC-APTES surface after being immersed in polymerisation solution.

To examine these possible causes of uncontrolled polymerisation, OEG-NPEOC-APTES films were exposed to UV light (λ=244 nm) and reacted with initiator and then reacted with polymer and each step monitored.

First OEG-NPEOC-APTES was exposed to a range of dosages of UV light and its deprotection was monitored by XPS and SIMS. In figure 44, the largest contribution of the C1s spectra of the native film is the peak that corresponds to the carbons in the OEG units (~286.7 eV) but as the molecule becomes further deprotected and the OEG units are removed, the contribution from the aromatic and propyl carbons becomes greater. Figure 45 shows how the nitro group peak (~406 eV) decreases as the amount of photodeprotection increases, to the point that the amine group peak (~400 eV) is the only contribution. Figure 46 shows the nitro group being removed after an 8 J cm^{-2} dose, as the peak at m/z 46 that correlates to the NO_2^- ion fragment can be seen to be almost entirely removed.

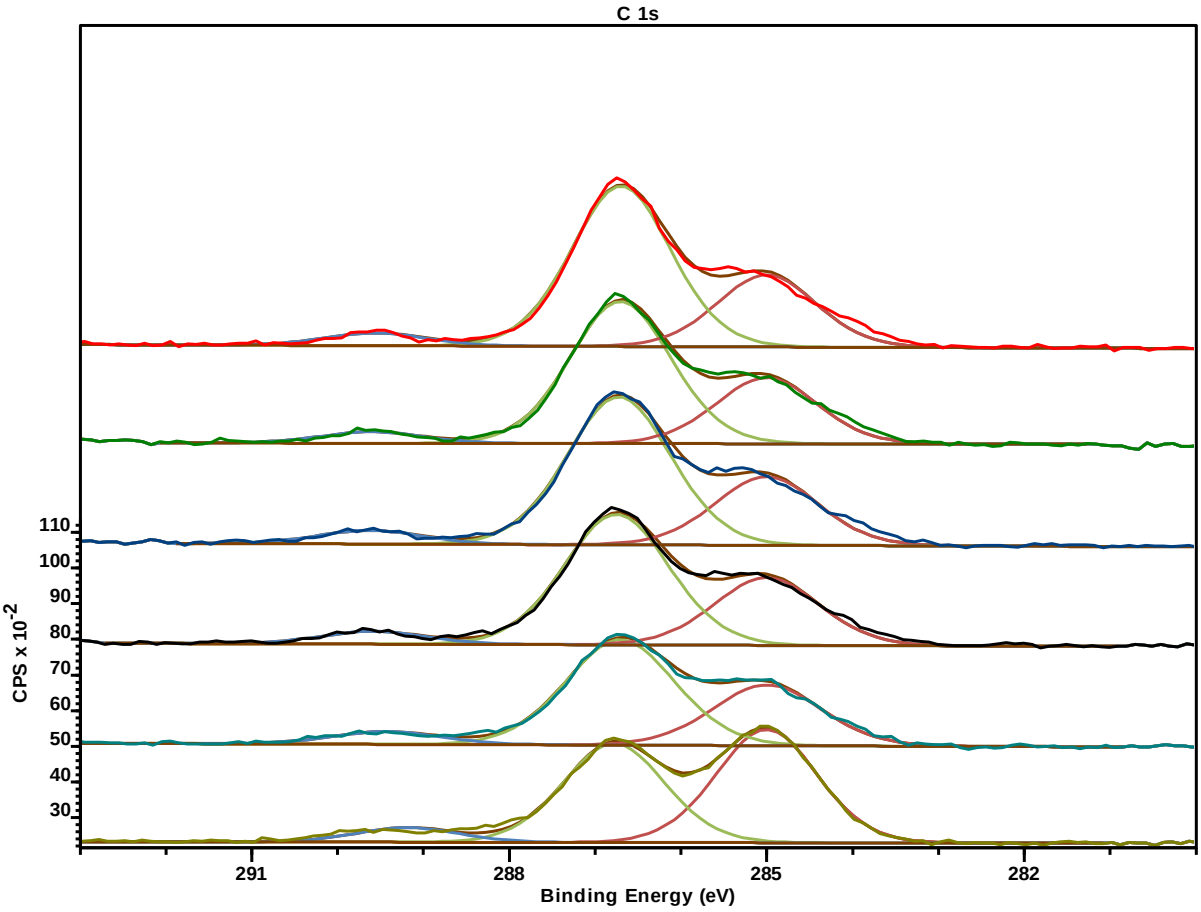

Figure 44. The C 1s spectra for OEG-NPEOC-APTES. The red line shows the native film and the lines below (reading down from the top line) correspond to an OEG-NPEOC-APTES film that has been exposed to dosages of 0.5, 1, 2, 4, 8 J cm^{-2}.

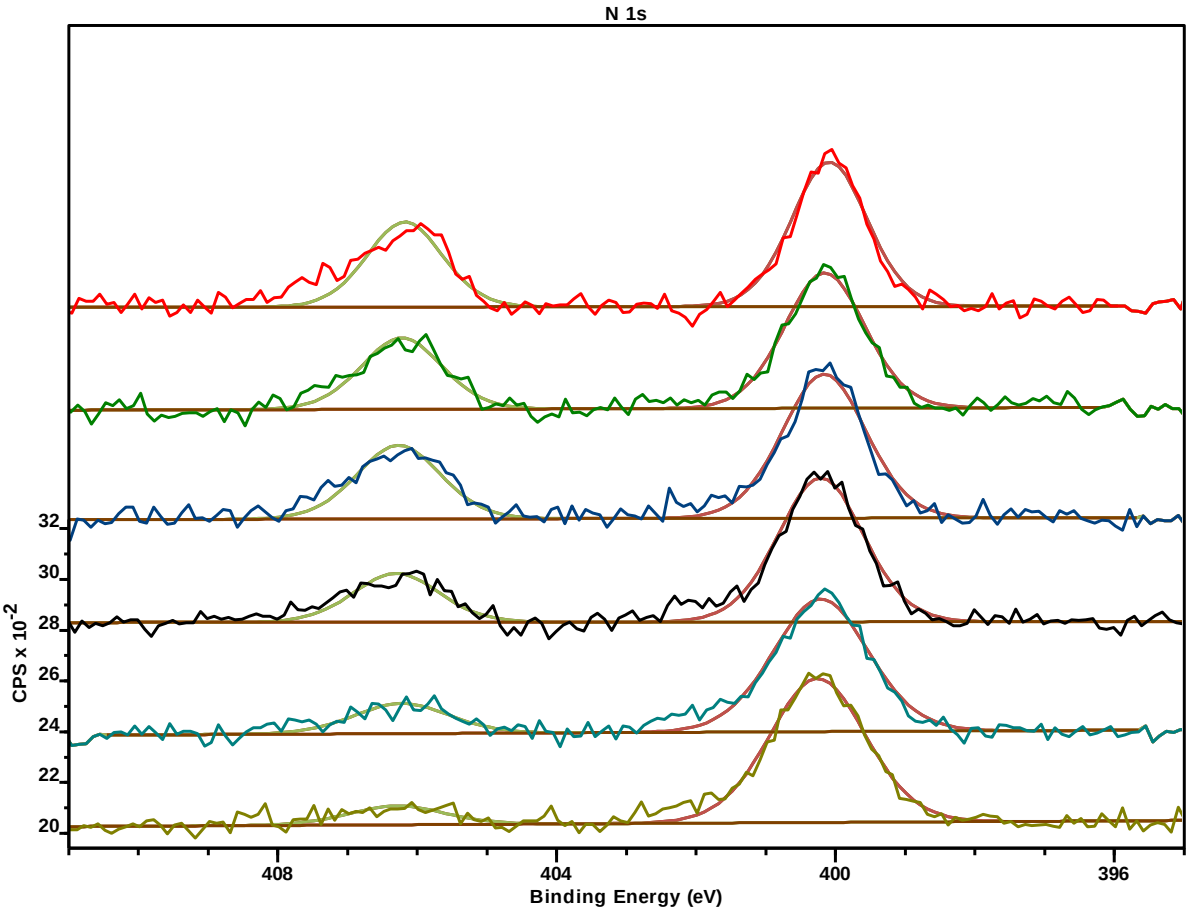

Figure 45. The N 1s spectra for OEG-NPEOC-APTES. The red line shows the native film and the lines below (reading down from the top line) correspond to an OEG-NPEOC-APTES film that has been exposed to dosages of 0.5, 1, 2, 4, 8 J cm^{-2}.

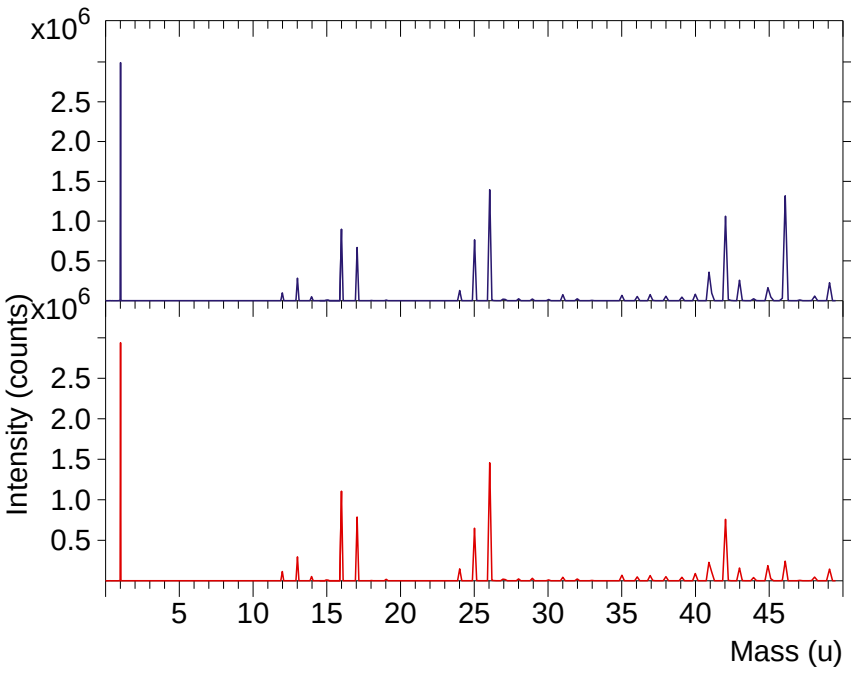

Figure 46. The negative ion SIMS spectra for m/z range 0-50 for **(top)** a native OEG-NPEOC-APTES film and **(bottom)** an OEG-NPEOC-APTES film that has been exposed to 8 J cm^{-2}.

Photodeprotection of OEG-NPEOC-APTES was done through a mask and then the sample immersed in initiator. The resultant surface was examined by SIMS imaging, see figure 47, which shows good contrast between regions where nitro groups are present, i.e. covered by the mask during the photodeprotection stage, and regions where the nitro groups have been exposed to UV light. These exposed areas show a high uptake of bromine which is responsible for initiating the polymerisation reaction, as a result of BiBB reacting with the free amine product of photodeprotection. The contrast however is not as clear as for the nitro groups, suggesting that bromine is present in undesired regions of the surface. This is further supported by SIMS analysis of the same sample after polymerisation. m/z peaks containing

sulfur groups were examined, as sulfur is unique to CysMA monomer units in these reaction conditions, and they were found to be present across the entire surface.

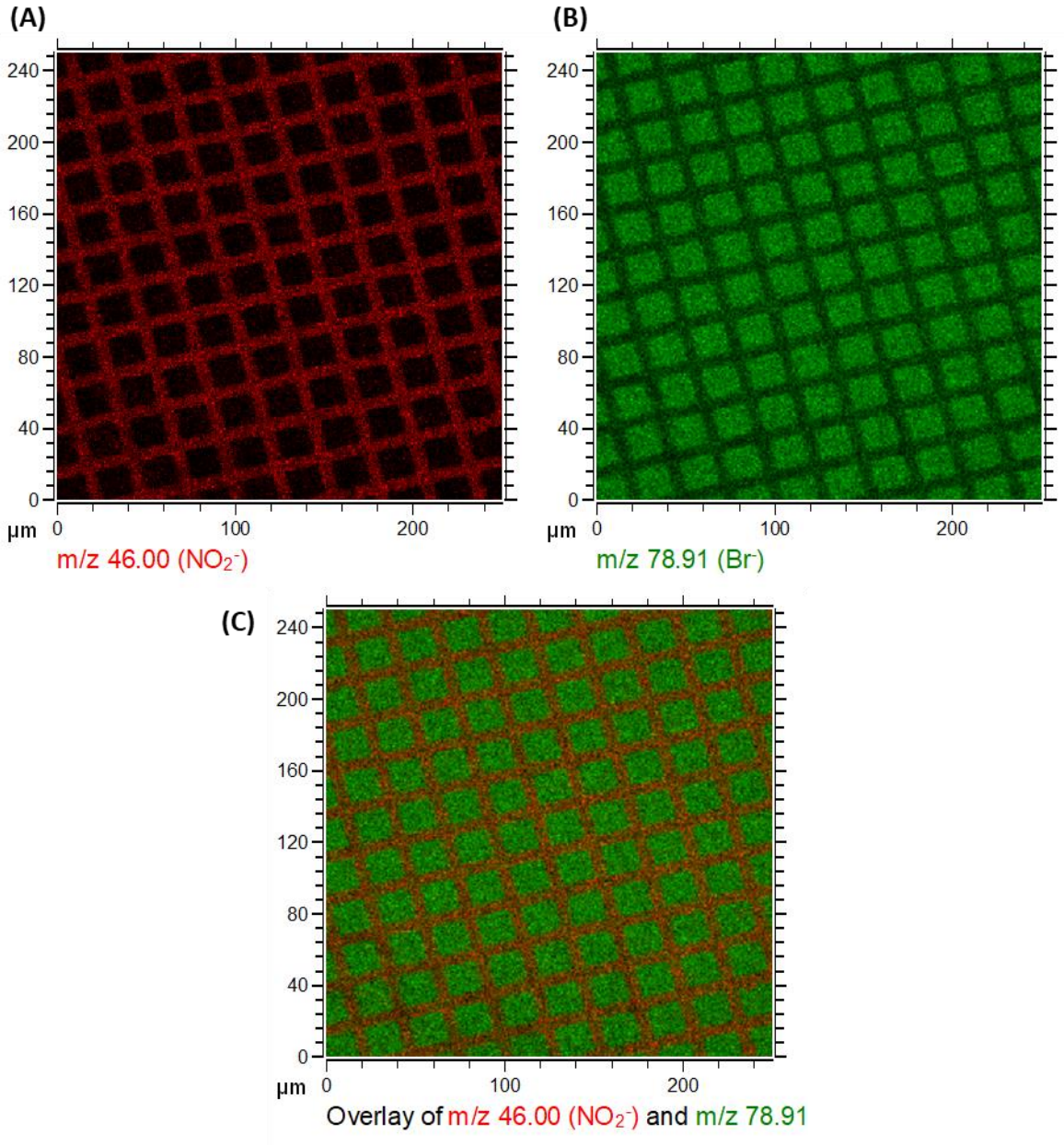

Figure 47. Negative ion images of an OEG-NPEOC-APTES film photodeprotected through a mask. Ion density image for **(A)** m/z 46.00, **(B)** m/z 78.91 and **(C)** the overlay of the contributions of both m/z 46.00 and 78.91.

Samples were imaged via AFM and showed evidence of selective polymer growth in the area that were exposed to UV light, contrary to that evidenced by SIMS. However, upon inspection the height difference between the exposed and protected areas did not match up with the thickness expected from ellipsometry studies. The height of the polymer growth appeared markedly smaller than the expected thickness, an example of which is shown in figure 48. This sample was immersed in polymer solution for 10 mins, though the difference between the height of the squares and the lower areas in between was approximately only 4.5 nm. This is a much smaller height than expected according to figure 42.

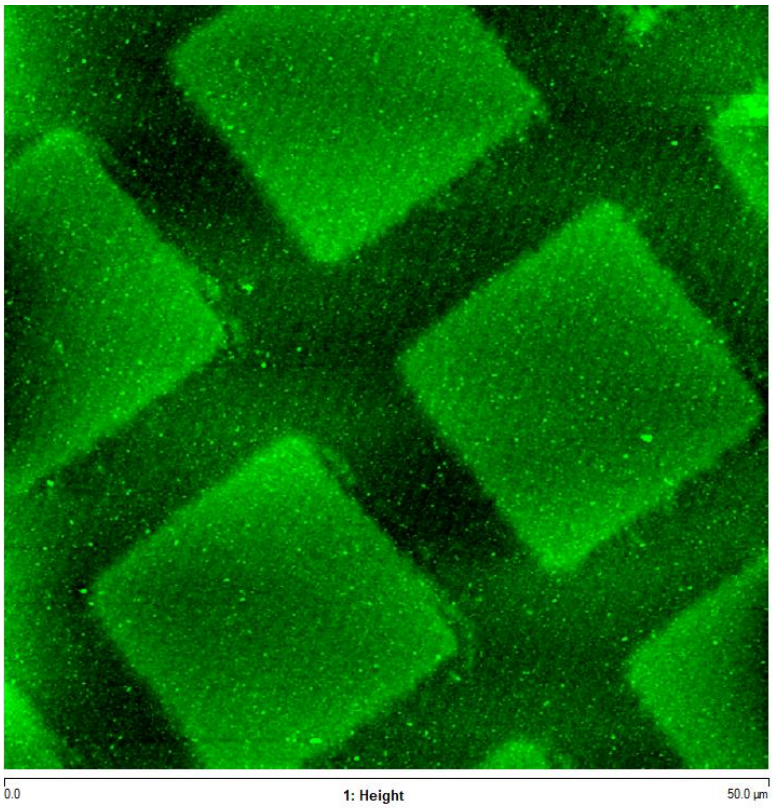

Figure 48. A tapping mode topography AFM image of an OEG-NPEOC-APTES film photodeprotected through a mask. The sample was then exposed to PCysMA solution.

This would evidence that bromine is taken up by the surface in the unexposed areas, though less densely than at the exposed areas. Due to the catalytic nature of the polymerisation process, only small amounts of bromine need to be available at the surface in order to start the growth of a long polymer chain. XPS studies show this to be the case as evidenced in figure 49. The fully deprotected OEG-NPEOC-APTES shows a large increase in the bromine 3d peak, whilst the OEG-NPEOC-APTES that has not been exposed to any UV light shows a small peak. This would explain why polymer covers the entirety of a photopatterned surface and why the difference in polymer density is different between the exposed and protected areas.

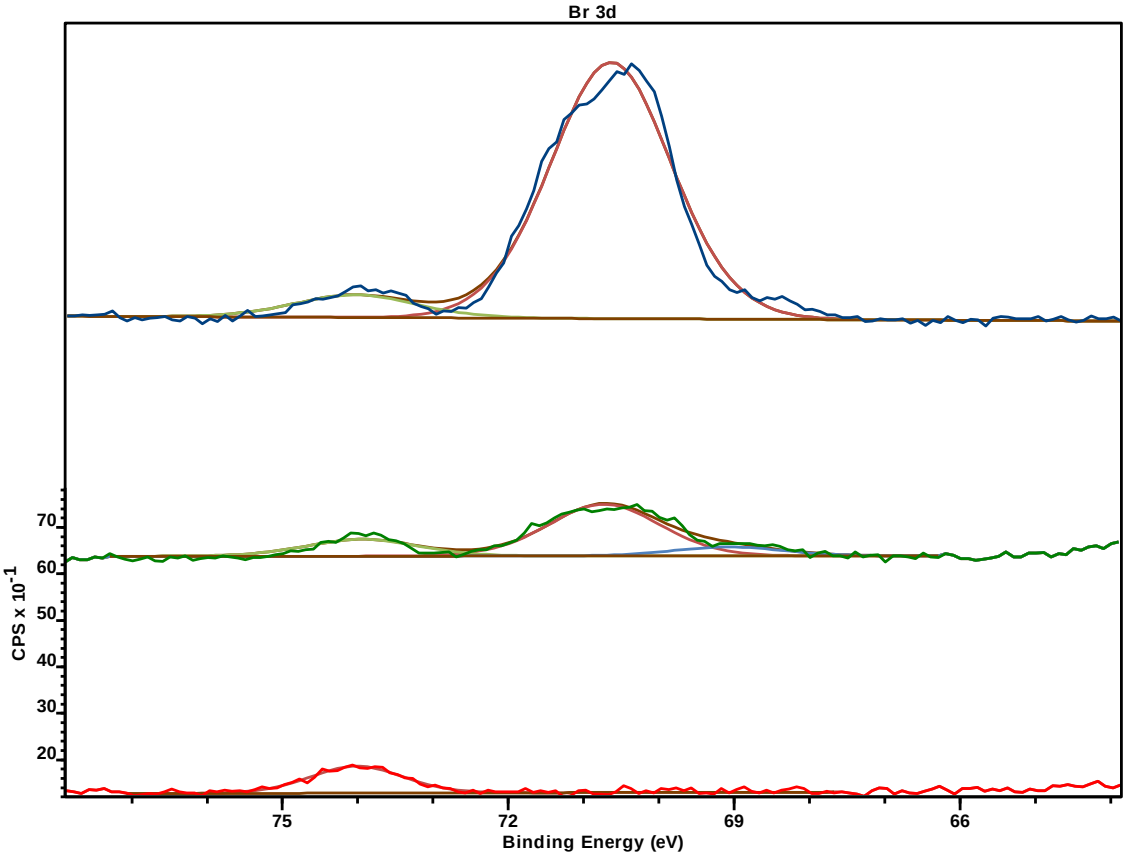

Figure 49. The Br 3d spectra of **(top)** an OEG-NPEOC-APTES film that has been exposed to a dose of 16 J cm^{-2} then reacted with BiBB, **(middle)** an OEG-NPEOC-APTES film that has been reacted with BiBB and **(bottom)** an native OEG-NPEOC-APTES surface.

It is most likely that a side reaction is occurring between the carbamate group of OEG-NPEOC-APTES and the initiator molecule outlined in figure 50. Though normally a poor nucleophile, the nitrogen in the carbamate can act as one when exposed to BiBB. This is because the acyl bromide is a very good leaving group. Alternative initiator molecules have been proposed that have poorer leaving groups such that the carbamate can not act as a nucleophile upon them, but the amine as a result of OEG-NPEOC-APTES deprotection can.

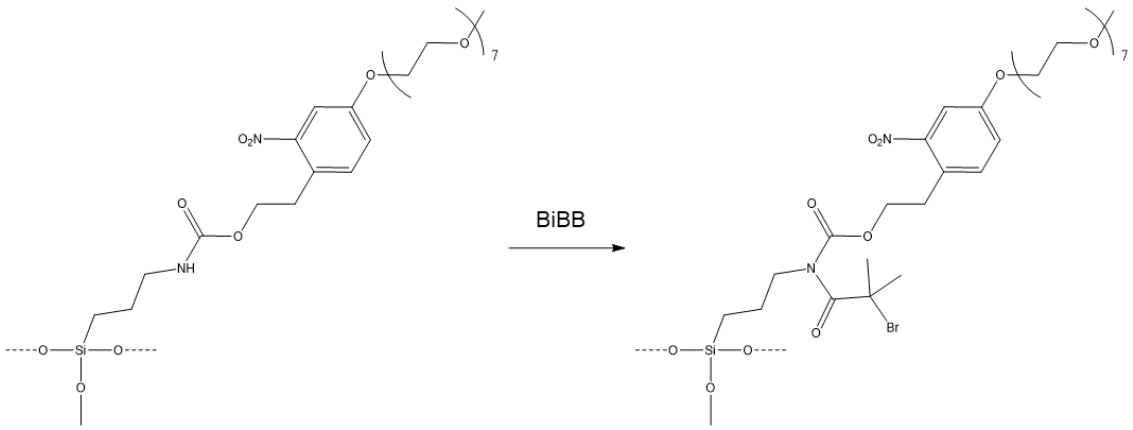

Figure 50. A proposed reaction that accounts for the presence of bromine initiator in unmodified regions of OEG-NPEOC-APTES.

Such alternative molecules are BiBNHS and BiBAn. Investigation of the reactivity of these molecules and their propensity for acting as an ATRP initiator have yet to be fully explored however initial experiments suggest that polymer growth is not as fast when BiBNHS and BiBAn are used compared to BiBB. A control was set up such that the same concentration of each of the three initiator molecules were exposed to an APTES surface. XPS was carried out to examine the amount of bromine present. Figure 51 shows clearly that the amount of bromine present on the surface is much greater for BiBB than BiBNHS and

BiBAn. This would provide a possible explanation for why not as much polymer growth is observed when the latter two initiator molecules are used, though further study is required.

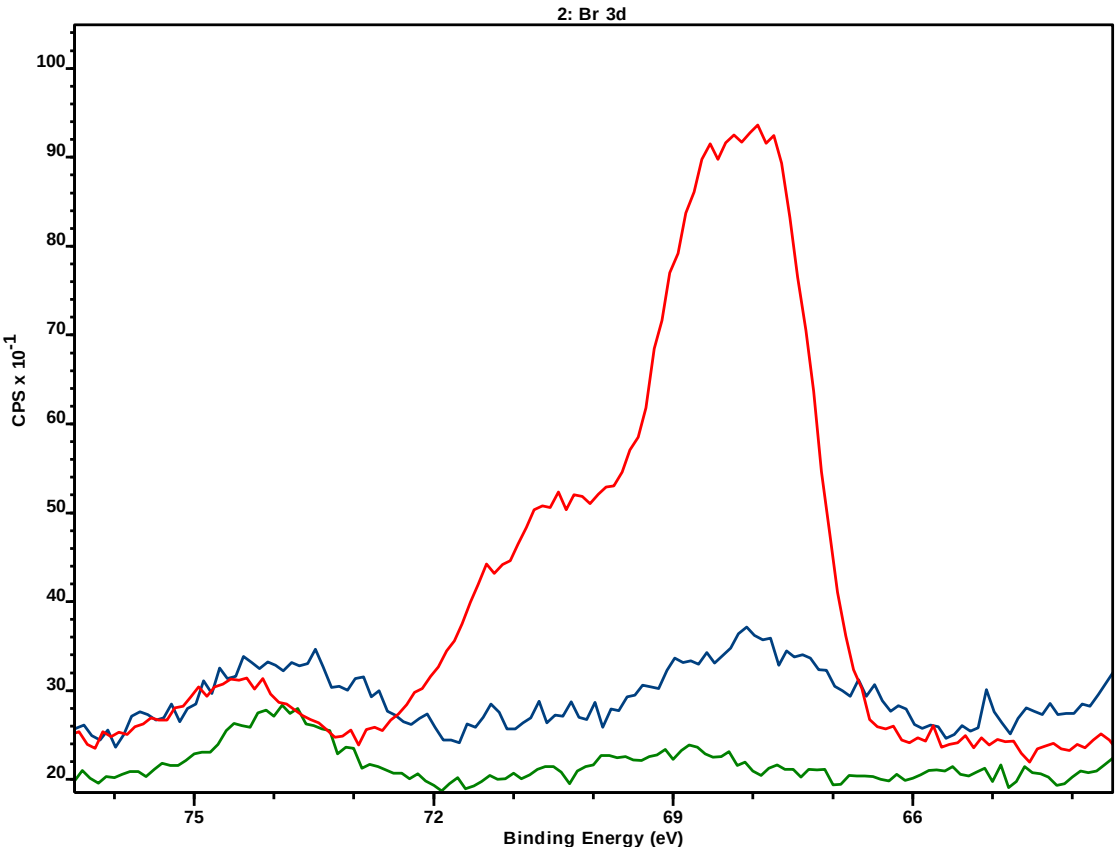

Figure 51. The Br 3d XPS spectra for an APTES monolayer on silicon when reacted with **(red)** BiBB, **(blue)** BiBAn and **(green)** BiBNHS.

4.4. Conclusions

Tribochemical modification of OEG-NPEOC-APTES was demonstrated by moving an AFM tip in contact with the surface across a film of OEG-NPEOC-APTES. This is a new technique and a new approach to nanolithography that provides a way to produce features of only 10s of nanometres using only an AFM. When coupled with OEG-NPEOC-APTES, this technique has shown the potential to produce nanolines of proteins, potentially only one unit thick.

A threshold load was required in order to penetrate the surface of the monolayer, which was found to be 300 nN. Consistently reproducible results required a load of 500 nN. Feature widths and depths increased with increasing loads above this threshold, suggesting that partial deprotection occurs. Loads of greater than 10,000 nN were found to cleave the silane from the substrate. Whilst an increase in load has a large effect on feature sizes, a change in writing speed has an almost negligible effect. Depending on the load and writing speed, features could be produced with high reproducibility with widths of between 25 and 120 nm and depths between 0.1 and 0.7 nm.

Loads less than those required to fully cleave the silane were used, and a build-up of material at the edges of the features was observed suggesting that a physical deformation of the monolayer has occurred. Subsequent reactions show an identical likeness to those carried out on photodeprotected OEG-NPEOC-APTES, in turn suggesting that the location of the mechanochemical reaction to occur in the same place as the photodeprotection, though the nature of the exact mechanism is not yet known.

4.5. Future work

Though highly reproducible features were fabricated using tribochemical approach described in this chapter, attachment of proteins proved to be much more difficult. The aim must be to determine why the GFP attachment process has so far failed to prove effective or to find an alternative that doesn't rely on specific chemical binding schemes but rather on most protein's tendency to adsorb to most surfaces and on OEG-NPEOC-APTES's natural anti-fouling. The latter approach could produce simple protein patterns, but as the features are often much shallower and narrower than most protein moieties, the protein may be prevented from reaching the deprotected areas by surrounding OEG-NPEOC-APTES.

The growth of polymer brushes from nanolines also remains a key objective. As mentioned in section 4.3.4, alternative approaches to derivatising the modified OEG-NPEOC-APTES exist and can be explored further.

Should either of the above problems be addressed, the technique of tribochemical modification can be utilised to produce patterns of greater complexity than discussed here. The technique can be combined with photolithographic processes to produce multiple protein patterns and the use of a scriptwriting programme can allow for specific patterns to be drawn onto the surface which can be done sequentially between derivatisation steps to create closed systems on a scale close to that seen in photosynthetic bacteria.

5. Experimental

5.1. Procedures

AFM

In order to calculate the load applied to the surface through the tip, the signal generated by the photodetector must be converted into a force. This can be calculated from the following equation:

$$F = K \times DS \times V_{diff}$$

Where F is the force applied (nN), K is the spring constant of the cantilever (nN nm^{-1}), DS is the deflection sensitivity of the photodetector (nm V^{-1}) and V_{diff} is the difference between the in photodetector setpoint reading on the AFM when clear of the surface and when in contact (V). For the V_{diff} value to have meaning, it must be known how much the piezo actually moves for a given reading difference. This is the deflection sensitivity (*DS*). In order to calculate the DS, the cantilever is pressed into a mica surface, so chosen because the stiffness of mica is much greater than that of the cantilever, therefore any movement in the piezo can only correspond to deflection in cantilever. A force-distance measurement is taken, and the reciprocal of the gradient is the DS value used. This gradient is equivalent to that of the straight line in section C of figure 11, but instead the y-axis is the reading of the photodetector.

The spring constant was obtained by using the thermal noise calibration technique.[203] Individual cantilever values were

calculated by using software built into the Nanoscope software used to operate the AFM.

All tip induced electro-oxidative lithography and tribochemical lithography was performed in the contact mode regime. Data collection and lithography was carried out in air, under ambient pressure unless otherwise stated.

ATRP

The ATRP reactions that were undergone did not follow the usual methodology. Instead of the reaction being carried out in a carefully maintained oxygen free environment, they were instead performed in a system that contains air but also importantly a reducing agent that regenerates the oxidised catalyst that readily forms from radical termination reactions. As a result of the continually regenerating catalyst, much less needs to be present in the system than would be required for regular ATRP. This process is referred to as activators regenerated by electron transfer (*ARGET*) ATRP.[204–206]

Contact angles

Contact angle measurements were taken on a goniometer. A sessile drop of water was placed on the surface of the sample and the syringe removed from the drop and the contact angle is taken once the drop has stabilised, normally after about three seconds. Where possible, five contact angles are taken per sample and an average determined.

Fluorescence microscopy

Fluorescence images were collected using an Olympus FV1200 confocal microscope. The excitation source was a 488 nm argon

	laser and emission was collected in the range of 500-515 nm. Images were analysed and processed using FiJi software.
Piranha solution	A mixture of hydrogen peroxide and sulfuric acid is made with ratios of 3 : 7 respectively, with the hydrogen peroxide being added first. The resulting reaction is exothermic and reaches temperatures of 100 °C within a time frame of minutes and explodes when brought into contact with organics,[207] thus great care should be exercised when using piranha solution. Slides are left in the cleaning solution for times between thirty minutes and one hour.
RCA I	A mixture of deionised water, hydrogen peroxide and ammonia is made with ratios of 5 : 1 : 1 respectively and heated to 80 °C on a hot plate.[208] Once boiling the slides are left for thirty minutes before being taken off the heat.
Silane monolayer formation	Once the silane has been added to the solution, the sample vials were sonicated for two minutes, after which the slides are left for a set period of time for the monolayer to establish as described in the relevant experimental section. Unless otherwise stated, the following procedure takes place. The slides are rinsed first with toluene, second with a 1 : 1 mix of ethanol and toluene, before finally being rinsed with ethanol. The sample vials are then wrapped in aluminium foil and then placed in a vacuum oven set to a temperature of approximately 110 °C for

twenty minutes to anneal the silane and drive off any remaining solvent.

SIMS

A time of flight secondary ion mass spectrometer was used to analyse the sample, with a Bi_3^{++} cluster to interrogate the surface. The instrument was set up for optimum spatial resolution (burst alignment mode, using manufacturer defined default settings) or optimum mass resolution (high current bunched mode, using manufacturer defined default settings). For optimum mass resolution the pulse width is adjusted to achieve a target current of 0.1 nA. For optimum spatial resolution the beam is more tightly focused with a lower current. The beam is not pulsed. Mass range and area analysed are user specific. The base operating pressure was 1×10^{-9} Torr.

Thiol monolayer formation

Once the thiol had been added to the solution, the sample vials were sonicated for two minutes, after which the slides are left for a set period of time for the monolayer to establish as described in the relevant experimental section. Unless otherwise stated, the following procedure takes place. The slides are rinsed with degassed ethanol and dried with nitrogen gas. If not used immediately at this point, the slides are submerged in fresh degassed ethanol until use, upon which point they are rinsed again with fresh degassed ethanol and dried with nitrogen gas.

Thin film evaporation

Slides were mounted above the metal sources for evaporation within a glass bell jar. A diffusion pump was used to generate a

vacuum of 5 x 10^{-6} mbar before evaporation could take place. In the case of multiple evaporations, the system was allowed to cool for approximately 15 minutes after each previous evaporation in order to allow the vacuum to re-establish. The system was allowed to cool entirely before the bell jar was vented to atmosphere.

XPS

The area analysed for a large area scan is 700 µm by 300 µm. Charge neutralisation is used for insulating samples, being low energy electrons emitted from a tungsten filament. Monochromated aluminium radiation was used to collect XPS survey scans (wide scans) with a 160 eV pass energy and 1 eV intervals. High-resolution XPS spectra was collected at 20 eV pass energy, and 0.1 eV intervals. The base operating pressure was 1 x 10^{-9} Torr. The anode was run at 12 kV and 10 mA.

CASA XPS software was used to analyse and curve-fit the spectra. The raw data collected is corrected by a transmission function characteristic of the instrument, determined using software from the National Physics Laboratory. The adjusted data is then be quantified using the theoretically derived Scofield relative sensitivity factors that have been corrected for the geometry of the instrument. Charge correction typically carried out by making the main C 1s peak at 285.0 eV.

5.2. Chemicals and materials

2-[methoxy (polyethyleneoxy) propyl]-trichlorosilane	–	From Fluorochem
[4-(Chloromethyl) phenyl]-trichlorosilane	–	97 % from Alfa Aesar
Acetone	–	≥99.8% from Sigma Aldrich
AFM tips (writing/tapping mode imaging)	–	Model: OTESPA-R3 from Bruker
AFM tips (contact mode imaging)	–	Model: DNP-10 from Bruker
(S)-N-(5-Amino-1-carboxypentyl)iminodiacetic acid	–	>97% from Sigma Aldrich
Ammonia	–	32% from VWR
(3-Aminopropyl)triethoxysilane	–	99% from Sigma Aldrich
L-Ascorbic acid	–	Reagent grade from Sigma Aldrich
2,2′-Bipyridyl	–	≥99% from Sigma Aldrich
2-Bromoisobutanoic acid N-hydroxysuccinimide ester	–	98% from Sigma Aldrich
2-Bromoisobutyric anhydride	–	95% from Sigma Aldrich
α-Bromoisobutyryl bromide	–	98% from Sigma Aldrich
Chromium chips	–	99.5% from Sigma Aldrich
Copper(II) chloride	–	99% from Sigma Aldrich
Cysteine methacrylate	–	Custom synthesised

Dichloromethane	–	100% from VWR
Dodecanethiol	–	≥98% from Sigma Aldrich
Ethanol	–	≥99.7% from VWR
Finder grids	–	Type HF15 from Agar Scientific
Glass slides	–	D 263 M borosilicate, thickness 1.5 from Menzel-Gläser
Glutaraldehyde	–	Grade II, 25% in H_2O from Sigma Aldrich
Gold wire	–	0.5 mm diameter, 99.99% trace metal basis from Goodfellow
Green fluorescent protein	–	Custom synthesised
Hydrogen peroxide	–	30% from VWR
Nickel(II) chloride	–	98% from Sigma Aldrich
Octadecyltrichlorosilane	–	95 % from Fluorochem
OEG-NPEOC-APTES	–	Custom synthesised
Phosphate buffered saline	–	Tablet form, from Sigma Aldrich
Silicon wafers	–	Boron doped, (1,0,0), 1-10 Ω.cm, test grade from PI-KEM
Sulfuric acid	–	95% from VWR
Triethylamine	–	99% from Fluorochem
Toluene	–	99.9% from Sigma Aldrich

Toluene (dry)	–	Dry solvent system, department of chemistry, University of Sheffield
Water	–	15 MΩ.cm, from an Elga Purelab Option

5.3. Equipment

AFM	–	Digital Instruments Multimode with NanoScope IIIa controller
Confocal microscope	–	Olympus FV1200 confocal. The Wolfson Light Microscope Facility, Sheffield, UK
Goniometer	–	Ramé-Hart 100-00-230
SIMS	–	IONTOF TOF.SIMS 5. Sheffield Surface Analysis Centre, Sheffield, UK
Thin film evaporator	–	Edwards Auto 306
Vacuum oven	–	Technico TEC-240-010S
XPS	–	Kratos Axis Ultra DLD. Sheffield Surface Analysis Centre, Sheffield, UK

6. Acronyms and frequently used abbreviations

2DES	–	Two-dimensional electronic spectroscopy
ABNTA	–	(S)-N-(5-Amino-1-carboxypentyl)iminodiacetic acid
AFM	–	Atomic force microscope
APTES	–	(3-Aminopropyl)triethoxysilane
ATP	–	Adenosine triphosphate
ARGET	–	Activators regenerated by electron transfer
ATRP	–	Atom transfer radical polymerisation
BChl	–	Bacteriochlorophyll
BiBAn	–	2-Bromoisobutyric anhydride
BiBB	–	α-Bromoisobutyryl bromide
BiBNHS	–	2-Bromoisobutanoic acid N-hydroxysuccinimide ester
BIPY	–	2,2′-Bipyridyl
BPhe	–	Bacteriopheophytin
CMPTS	–	[4-(Chloromethyl) phenyl]-trichlorosilane
DCM	–	Dichloromethane
DMT	–	Deraguin-Muller-Toporov
DPN	–	Dip pen nanolithography

DS	–	Deflection sensitivity
EUV	–	Extreme ultraviolet
FFM	–	Frictional force microscopy
FRET	–	Fluorescence resonance energy transfer
FWHM	–	Full width at half maximum
GA	–	Glutaraldehyde
GFP	–	Green fluorescent protein
His	–	Histidine
IL	–	Interference lithography
JKR	–	Johnson-Kendall-Roberts
LFM	–	Lateral force microscopy
LH1	–	Light-harvesting complex one
LH2	–	Light-harvesting complex two
LSPR	–	Localised surface plasmon resonance
NPEOC	–	2-Nitrophenylethoxycarbonyl
NTA	–	Nitrilotriacetic acid
OEG	–	Oligo(ethylene glycol)

OEG-NPEOC-APTES	–	Oligo(ethylene glycol) nitrophenylethoxycarbonyl protected aminopropyltriethoxysilane
ODTMS	–	Octadecyltrimethoxysilane
ODTS	–	Octadecyltrichlorosilane
P	–	Special pair
PBS	–	Phosphate-buffered saline
PCysMA	–	Poly(cysteine methacrylate)
PDB	–	Protein data bank
PDMS	–	Polydimethylsiloxane
PEG	–	Poly(ethylene glycol)
Rba	–	Rhodobacter
RC	–	Reaction centre
RCA I	–	Radio corporation of America standard clean one
RET	–	Resonance energy transfer
SAM	–	Self-assembled monolayer
SIMS	–	Secondary ion mass spectrometry
SNOM	–	Scanning near-field microscope
SP	–	Surface plasmon

SPR	–	Surface plasmon resonance
STM	–	Scanning tunnelling microscopy
TEA	–	Triethylamine
ToF	–	Time of flight
UHV	–	Ultrahigh vacuum
UV	–	Ultraviolet
XPS	–	X-ray photoemission spectroscopy
λ	–	Wavelength

7. Bibliography

1 J. Strümpfer, M. Şener and K. Schulten, "How quantum coherence assists photosynthetic light-harvesting", *J. Phys. Chem. Lett.*, 2012, **3**, pp. 536–542.

2 F. Fassioli, R. Dinshaw, P. C. Arpin and G. D. Scholes, "Photosynthetic light harvesting: Excitons and coherence", *J. R. Soc. Interface*, 2014, **11**, p. 20130901.

3 M. R. Jones, "The petite purple photosynthetic powerpack", *Biochem. Soc. Trans.*, 2009, **37**, pp. 400–407.

4 U. Ermler, G. Fritzsch, S. K. Buchanan and H. Michel, "Structure of the photosynthetic reaction centre from Rhodobacter sphaeroides at 2.65 Å resolution: Cofactors and protein-cofactor interactions", *Structure*, 1994, **2**, pp. 925–936.

5 M. F. Sanner, "Python: A programming language for software integration and development", *J. Mol. Graph. Model.*, 1999, **17**, pp. 57–61.

6 W. Zinth and J. Wachtveitl, "The first picoseconds in bacterial photosynthesis - ultrafast electron transfer for the efficient conversion of light energy", *ChemPhysChem*, 2005, **6**, pp. 871–880.

7 G. D. Scholes, G. R. Fleming, A. Olaya-Castro and R. van Grondelle, "Lessons from nature about solar light harvesting", *Nat. Chem.*, 2011, **3**, pp. 763–774.

8 X. Hu and K. Schulten, "Model for the light-harvesting complex I (B875) of Rhodobacter sphaeroides", *Biophys. J.*, 1998, **75**, pp. 683–694.

9 M. L. Cartron, J. D. Olsen, M. Sener, P. J. Jackson, A. A. Brindley, P. Qian, M. J. Dickman, G. J. Leggett, K. Schulten and C. Neil Hunter, "Integration of energy and electron transfer processes in the photosynthetic membrane of Rhodobacter sphaeroides", *Biochim. Biophys. Acta*, 2014, **1837**, pp. 1769–1780.

10 T. Förster, "Energiewanderung and fluoreszenz", *Naturwissenschaften*, 1946, **33**, pp. 166–175.

11 T. Förster, "Zwischenmolekulare energiewanderung und fluoreszenz", *Ann. Phys.*, 1948, **437**, pp. 55–75.

12 M. Şener, J. Strümpfer, J. Hsin, D. Chandler, S. Scheuring, C. N. Hunter and K. Schulten, "Förster energy transfer theory as reflected in the structures of photosynthetic light-harvesting systems", *ChemPhysChem*, 2011, **12**, pp. 518–531.

13 S. Hess, K. J. Visscher, T. Pullerits, V. Sundström, G. J. S. Fowler and C. N. Hunter, "Enhanced rates of subpicosecond energy transfer in blue-shifted light harvesting LH2 mutants of Rhodobacter sphaeroides", *Biochemistry*, 1994, **33**, pp. 8300–8305.

14 R. Jimenez, S. N. Dikshit, S. E. Bradforth and G. R. Fleming, "Electronic excitation transfer in the LH2 complex of Rhodobacter sphaeroides", *J. Phys. Chem.*, 1996, **100**, pp. 6825–6834.

15 T. Pullerits, S. Hess, J. L. Herek and V. Sundström, "Temperature dependence of excitation transfer in LH2 of Rhodobacter sphaeroides", *J. Phys. Chem. B*, 1997, **101**, pp. 10560–10567.

16 J. M. Anna, G. D. Scholes and R. Van Grondelle, "A little coherence in photosynthetic light harvesting", *Bioscience*, 2014, **64**, pp. 14–25.

17 H. Lee, Y.-C. Cheng and G. R. Fleming, “Coherence dynamics in photosynthesis: protein protection of excitonic coherence.”, *Science (80-.).*, 2007, **316**, pp. 1462–1465.

18 G. S. Engel, T. R. Calhoun, E. L. Read, T.-K. Ahn, T. Mančal, Y.-C. Cheng, R. E. Blankenship and G. R. Fleming, “Evidence for wavelike energy transfer through quantum coherence in photosynthetic systems”, *Nature*, 2007, **446**, pp. 782–786.

19 B. P. Krueger, G. D. Scholes and G. R. Fleming, “Calculation of couplings and energy-transfer pathways between the pigments of LH2 by the ab initio transition density cube method”, *J. Phys. Chem. B*, 1998, **102**, pp. 5378–5386.

20 G. D. Scholes and G. R. Fleming, “On the mechanism of light harvesting in photosynthetic purple bacteria: B800 to B850 energy transfer”, *J. Phys. Chem. B*, 2000, **104**, pp. 1854–1868.

21 X. Hu, T. Ritz, A. Damjanović and K. Schulten, “Pigment organization and transfer of electronic excitation in the photosynthetic unit of purple bacteria”, *J. Phys. Chem. B*, 1997, **101**, pp. 3854–3871.

22 T. Förster, “Delocalized excitation and excitation transfer”, in *Modern Quantum Chemistry - Istanbul Lectures Part III: Action of Light and Organic Crystals*, ed. by O. Sinanoğlu, Academic Press Inc. (London) Ltd., London, 1965, 1st ed., pp. 93–137.

23 R. S. Knox, “Excitation energy transfer and migration: Theoretical considerations”, in *Bioenergetics of Photosynthesis*, ed. by Govindjee, Academic Press Inc. (London) Ltd., London, 1975, 1st ed., pp. 183–223.

24 J. D. Hybl, A. W. Albrecht, S. M. Gallagher Faeder and D. M. Jonas, “Two-dimensional electronic spectroscopy”, *Chem. Phys. Lett.*, 1998, **297**, pp. 307–313.

25 T. Brixner, J. Stenger, H. M. Vaswani, M. Cho, R. E. Blankenship and G. R. Fleming, “Two-dimensional spectroscopy of electronic couplings in photosynthesis”, *Nature*, 2005, **434**, pp. 625–628.

26 J. M. Anna, Y. Song, R. Dinshaw and G. D. Scholes, “Two-dimensional electronic spectroscopy for mapping molecular photophysics”, *Pure Appl. Chem.*, 2013, **85**, pp. 1307–1319.

27 W. L. Barnes, A. Dereux and T. W. Ebbesen, “Surface plasmon subwavelength optics”, *Nature*, 2003, **424**, pp. 824–30.

28 K. A. Willets and R. P. Van Duyne, “Localized surface plasmon resonance spectroscopy and sensing”, *Annu. Rev. Phys. Chem.*, 2007, **58**, pp. 267–297.

29 B. Liedberg, C. Nylander and I. Lunström, “Surface plasmon resonance for gas detection and biosensing”, *Sensors and Actuators*, 1983, **4**, pp. 299–304.

30 J. M. Brockman, A. G. Frutos and R. M. Corn, “A multistep chemical modification procedure to create DNA arrays on gold surfaces for the study of protein-DNA interactions with surface plasmon resonance imaging”, *J. Am. Chem. Soc.*, 1999, **121**, pp. 8044–8051.

31 C. R. Yonzon, E. Jeoung, S. Zou, G. C. Schatz, M. Mrksich and R. P. Van Duyne, “A comparative analysis of localized and propagating surface plasmon resonance sensors: The binding of Concanavalin A to a monosaccharide functionalized self-assembled monolayer”, *J. Am. Chem. Soc.*, 2004, **126**, pp. 12669–12676.

32 R. P. Van Duyne, “Molecular plasmonics”, *Science (80-.).*, 2004, **306**, pp. 985–986.

33 P. Andrew and W. L. Barnes, “Energy transfer across a metal film mediated by surface plasmon polaritons”, *Science (80-.).*, 2004, **306**, pp. 1002–1005.

34 K. L. Kelly, E. Coronado, L. L. Zhao and G. C. Schatz, “The optical properties of metal nanoparticles: The influence of size, shape, and dielectric environment”, *J. Phys. Chem. B*, 2003, **107**, pp. 668–677.

35 T. R. Jensen, M. L. Duval, K. L. Kelly, A. A. Lazarides, G. C. Schatz and R. P. Van Duyne, “Nanosphere lithography: Effect of the external dielectric medium on the surface plasmon resonance spectrum of a periodic array of silver nanoparticles”, *J. Phys. Chem. B*, 1999, **103**, pp. 9846–9853.

36 J. J. Mock, M. Barbic, D. R. Smith, D. A. Schultz and S. Schultz, “Shape effects in plasmon resonance of individual colloidal silver nanoparticles”, *J. Chem. Phys.*, 2002, **116**, p. 6755.

37 M. M. Miller and A. A. Lazarides, “Sensitivity of metal nanoparticle surface plasmon resonance to the dielectric environment”, *J. Phys. Chem. B*, 2005, **109**, pp. 21556–21565.

38 A. Tsargorodska, O. El Zubir, B. Darroch, M. L. Cartron, T. Basova, C. N. Hunter, A. V. Nabok and G. J. Leggett, “Fast, simple, combinatorial routes to the fabrication of reusable, plasmonically active gold nanostructures by interferometric lithography of self-assembled monolayers”, *ACS Nano*, 2014, **8**, pp. 7858–7869.

39 J. C. Riboh, A. J. Haes, A. D. McFarland, C. R. Yonzon and R. P. Van Duyne, “A nanoscale optical biosensor: Real-time immunoassay in physiological buffer enabled by improved nanoparticle adhesion”, *J. Phys. Chem. B*, 2003, **107**, pp. 1772–1780.

40 A. D. McFarland and R. P. Van Duyne, “Single silver nanoparticles as real-time optical sensors with zeptomole sensitivity”, *Nano Lett.*, 2003, **3**, pp. 1057–1062.

41 A. J. Haes, C. L. Haynes, A. D. McFarland, G. C. Schatz, R. P. Van Duyne and S. Zou, “Plasmonic materials for surface-enhanced sensing and spectroscopy”, *MRS Bull.*, 2005, **30**, pp. 368–375.

42 B. M. Reinhard, M. Siu, H. Agarwal, A. P. Alivisatos and J. Liphardt, “Calibration of dynamic molecular rulers based on plasmon coupling between gold nanoparticles”, *Nano Lett.*, 2005, **5**, pp. 2246–2252.

43 C. Sönnichsen, B. M. Reinhard, J. Liphardt and A. P. Alivisatos, “A molecular ruler based on plasmon coupling of single gold and silver nanoparticles”, *Nat. Biotechnol.*, 2005, **23**, pp. 741–745.

44 I. Langmuir, “The constitution and fundamental properties of solids and liquids. II. Liquids”, *J. Am. Chem. Soc.*, 1917, **39**, pp. 1848–1906.

45 K. B. Blodgett and I. Langmuir, “Built-up films of barium and their optical properties”, *Phys. Rev.*, 1937, **51**, pp. 964–982.

46 W. C. Bigelow, D. L. Pickett and W. A. Zisman, “Oleophobic monolayers. I. Films adsorbed from solution in non-polar liquids”, *J. Colloid Sci.*, 1946, **1**, pp. 513–538.

47 R. C. Waldbillig, J. D. Robertson and T. J. McIntosh, “Images of divalent cations in unstained symmetric and asymmetric lipid bilayers”, *Biochim. Biophys. Acta*, 1976,

448, pp. 1–14.

48 T. J. McIntosh, R. C. Waldbillig and J. D. Robertson, “Lipid bilayer ultrastructure: Electron density profiles and chain tilt angles as determined by X-ray diffraction”, *Biochim. Biophys. Acta*, 1976, **448**, pp. 15–33.

49 D. G. Whitten, “Photochemical reactions of surfactant molecules in condensed monolayer assemblies-environmental control and modification of reactivity”, *Angew. Chem. Int. Ed. Engl.*, 1979, **18**, pp. 440–450.

50 M. A. Richard, J. Deutch and G. M. Whitesides, “Hydrogenation of oriented monolayers of ω-unsaturated fatty acids supported on platinum”, *J. Am. Chem. Soc.*, 1978, **100**, pp. 6613–6625.

51 R. R. Durand, C. S. Bencosme, J. P. Collman and F. C. Anson, “Mechanistic aspects of the catalytic reduction of dioxygen by cofacial metalloporphyrins”, *J. Am. Chem. Soc.*, 1983, **105**, pp. 2710–2718.

52 A. T. Hubbard, “Electrochemistry of well-defined surfaces”, *Acc. Chem. Res.*, 1980, **13**, pp. 177–184.

53 E. E. Polymeropoulos and J. Sagiv, “Electrical conduction through adsorbed monolayers”, *J. Chem. Phys.*, 1978, **69**, pp. 1836–1847.

54 J. Sagiv, “Organized monolayers by adsorption. 1. Formation and structure of oleophobic mixed monolayers on solid surfaces”, *J. Am. Chem. Soc.*, 1980, **102**, pp. 92–98.

55 M. P. Soriaga and A. T. Hubbard, “Determination of the orientation of aromatic molecules adsorbed on platinum electrodes. The effect of solute concentration”, *J. Am. Chem. Soc.*, 1982, **104**, pp. 3937–3945.

56 R. G. Nuzzo and D. L. Allara, “Adsorption of bifunctional organic disulfides on gold surfaces”, *J. Am. Chem. Soc.*, 1983, **105**, pp. 4481–4483.

57 M. Pomerantz, A. Segmüller, L. Netzer and J. Sagiv, “Coverage of Si substrates by self-assembling monolayers and multilayers as measured by IR, wettability and X-ray diffraction”, *Thin Solid Films*, 1985, **132**, pp. 153–162.

58 C. D. Bain and G. M. Whitesides, “Formation of monolayers by the coadsorption of thiols on gold: Variation in the length of the alkyl chain”, *J. Am. Chem. Soc.*, 1989, **111**, pp. 7164–7175.

59 C. D. Bain, E. B. Troughton, Y.-T. Tao, J. Evall, G. M. Whitesides and R. G. Nuzzo, “Formation of monolayer films by the spontaneous assembly of organic thiols from solution onto gold”, *J. Am. Chem. Soc.*, 1989, **111**, pp. 321–335.

60 R. G. Nuzzo, F. A. Fusco and D. L. Allara, “Spontaneously organized molecular assemblies. 3. Preparation and properties of solution adsorbed monolayers of organic disulfides on gold surfaces”, *J. Am. Chem. Soc.*, 1987, **109**, pp. 2358–2368.

61 M. D. Porter, T. B. Bright, D. L. Allara and C. E. D. Chidsey, “Spontaneously organized molecular assemblies. 4. Structural characterization of n-alkyl thiol monolayers on gold by optical ellipsometry, infrared spetcroscopy, and electrochemistry”, *J. Am. Chem. Soc.*, 1987, **109**, pp. 3559–3568.

62 L. Strong and G. M. Whitesides, “Structures of self-assembled monolayer films of

organosulfur compounds adsorbed on gold single crystals: Electron diffraction studies", *Langmuir*, 1988, **4**, pp. 546–558.

63 C. D. Bain, J. Evall and G. M. Whitesides, "Formation of monolayers by the coadsorption of thiols on gold: Variation in the head group, tail group, and solvent", *J. Am. Chem. Soc.*, 1989, **111**, pp. 7155–7164.

64 C. D. Bain, H. A. Biebuyck and G. M. Whitesides, "Comparison of self-assembled monolayers on gold: Coadsorption of thiols and disulfides", *Langmuir*, 1989, **5**, pp. 723–727.

65 R. G. Nuzzo, B. R. Zegarski and L. H. Dubois, "Fundamental studies of the chemisorption of organosulfur compounds on Au(111). Implications for molecular self-assembly on gold surfaces", *J. Am. Chem. Soc.*, 1987, **109**, pp. 733–740.

66 R. G. Nuzzo, L. H. Dubois and D. L. Allara, "Fundamental studies of microscopic wetting on organic surfaces. 1. Formation and structural characterization of a self-consistent series of polyfunctional organic monolayers", *J. Am. Chem. Soc.*, 1990, **112**, pp. 558–569.

67 M. A. Bryant and J. E. Pemberton, "Surface raman scattering of self-assembled monolayers formed from 1-alkanethiols: Behavior of films at Au and comparison to films at Ag", *J. Am. Chem. Soc.*, 1991, **113**, pp. 8284–8293.

68 L. Kankate, A. Turchanin and A. Gölzhäuser, "On the release of hydrogen from the S-H groups in the formation of self-assembled monolayers of thiols", *Langmuir*, 2009, **25**, pp. 10435–10438.

69 J. C. Love, L. A. Estroff, J. K. Kriebel, R. G. Nuzzo and G. M. Whitesides, "Self-assembled monolayers of thiolates on metals as a form of nanotechnology", *Chem. Rev.*, 2005, **105**, pp. 1103–1169.

70 N. Camillone III, C. E. D. Chidsey, G. Liu and G. Scoles, "Superlattice structure at the surface of a monolayer of octadecanethiol self-assembled on Au(111)", *J. Chem. Phys.*, 1993, **98**, pp. 3503–3511.

71 N. Camillone III, C. E. D. Chidsey, P. Eisenberger, P. Fenter, J. Li, K. S. Liang, G.-Y. Liu and G. Scoles, "Structural defects in self-assembled organic monolayers via combined atomic beam and x-ray diffraction", *J. Chem. Phys.*, 1993, **99**, pp. 744–747.

72 C. Fan, K. W. Plaxco and A. J. Heeger, "Electrochemical interrogation of conformational changes as a reagentless method for the sequence-specific detection of DNA", *Proc. Natl. Acad. Sci. U. S. A.*, 2003, **100**, pp. 9134–9137.

73 J. A. Hansen, J. Wang, A.-N. Kawde, Y. Xiang, K. V. Gothelf and G. Collins, "Quantum-dot/aptamer-based ultrasensitive multi-analyte electrochemical biosensor", *J. Am. Chem. Soc.*, 2006, **128**, pp. 2228–2229.

74 F. Ricci, R. Y. Lai and K. W. Plaxco, "Linear, redox modified DNA probes as electrochemical DNA sensors", *Chem. Commun.*, 2007, pp. 3768–3770.

75 S. Hong, T. Kang, J. Moon, S. Oh and J. Yi, "Surface plasmon resonance analysis of aqueous copper ions with amino-terminated self-assembled monolayers", *Colloids Surfaces A Physicochem. Eng. Asp.*, 2007, **292**, pp. 264–270.

76 N. Phares, R. J. White and K. W. Plaxco, "Improving the stability and sensing of electrochemical biosensors by employing trithiol-anchoring groups in a six-carbon

self-assembled monolayer", *Anal. Chem.*, 2009, **81**, pp. 1095–1100.

77 Z. Weng and F. Zaera, "Increase in activity and selectivity in catalysis via surface modification with self-assembled monolayers", *J. Phys. Chem. C*, 2014, **118**, pp. 3672–3679.

78 T. Taguchi, K. Isozaki and K. Miki, "Enhanced catalytic activity of self-assembled-monolayer-capped gold nanoparticles", *Adv. Mater.*, 2012, **24**, pp. 6462–6467.

79 S. Chatterjee, K. Sengupta, S. Samanta, P. K. Das and A. Dey, "Electrocatalytic O2 reduction reaction by synthetic analogues of cytochrome P450 and myoglobin: In-situ resonance raman and dynamic electrochemistry investigations", *Inorg. Chem.*, 2013, **52**, pp. 9897–9907.

80 W. Wang, T. Lee and M. A. Reed, "Mechanism of electron conduction in self-assembled alkanethiol monolayer devices", *Phys. Rev. B*, 2003, **68**, pp. 035416/1-035416/7.

81 H. B. Akkerman, P. W. M. Blom, D. M. de Leeuw and B. de Boer, "Towards molecular electronics with large-area molecular junctions", *Nature*, 2006, **441**, pp. 69–72.

82 H.-S. Choi, Y. Kang, H. Lee and C. Lee, "Photopatterning of gold and copper surfaces by using self-assembled monolayers", *Curr. Appl. Phys.*, 2007, **7**, pp. 522–527.

83 D. P. Dowling, K. Donnelly, M. L. McConnell, R. Eloy and M. N. Arnaud, "Deposition of anti-bacterial silver coatings on polymeric substrates", *Thin Solid Films*, 2001, **398–399**, pp. 602–606.

84 R. Maoz and J. Sagiv, "On the formation and structure of self-assembling monolayers. I. A comparative ATR-wettability study of Langmuir-Blodgett and adsorbed films on flat substrates and glass microbeads", *J. Colloid Interface Sci.*, 1984, **100**, pp. 465–496.

85 M. J. Stevens, "Thoughts on the structure of alkylsilane monolayers", *Langmuir*, 1999, **15**, pp. 2773–2778.

86 R. Maoz, J. Sagiv, D. Degenhardt, H. Möhwald and P. Quint, "Hydrogen-bonded multilayers of self-assembling silanes: Structure elucidation by combined Fourier transform infra-red spectroscopy and X-ray scattering techniques", *Supramol. Sci.*, 1995, **2**, pp. 9–24.

87 R. R. Rye, G. C. Nelson and M. T. Dugger, "Mechanistic aspects of alkylchlorosilane coupling reactions", *Langmuir*, 1997, **13**, pp. 2965–2972.

88 D. K. Aswal, S. Lenfant, D. Guerin, J. V. Yakhmi and D. Vuillaume, "Self assembled monolayers on silicon for molecular electronics", *Anal. Chim. Acta*, 2006, **568**, pp. 84–108.

89 M. M. Walczak, C. Chung, S. M. Stole, C. A. Widrig and M. D. Porter, "Structure and interfacial properties of spontaneously adsorbed n-alkanethiolate monolayers on evaporated silver surfaces", *J. Am. Chem. Soc.*, 1991, **113**, pp. 2370–2378.

90 B. D. Ratner and D. G. Castner, "Electron spectroscopy for chemical analysis", in *Surface Analysis - The Principal Techniques*, ed. by J. C. Vickerman and I. S. Gilmore, John Wiley & Sons, Ltd, Chichester, UK, 2009, 2nd ed., pp. 47–112.

91 D. Briggs and J. C. Rivière, “Spectral interpretation”, in *Practical Surface Analysis: Volume 1 - Auger and X-ray Photoelectron Spectroscopy*, ed. by D. Briggs and M. P. Seah, John Wiley & Sons, Ltd., Chichester, UK, 1990, 2nd ed., pp. 85–141.

92 A. F. Orchard, “Basic principles of photoelectron spectroscopy”, in *Handbook of X-ray and Ultraviolet Photoelectron Spectroscopy*, ed. by D. Briggs, Heyden & Son Ltd., London, 1977, 1st ed., pp. 1–77.

93 S. Hofmann, “Depth profiling in AES and XPS”, in *Practical Surface Analysis: Volume 1 - Auger and X-ray Photoelectron Spectroscopy*, ed. by D. Briggs and M. P. Seah, John Wiley & Sons, Ltd., Chichester, UK, 1990, 2nd ed., pp. 143–199.

94 A. Barrie, “Instrumentation for electron spectroscopy”, in *Handbook of X-ray and Ultraviolet Photoelectron Spectroscopy*, ed. by D. Briggs, Heyden & Son Ltd., London, 1977, 1st ed., pp. 79–119.

95 L. A. McDonnell and R. M. A. Heeren, “Imaging mass spectrometry”, *Mass Spectrom. Rev.*, 2007, **26**, pp. 606–643.

96 A. J. Eccles, “SIMS instrumentation”, in *Secondary Ion Mass Spectrometry - Principle and Applications*, ed. by J. C. Vickerman, A. Brown, and N. M. Reed, Oxford University Press, Oxford, 1989, 1st ed.

97 L. Van Vaeck, A. Adriaens and R. Gijbels, “Static secondary ion mas spectrometry (S-SIMS) Part 1: Methodology and structural interpretation”, *Mass Spectrom. Rev.*, 1999, **18**, pp. 1–47.

98 J. C. Vickerman and A. J. Swift, “Secondary ion mass spectrometry - the surface mass spectrometry”, in *Surface Analysis - The Principal Techniques*, ed. by J. C. Vickerman, John Wiley & Sons, Ltd, Chichester, UK, 1997, 1st ed.

99 A. Benninghoven, “The analysis of monomolecular layers of solids by secondary ion emission”, *Z. Phys.*, 1970, **230**.

100 B. Hagenhoff, R. Kersting and D. Rading, “Ion Beam Techniques: Time-of-Flight Secondary Ion Mass Spectrometry (ToF-SIMS)”, in *Handbook of Surface and Interface Analysis: Methods for Problem-Solving*, ed. by J. C. Rivière and S. Myhra, CRC Press, Boca Raton, FL, USA, 2009, 2nd ed.

101 P. Williams, “The sputtering process and sputtered ion emission”, *Surf. Sci.*, 1979, **90**, pp. 588–634.

102 P. Williams, “On mechanisms of sputtered ion emission”, *Appl. Surf. Sci.*, 1982, **13**, pp. 241–259.

103 A. Wucher, “Formation of atomic secondary ions in sputtering”, *Appl. Surf. Sci.*, 2008, **255**, pp. 1194–1200.

104 A. Wucher, B. Weidtmann and A. Duvenbeck, “A microscopic view of secondary ion formation”, *Nucl. Instruments Methods Phys. Res. Sect. B Beam Interact. with Mater. Atoms*, 2013, **303**, pp. 108–111.

105 D. Weibel, S. Wong, N. Lockyer, P. Blenkinsopp, R. Hill and J. C. Vickerman, “A C 60 Primary Ion Beam System for Time of Flight Secondary Ion Mass Spectrometry: Its Development and Secondary Ion Yield Characteristics”, *Anal. Chem.*, 2003, **75**, pp. 1754–1764.

106 A. Tempez, J. A. Schultz, S. Della-Negra, J. Depauw, D. Jacquet, A. Novikov, Y. Lebeyec, M. Pautrat, M. Caroff, M. Ugarov, H. Bensaoula, M. Gonin, K. Fuhrer and A. Woods, "Orthogonal time-of-flight secondary ion mass spectrometric analysis of peptides using large gold clusters as primary ions", *Rapid Commun. Mass Spectrom.*, 2004, **18**, pp. 371–376.

107 P. Humphrey, "SIMS Imaging", in *Secondary Ion Mass Spectrometry - Principle and Applications*, ed. by J. C. Vickerman, A. Brown, and N. M. Reed, Oxford University Press, Oxford, 1989, 1st ed.

108 G. Binnig, C. F. Quate and C. Gerber, "Atomic Force Microscope", *Phys. Rev. Lett.*, 1986, **56**, pp. 930–933.

109 G. J. Leggett, "Scanning Probe Microscopy", in *Surface Analysis - The Principal Techniques*, ed. by J. C. Vickerman and I. S. Gilmore, John Wiley & Sons, Ltd, Chichester, UK, 2009, 2nd ed., pp. 479–562.

110 V. L. Popov, *Contact Mechanics and Friction*, Springer-Verlag Berlin Heidelberg, Heidelberg, Germany, 2017, 2nd ed.

111 J. R. Barber, *Contact Mechanics*, Springer International Publishing AG, Cham, Switzerland, 2018, 1st ed.

112 K. L. Johnson, *Contact Mechanics*, Cambridge University Press, Cambridge, UK, 1985, 1st ed.

113 G. Haugstad, W. L. Gladfelter, E. B. Weberg, R. T. Weberg and R. R. Jones, "Probing molecular relaxation on polymer surfaces with friction force microscopy", *Langmuir*, 1995, **11**, pp. 3473–3482.

114 A. Kumar, H. A. Biebuyck, N. L. Abbott and G. M. Whitesides, "The use of self-assembled monolayers and a selective etch to generate patterned gold features", *J. Am. Chem. Soc.*, 1992, **114**, pp. 9188–9189.

115 E. Ul-Haq, S. Patole, M. Moxey, E. Amstad, C. Vasilev, C. N. Hunter, G. J. Leggett, N. D. Spencer and N. H. Williams, "Photocatalytic nanolithography of self-assembled monolayers and proteins", *ACS Nano*, 2013, **7**, pp. 7610–7618.

116 A. Kumar and G. M. Whitesides, "Features of gold having micrometer to centimeter dimensions can be formed through a combination of stamping with an elastomeric stamp and an alkanethiol 'ink' followed by chemical etching", *Appl. Phys. Lett.*, 1993, **63**, pp. 2002–2004.

117 Y. Xia, M. Mrksich, E. Kim and G. M. Whitesides, "Microcontact printing of octadecylsiloxane on the surface of silicon dioxide and its application in microfabrication", *J. Am. Chem. Soc.*, 1995, **117**, pp. 9576–9577.

118 C. D. James, R. C. Davis, L. Kam, H. G. Craighead, M. Isaacson, J. N. Turner and W. Shain, "Patterned protein layers on solid substrates by thin stamp microcontact printing", *Langmuir*, 1998, **14**, pp. 741–744.

119 Y. Xia and G. M. Whitesides, "Soft lithography", *Angew. Chem. Int. Ed.*, 1998, **37**, pp. 550–575.

120 A. Kumar, H. A. Biebuyck and G. M. Whitesides, "Patterning self-assembled monolayers: Applications in materials science", *Langmuir*, 1994, **10**, pp. 1498–1511.

121 C. S. Chen, M. Mrksich, S. Huang, G. M. Whitesides and D. E. Ingber, “Micropatterned surfaces for control of cell shape, position, and function”, *Biotechnol. Prog.*, 1998, **14**, pp. 356–363.

122 S. Liang, M. Chen and Q. Xue, “Deposition behaviors and patterning of TiO2 thin films on different SAMs surfaces from titanium sulfate aqueous solution”, *Colloids Surfaces A Physicochem. Eng. Asp.*, 2008, **324**, pp. 137–142.

123 S. Alom Ruiz and C. S. Chen, “Microcontact printing: A tool to pattern”, *Soft Matter*, 2007, **3**, pp. 1–11.

124 W. S. Dillmore, M. N. Yousaf and M. Mrksich, “A photochemical method for patterning the immobilization of ligands and cells to self-assembled monolayers”, *Langmuir*, 2004, **20**, pp. 7223–7231.

125 R. D. Piner and C. A. Mirkin, “Effect of water on lateral force microscopy in air”, *Langmuir*, 1997, **13**, pp. 6864–6868.

126 R. D. Piner, J. Zhu, F. Xu, S. Hong and C. A. Mirkin, “‘Dip-pen’ nanolithography”, *Science (80-.).*, 1999, **283**, pp. 661–663.

127 S. Hong, J. Zhu and C. A. Mirkin, “Multiple ink nanolithography: Toward a multiple-pen nano-plotter”, *Science (80-.).*, 1999, **286**, pp. 523–525.

128 S. E. Kooi, L. A. Baker, P. E. Sheehan and L. J. Whitman, “Dip-pen nanolithography of chemical templates on silicon oxide”, *Adv. Mater.*, 2004, **16**, pp. 1013–1016.

129 M. Su, M. Aslam, L. Fu, N. Wu and V. P. Dravid, “Dip-pen nanopatterning of photosensitive conducting polymer using a monomer ink”, *Appl. Phys. Lett.*, 2004, **84**, pp. 4200–4202.

130 L. M. Demers, D. S. Ginger, S.-J. Park, Z. Li, S.-W. Chung and C. A. Mirkin, “Direct patterning of modified oligonucleotides on metals and insulators by dip-pen nanolithography”, *Science (80-.).*, 2002, **296**, pp. 1836–1838.

131 B. W. Maynor, Y. Li and J. Liu, “Au ‘ink’ for AFM ‘dip-pen’ nanolithography”, *Langmuir*, 2001, **17**, pp. 2575–2578.

132 L. A. Porter Jr., H. C. Choi, J. M. Schmeltzer, A. E. Ribbe, L. C. C. Elliott and J. M. Buriak, “Electroless nanoparticle film deposition compatible with photolithography, microcontact printing, and dip-pen nanolithography patterning technologies”, *Nano Lett.*, 2002, **2**, pp. 1369–1372.

133 P. J. Thomas, G. U. Kulkarni and C. N. R. Rao, “Dip-pen lithography using aqueous metal nanocrystal dispersions”, *J. Mater. Chem.*, 2004, **14**, pp. 625–628.

134 L. Ding, Y. Li, H. Chu, X. Li and J. Liu, “Creation of cadmium sulfide nanostructures using AFM dip-pen nanolithography”, *J. Phys. Chem. B*, 2005, **109**, pp. 22337–22340.

135 K. Salaita, Y. Wang and C. A. Mirkin, “Applications of dip-pen nanolithography”, *Nat. Nanotechnol.*, 2007, **2**, pp. 145–155.

136 C. S. Dulcey, J. H. Georger Jr., V. Krauthamer, D. A. Stenger, T. L. Fare and J. M. Calvert, “Deep UV photochemistry of chemisorbed monolayers: Patterned coplanar molecular assemblies”, *Science (80-.).*, 1991, **252**, pp. 551–554.

137 J. Huang and J. C. Hemminger, “Photooxidation of thiols in self-assembled monolayers on gold”, *J. Am. Chem. Soc.*, 1993, **115**, pp. 3342–3343.

138 M. J. Tarlov, D. R. F. Burgess Jr. and G. Gillen, “UV photopatterning of alkanethiolate monolayers self-assembled on gold and silver”, *J. Am. Chem. Soc.*, 1993, **115**, pp. 5305–5306.

139 M. J. Tarlov and J. G. Newman, “Static secondary ion mass spectrometry of self-assembled alkanethiol monolayers on gold”, *Langmuir*, 1992, **8**, pp. 1398–1405.

140 S. P. A. Fodor, J. L. Read, M. C. Pirrung, L. Stryer, A. T. Lu and D. Solas, “Light-directed, spatially addressable parallel chemical synthesis”, *Science (80-.).*, 1991, **251**, pp. 767–773.

141 S. A. A. Ahmad, L. S. Wong, E. Ul-Haq, J. K. Hobbs, G. J. Leggett and J. Micklefield, “Protein micro- and nanopatterning using aminosilanes with protein-resistant photolabile protecting groups”, *J. Am. Chem. Soc.*, 2011, **133**, pp. 2749–2759.

142 T. Weimann, W. Geyer, P. Hinze, V. Stadler, W. Eck and A. Gölzhäuser, “Nanoscale patterning of self-assembled monolayers by e-beam lithography”, *Microelectron. Eng.*, 2001, **57–58**, pp. 903–907.

143 Y. Shin, S. Han, J. S. Jeon, K. Yamamoto, I. K. Zervantonakis, R. Sudo, R. D. Kamm and S. Chung, “Microfluidic assay for simultaneous culture of multiple cell types on surfaces or within hydrogels”, *Nat. Protoc.*, 2012, **7**, pp. 1247–1259.

144 G. J. Leggett, “Scanning near-field photolithography - surface photochemistry with nanoscale spatial resolution”, *Chem. Soc. Rev.*, 2006, **35**, pp. 1150–1161.

145 G. E. Moore, “Progress in digital integrated electronics”, in *Electron Devices Meetings, 1975 International*, 1975, 21, pp. 11–13.

146 E. Betzig and J. K. Trautman, “Near-field optics: Microscopy, spectroscopy, and surface modification beyond the diffraction limit”, *Science (80-.).*, 1992, **257**, pp. 189–195.

147 E. Betzig, J. K. Trautman, R. Wolfe, E. M. Gyorgy, P. L. Finn, M. H. Kryder and C.-H. Chang, “Near-field magneto-optics and high density data storage”, *Appl. Phys. Lett.*, 1992, **61**, pp. 142–144.

148 S. Sun and G. J. Leggett, “Matching the resolution of electron beam lithography by scanning near-field photolithography”, *Nano Lett.*, 2004, **4**, pp. 1381–1384.

149 M. Montague, R. E. Ducker, K. S. L. Chong, R. J. Manning, F. J. M. Rutten, M. C. Davies and G. J. Leggett, “Fabrication of biomolecular nanostructures by scanning near-field photolithography of oligo(ethylene glycol)-terminated self-assembled monolayers”, *Langmuir*, 2007, **23**, pp. 7328–37.

150 E. ul Haq, Z. Liu, Y. Zhang, S. A. A. Ahmad, L.-S. Wong, S. P. Armes, J. K. Hobbs, G. J. Leggett, J. Micklefield, C. J. Roberts and J. M. R. Weaver, “Parallel scanning near-field photolithography : The Snomipede”, *Nano Lett.*, 2010, **10**, pp. 4375–4380.

151 B. Wu and A. Kumar, “Extreme ultraviolet lithography: A review”, *J. Vac. Sci. Technol. B*, 2007, **25**, pp. 1743–1761.

152 D. Gil, T. Bailey, D. Corliss, M. J. Brodsky, P. Lawson, M. Rutten, Z. Chen, N. Lustig, T. Nigussie, K. Petrillo and C. Robinson, “First microprocessors with immersion lithography”, *Proc. SPIE*, 2005, **5754**, pp. 119–128.

153 T. Sizyuk and A. Hassanein, “Extending the path for efficient extreme ultraviolet

sources for advanced nanolithography", *Phys. Plasmas*, 2015, **22**, p. 093101.

154 G. O'Sullivan, T. Cummins, P. Dunne, A. Endo, P. Hayden, T. Higashiguchi, D. Kilbane, B. Li, C. O'Gorman, T. Otsuka, E. Sokell and N. Yugami, "Recent progress in source development for lithography at 6.x nm", *Phys. Scr.*, 2013, **T156**, p. 014105.

155 K. Yoshimoto, M. P. Stoykovich, H. B. Cao, J. J. de Pablo, P. F. Nealey and W. J. Drugan, "A two-dimensional model of the deformation of photoresist structures using elastoplastic polymer properties", *J. Appl. Phys.*, 2004, **96**, pp. 1857–1865.

156 P. D. Ashby, D. L. Olynick, D. F. Ogletree and P. P. Naulleau, "Resist materials for extreme ultravioletlithography: Toward low-cost single-digit-nanometer patterning", *Adv. Mater.*, 2015, **Ahead of p**, p. n/a-n/a.

157 T. Kozawa and S. Tagawa, "Radiation chemistry in chemically amplified resists", *Jpn. J. Appl. Phys.*, 2010, **49**, p. 030001.

158 C. Lu and R. H. Lipson, "Interference lithography: A powerful tool for fabricating periodic structures", *Laser Photonics Rev.*, 2010, **4**, pp. 568–580.

159 C. V. Shank and R. V. Schmidt, "Optical technique for producing 0.1-μ periodic surface structures", *Appl. Phys. Lett.*, 1973, **23**, p. 154.

160 S. H. Zaidi and S. R. J. Brueck, "Multiple-exposure interferometric lithography", *J. Vac. Sci. Technol. B*, 1993, **11**, pp. 658–666.

161 J. Adams, G. Tizazu, S. Janusz, S. R. J. Brueck, G. P. Lopez and G. J. Leggett, "Large-area nanopatterning of self-assembled monolayers of alkanethiolates by interferometric lithography", *Langmuir*, 2010, **26**, pp. 13600–13606.

162 R. F. M. Thornley and T. Sun, "Electron beam exposure of photoresists", *J. Electrochem. Soc.*, 1965, **112**, pp. 1151–1153.

163 M. Hatzakis, "Electron resists for microcircuit and mask production", *J. Electrochem. Soc.*, 1969, **116**, pp. 1033–1037.

164 M. Altissimo, "E-beam lithography for micro-/nanofabrication", *Biomicrofluidics*, 2010, **4**, p. 026503.

165 C. Vieu, F. Carcenac, A. Pépin, Y. Chen, M. Mejias, A. Lebib, L. Manin-Ferlazzo, L. Couraud and H. Launois, "Electron beam lithography: Resolution limits and applications", *Appl. Surf. Sci.*, 2000, **164**, pp. 111–117.

166 W. Chen and H. Ahmed, "Fabrication of 5–7 nm wide etched lines in silicon using 100 keV electron-beam lithography and polymethylmethacrylate resist", *Appl. Phys. Lett.*, 1993, **62**, pp. 1499–1501.

167 A. A. Tseng, K. Chen, C. D. Chen and K. J. Ma, "Electron beam lithography in nanoscale fabrication: Recent development", *IEEE Trans. Electron. Packag. Manuf.*, 2003, **26**, pp. 141–149.

168 D. C. Joy, "The spatial resolution limit of electron lithography", *Microelectron. Eng.*, 1983, **1**, pp. 103–119.

169 G. Owen and P. Rissman, "Proximity effect correction for electron beam lithography by equalization of background dose", *J. Appl. Phys.*, 1983, **54**, pp. 3573–3581.

170 M. Osawa, K. Takahashi, M. Sato, H. Arimoto, K. Ogino, H. Hoshino and Y.

Machida, “Proximity effect correction using pattern shape modification and area density map for electron-beam projection lithography”, *J. Vac. Sci. Technol. B*, 2001, **19**, pp. 2483–2487.

171 T. Abe, H. Matsumoto, H. Shibata, T. Motosugi, Y. Kato, T. Ohnishi, J. Yashima, T. Iijima and H. Anze, “Proximity effect correction for mask writing taking resist development processes into account”, *Jpn. J. Appl. Phys.*, 2009, **48**, p. 095004.

172 D. Stiévenard, P. A. Fontaine and E. Dubois, “Nanooxidation using a scanning probe microscope: An analytical model based on field induced oxidation”, *Appl. Phys. Lett.*, 1997, **70**, pp. 3272–3274.

173 P. Avouris, T. Hertel and R. Martel, “Atomic force microscope tip-induced local oxidation of silicon: Kinetics, mechanism, and nanofabrication”, *Appl. Phys. Lett.*, 1997, **71**, pp. 285–287.

174 R. García, M. Calleja and F. Pérez-Murano, “Local oxidation of silicon surfaces by dynamic force microscopy: Nanofabrication and water bridge formation”, *Appl. Phys. Lett.*, 1998, **72**, pp. 2295–2297.

175 R. García, M. Calleja and H. Rohrer, “Patterning of silicon surfaces with noncontact atomic force microscopy: Field-induced formation of nanometer-size water bridges”, *J. Appl. Phys.*, 1999, **86**, pp. 1898–1903.

176 M. Calleja and R. García, “Nano-oxidation of silicon surfaces by noncontact atomic-force microscopy: Size dependence on voltage and pulse duration”, *Appl. Phys. Lett.*, 2000, **76**, pp. 3427–3429.

177 J. Berson, D. Burshtain, A. Zeira, A. Yoffe, R. Maoz and J. Sagiv, “Single-layer ionic conduction on carboxyl-terminated silane monolayers patterned by constructive lithography”, *Nat. Mater.*, 2015, **14**, pp. 613–621.

178 R. Maoz, S. R. Cohen and J. Sagiv, “Nanoelectrochemical patterning of monolayer surfaces: Toward spatially defined self-assembly of nanostructures”, *Adv. Mater.*, 1999, **11**, pp. 55–61.

179 K. L. Prime and G. M. Whitesides, “Self-assembled organic monolayers - model systems for studying adsorption of proteins at surfaces”, *Science (80-.).*, 1991, **252**, pp. 1164–1167.

180 R. E. Ducker, S. Janusz, S. Sun and G. J. Leggett, “One-step photochemical introduction of nanopatterned protein-binding functionalities to oligo(ethylene glycol)-terminated self-assembled monolayers”, *J. Am. Chem. Soc.*, 2007, **129**, pp. 14842–14843.

181 N. P. Reynolds, J. D. Tucker, P. A. Davison, J. A. Timney, C. N. Hunter and G. J. Leggett, “Site-specific immobilization and micrometer and nanometer scale photopatterning of yellow fluorescent protein on glass surfaces”, *J. Am. Chem. Soc.*, 2009, **131**, pp. 896–897.

182 S. C. Clear and P. F. Nealey, “Lateral force microscopy study of the frictional behavior of self-assembled monolayers of octadecyltrichlorosilane on silicon/silicon dioxide immersed in n-alcohols”, *Langmuir*, 2001, **17**, pp. 720–732.

183 Z. H. Lu, J. P. McCaffrey, B. Brar, G. D. Wilk, R. M. Wallace, L. C. Feldman and S. P. Tay, “SiO2 film thickness metrology by x-ray photoelectron spectroscopy”, *Appl.*

Phys. Lett., 1997, **71**, pp. 2764–2766.

184 S. R. Wasserman, Y.-T. Tao and G. M. Whitesides, "Structure and reactivity of alkylsiloxane monolayers formed by reaction of alkyltrichlorosilanes on silicon substrates", *Langmuir*, 1989, **5**, pp. 1074–1087.

185 S. R. Wasserman, G. M. Whitesides, I. M. Tidswell, B. M. Ocko, P. S. Pershan and J. D. Axe, "The structure of self-assembled monolayers of alkylsiloxanes on silicon: A comparison of results from ellipsometry and low-angle X-ray reflectivity", *J. Am. Chem. Soc.*, 1989, **111**, pp. 5852–5861.

186 S. Sun, M. Montague, K. Critchley, M.-S. Chen, W. J. Dressick, S. D. Evans and G. J. Leggett, "Fabrication of biological nanostructures by scanning near-field photolithography of chloromethylphenylsiloxane monolayers", *Nano Lett.*, 2006, **6**, pp. 29–33.

187 G. J. Leggett, "Light-directed nanosynthesis: Near-field optical approaches to integration of the top-down and bottom-up fabrication paradigms", *Nanoscale*, 2012, **4**, pp. 1840–1855.

188 S. Xia, M. Cartron, J. Morby, D. A. Bryant, C. N. Hunter and G. J. Leggett, "Fabrication of nanometer- and micrometer-scale protein structures by site-specific immobilization of histidine-tagged proteins to aminosiloxane films with photoremovable protein-resistant protecting groups", *Langmuir*, 2016, **32**, pp. 1818–1827.

189 G. B. Sigal, C. Bamdad, A. Barberis, J. Strominger and G. M. Whitesides, "A self-assembled monolayer for the binding and study of histidine-tagged proteins by surface plasmon resonance", *Anal. Chem.*, 1996, **68**, pp. 490–497.

190 G. W. de Groot, S. Demarche, M. G. Santonicola, L. Tiefenauer and G. J. Vancso, "Smart polymer brush nanostructures guide the self-assembly of pore-spanning lipid bilayers with integrated membrane proteins", *Nanoscale*, 2014, **6**, pp. 2228–2237.

191 A. Lio, C. Morant, D. F. Ogletree and M. Salmeron, "Atomic force microscopy study of the pressure-dependent structural and frictional properties of n-alkanethiols on gold", *J. Phys. Chem. B*, 1997, **101**, pp. 4767–4773.

192 G. Liu and M. B. Salmeron, "Reversible displacement of chemisorbed n-alkanethiol molecules on Au(111) surface: An atomic force microscopy study", *Langmuir*, 1994, **10**, pp. 367–370.

193 A. Hucknall, S. Rangarajan and A. Chilkoti, "In pursuit of zero: Polymer brushes that resist the adsorption of proteins", *Adv. Mater.*, 2009, **21**, pp. 2441–2446.

194 A. M. Alswieleh, N. Cheng, I. Canton, B. Ustbas, X. Xue, V. Ladmiral, S. Xia, R. E. Ducker, O. El Zubir, M. L. Cartron, C. N. Hunter, G. J. Leggett and S. P. Armes, "Zwitterionic poly(amino acid methacrylate) brushes", *J. Am. Chem. Soc.*, 2014, **136**, pp. 9404–9413.

195 A. Johnson, J. Madsen, P. Chapman, A. Alswieleh, O. Al-Jaf, P. Bao, C. R. Hurley, M. L. Cartron, S. D. Evans, J. K. Hobbs, C. N. Hunter, S. P. Armes and G. J. Leggett, "Micrometre and nanometre scale patterning of binary polymer brushes, supported lipid bilayers and proteins", *Chem. Sci.*, 2017, **8**, pp. 4517–4526.

196 A. Johnson, P. Bao, C. R. Hurley, M. Cartron, S. D. Evans, C. N. Hunter and G. J.

Leggett, “Simple, direct routes to polymer brush traps and nanostructures for studies of diffusional transport in supported lipid bilayers”, *Langmuir*, 2017, **33**, pp. 3672–3679.

197 S. Kumar, M. L. Cartron, N. Mullin, P. Qian, G. J. Leggett, C. N. Hunter and J. K. Hobbs, “Direct imaging of protein organization in an intact bacterial organelle using high-resolution atomic force microscopy”, *ACS Nano*, 2017, **11**, pp. 126–133.

198 S. Edmondson, V. L. Osborne and W. T. S. Huck, “Polymer brushes via surface-initiated polymerizations”, *Chem. Soc. Rev.*, 2004, **33**, pp. 14–22.

199 B. Du, M. R. VanLandingham, Q. Zhang and T. He, “Direct measurement of plowing friction and wear of a polymer thin film using the atomic force microscope”, *J. Mater. Res.*, 2001, **16**, pp. 1487–1492.

200 X.-D. Xiao, G.-Y. Liu, D. H. Charych and M. Salmeron, “Preparation, structure, and mechanical stability of alkylsilane monolayers on mica”, *Langmuir*, 1995, **11**, pp. 1600–1604.

201 E. Hochuli, H. Döbeli and A. Schacher, “New metal chelate adsorbent selective for proteins and peptides containing neighbouring histidine residues”, *J. Chromatogr. A*, 1987, **411**, pp. 177–184.

202 J. A. Bornhorst and J. J. Falke, “Purification of proteins using polyhistidine affinity tags”, *Methods Enzymol.*, 2000, **326**, pp. 245–254.

203 J. L. Hutter and J. Bechhoefer, “Calibration of atomic-force microscope tips”, *Rev. Sci. Instrum.*, 1993, **64**, pp. 1868–1873.

204 A. Simakova, S. E. Averick, D. Konkolewicz and K. Matyjaszewski, “Aqueous ARGET ATRP”, *Macromolecules*, 2012, **45**, pp. 6371–6379.

205 G. J. Dunderdale, C. Urata, D. F. Miranda and A. Hozumi, “Large-scale and environmentally friendly synthesis of pH-responsive oil-repellent polymer brush surfaces under ambient conditions”, *ACS Appl. Mater. Interfaces*, 2014, **6**, pp. 11864–11868.

206 K. Min, H. Gao and K. Matyjaszewski, “Use of ascorbic acid as reducing agent for synthesis of well-defined polymers by ARGET ATRP”, *Macromolecules*, 2007, **40**, pp. 1789–1791.

207 D. A. Dobbs, R. G. Bergman and K. H. Theopold, “Piranha solution explosion”, *Chem. Eng. News*, 1990, **68**, p. 2.

208 K. Werner and D. A. Puotinen, “Cleaning solution based on hydrogen peroxide for use in silicon semiconductor technology”, *RCA Rev.*, 1970, **31**, pp. 187–206.